Characterizing Adsorbents for Pre- and Post-Combustion Carbon Capture

by

Nicholas Stiles Wilkins

A thesis submitted in partial fulfillment of the requirements for the degree of

Master of Science

in

Chemical Engineering

Department of Chemical and Materials Engineering

University of Alberta

Abstract

Anthropogenic CO_2 emissions are driving climate change. The largest sources of emitted CO_2 are coal and fossil fuel power plants. One proposed solution to mitigate emissions is to capture CO_2 from fossil fuel power plants and store it underground. This is the basis of carbon capture and storage (CCS). There are two main carbon capture processes that are utilized in industry: pre- and post-combustion capture. In post-combustion capture, the fuel is combusted to generate power and then CO_2 is separated afterwards. In pre-combustion capture, a fuel is gasified and catalytically converted to mostly CO_2 and H_2; the H_2 is then combusted to generate power. Adsorption has been suggested as a possible mechanism to capture CO_2. In early design stages it is practical to simulate an adsorbent using a process model. This cuts costs and time associated with physical experiments. This thesis characterized and built models for adsorptive pre- and post-combustion processes. TDA Research Inc. (Wheat Ridge, CO, USA) has developed an activated carbon adsorbent called TDA 2015 (a pseudonym for patent protections) for pre-combustion carbon capture. A series of dynamic column breakthrough experiments were performed to determine equilibrium loadings and to build a model in our in-house adsorption simulator. These experiments were performed at $\approx$ 160, 200 and 240°C and $\approx$ 2.5, 4.5, 6.5, 8.5 and 10.5 bar of CO_2. Additional equilibrium loadings were measured using volumetry at 30, 60, 120 and 160°C from vacuum to 1.2 bar. At this time H_2 was not characterized, but it known to be very weakly adsorbing on TDA 2015. A LRC isotherm was fit to the equilibrium data and utilized in the adsorption simulator. At $\approx$ 2.5, 4.5 and 6.5 bar of CO_2 the experimental and simulated results were in good agreement. However, at 8.5 and 10.5 bar of CO_2, the LRC isotherm could quantitatively predict the loading, but not qualitatively predict the concentration or thermal breakthrough shape. A case study was performed to determine possible explanations to this behavior. For post-combustion capture, a premium (Z10-02ND) and standard (Z10-02) zeolite 13X were obtained from Zeochem (Uetikon am See, Switzerland) and studied. H_2O adsorbs very strongly on zeolite 13X. Due to this fact it usually neglected in adsorptive post-combustion capture studies. For this study, post-combustion flue gas is considered as a mixture of CO_2, H_2O and N_2. CO_2 and N_2 equilibrium loadings were measured from 0 to 150°C and 0 to 5 bar

using volumetry and gravimetry. Equilibrium data was fit to a dual-site Langmuir isotherm for all components. A series of single component CO_2 and H_2O breakthrough experiments were measured on both zeolite 13X samples at 22°C and 1.02 bar. These were modeled and simulated with the in-house adsorption simulator. The simulator predicted breakthrough behavior well for all materials and components. Competitive CO_2 and H_2O breakthrough experiments were then performed at 22°C and 1.02 bar. The competitive breakthrough experiments were also simulated with the breakthrough simulator. However, the dual-site Langmuir isotherm was not able to capture the nonideality of the CO_2/H_2O mixture well.

To my family and friends
Alla mia famiglia ed ai miei amici
Manai ģimenei un draugiem

"**Costanza: non chi comincia, ma quel che persevera**"
Constancy: not the one who starts, but the one who perseveres
Leonardo Da Vinci

Acknowledgements

Grazie alla mia ragazza Ilaria, per la forza a continuare ed a vivere la vità al massimo. Ti amo. Anche, vorrei ringraziare ai genitori di Ilaria per credermi.

I would like to thank my family for their love and support. Riley and Taylor for being the best siblings and for all the trips to Sam Deigo's. Mom and Dad for teaching me the value of perseverance and hard work. Paldies Momoo and Granddude for introducing me to engineering and encouraging my curiosity. Khaki for listening to Dad and I talk your ears off about skiing at Killington. The Meyer family for letting me sleep at their house on my cross country moves.

Contents

List of Figures

List of Tables

Chapter 1

Introduction

1.1 Introduction to Climate Change

Climate change has been observed all over the world, from increased chances of wildfire in the North American west, to widespread droughts across all continents (except Antartica) and to the destruction of marine ecosystems off of Australia, the United States and Mexico [1]. If climate change continues at its current rate, by 2100 the Earth's average temperature is expected to increase $\approx 5°C$ from the current global average [1]. These changes will be more extreme at the Earth's poles, increasing the rate of glacial ice melting and ultimately raising the level of the ocean [1]. While some of these factors have previously been mentioned, the Intergovernmental Panel on Climate Change (IGCC) has published a summary of the reasons why one should be concerned about climate change; these reasons include: destruction to unique and threatened cultures and ecosystems, more frequent extreme weather events, reduced crop yield, increased and more severe droughts and destruction to certain economies (such as fishing) [1]. It is expected that if climate change remains unmitigated, these problems will be amplified.

Climate change is proceeding exponentially faster each year with an increasing population and demand for power. Carbon dioxide emissions have doubled since 1971 [2]. Figure 1.1 shows CO_2 emissions from 1751 to 2014 [3]. Due to an increasing amount of emissions, the ambient concentration of CO_2 has also increased, as seen in Figure 1.1 [4,5]. The historical ambient CO_2 concentration record was ≈ 300 ppm about 325 thousand years ago [4]. When this thesis was written, the ambient CO_2 concentration was 406.31 ppm [5].

The scientific community has predominantly reached the conclusion that climate change is due to human interference [1]. A large contributor is the exhaust of greenhouse gases, such as CO_2, CH_4, NO_2 (smog) and chlorofluorocarbons [6]. The United States, in 2015 alone, emitted an equivalent of 6587 million tonnes of CO_2 in greenhouse gases; $\approx 82\%$ was CO_2 [6]. Humans are dependent on technologies that produce greenhouses gases, from vehicular transportation to power generation and even agricultural processes. One of the main challenges for climate change mitigation is to create and build technologies that will keep the global standard of living

the same, or make it better. One of many proposed solutions is to emit less greenhouse gases to the environment. This can be achieved by changing power generation to green or renewable sources, or by making currently carbon positive sources carbon neutral or carbon negative.
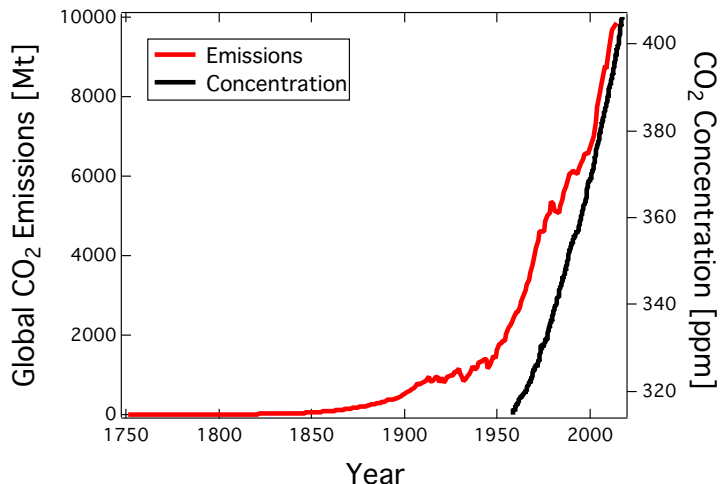
Figure 1.1: Global CO_2 emissions in millions of tonnes from 1751 to 2014 and the ambient concentration of CO_2 in parts per million from 1959 to 2017 with seasonal CO_2 cycling removed [3–5].

1.2 Introduction to Carbon Capture

Many industrial and agricultural processes release CO_2 to the atmosphere. It is widely accepted that anthropogenic CO_2 emissions, and other greenhouse gasses, are driving climate change [1]. To combat climate change many technologies have been proposed to mitigate anthropogenic CO_2 sources. One proposed idea is to remove CO_2 from industrial waste streams before releasing the effluent gas to the environment. The removed CO_2 could be stored underground, or utilized as a solvent for enhanced oil recovery [7,8]. This is the basis of carbon capture and storage (CCS).

Carbon capture is the study of separating CO_2 out of a bulk gas stream, usually from an industrial power plant. There are two main combustion processes that are used for energy production: pre-combustion and post-combustion. Post-combustion is the familiar combustion reaction where a fuel is combusted in the presence of air to produce predominantly H_2O and CO_2. Pre-combustion utilizes the water-gas shift reaction to pre-combust a fuel into CO_2 and H_2. CO_2 is removed from gas mixture and H_2 is combusted to generate power. Both processes operate at different pressures and temperatures. Typical post-combustion conditions are 15 mol% CO_2 at room temperature, $\approx 25°C$, and about 0.03 to 5 bar total pressure [9]. For pre-combustion, the concentration of CO_2 is between 15 and 60 mol% with a total feed pressure of 20 to 70 bar [8]. In pre-combustion processes, CO_2 is ≈ 1000 times more concentrated than in post-combustion conditions [8]. Both processes are shown in Figure 1.2.
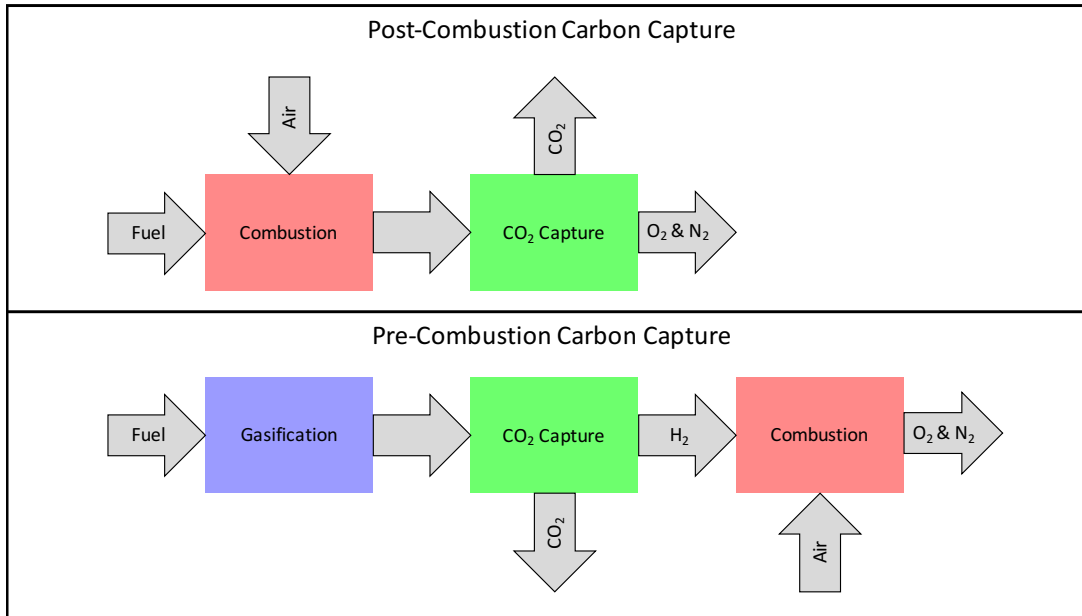
Figure 1.2: Simplified pre- and post-combustion carbon capture schematics.

There are advantages and disadvantages to both processes. It is easy to retrofit post-combustion plants for CO_2 capture [7]. A power plant can still operate during the construction of a post-combustion CO_2 capture plant. Post-combustion capture is the most common way that CO_2 can be captured in fossil fuel power plants [10]. Post-combustion capture has also been heavily researched. However, due to low operating pressures and concentrations, post-combustion can be inefficient [7]. In pre-combustion capture, higher CO_2 concentrations facilitate capture; but, there are a limited number of integrated gasification combined cycle (IGCC) plants that can perform pre-combustion capture [10, 11]. Also, pre-combustion must be integrated at the start of design and construction, because capturing CO_2 is an integral part of the process to purify H_2 for combustion [11]. There are also some losses in electrical efficiency due to the H_2 rich gas stream [7]. For both processes, more energy must be used for the same net amount of power generation if CO_2 capture is implemented [7, 10].

In 2016, the Global CCS Institute had identified 38 large-scale carbon capture and storage projects that are currently operating or under construction [12]. Boundary Dam in Saskatchewan, Canada was the first large-scale carbon capture project. Boundary Dam was operational in October, 2014. Since then, many have been built in across the world, but most CCS facilities are in the United States and Canada [12]. The largest carbon capture and storage plant currently in operation is in Texas, United States; it is a vacuum swing adsorption process that has captured and stored 3 million tonnes of CO_2 [8].

1.3   Adsorption

Adsorption is a process where a gas molecule enters the pores or adheres to the surface of a solid material, called an adsorbent; this could be through a physical or chemical mechanism [13]. The reverse process, when a gas molecule leaves the pores or surface of an adsorbent, is called desorption. Adsorption is an exothermic process and desorption is endothermic. Therefore, the process temperature becomes important, since at lower temperatures adsorption will become more favorable. Again, the analogue is that desorption becomes more favorable at high temperatures.

An isotherm is an equilibrium diagram that shows how much of a gas adsorbs into an adsorbent at a given pressure and temperature. An example of an isotherm at multiple temperatures is shown in Figure 1.3. At lower temperatures, more gas adsorbs since adsorption is an exothermic process; also, as the gas's pressure decreases less is adsorbed. Each gas in a bulk mixture of gases will have an isotherm on a given adsorbent. Isotherms will be explained in more detail in Chapter 2. A separation can be performed by manipulating a gas's partial pressure or temperature. These two processes are called pressure swing adsorption and temperature swing adsorption.
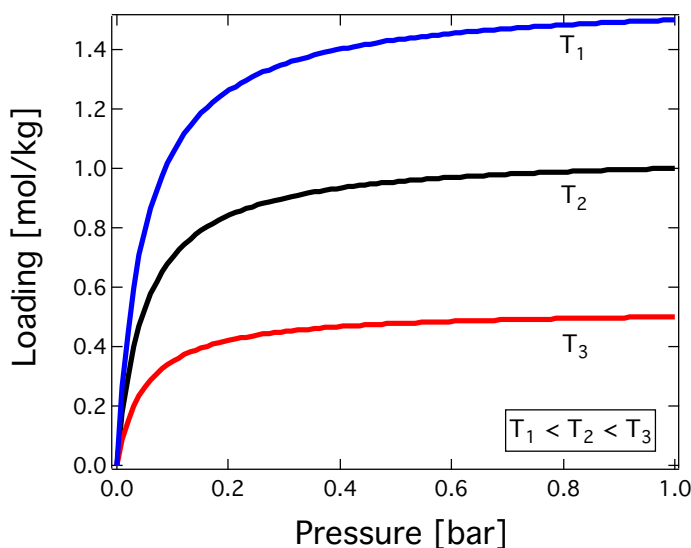
Figure 1.3: Examples of an isotherm at temperatures T_1, T_2 and T_3, where $T_1 < T_2 < T_3$.

1.3.1   Temperature Swing Adsorption

During a temperature swing adsorption, TSA, process, a mixture of gases flows through a column packed with an adsorbent at a given temperature, T_{ads}, and pressure, P. After a given amount of time, the flow through the column is stopped and the column is heated up to T_{des} to remove trapped gases through either the inlet or outlet of the column. This is the most basic example of a temperature swing adsorption process. This process can be visualized on the isotherm for one of the gases in Figure 1.4.

4
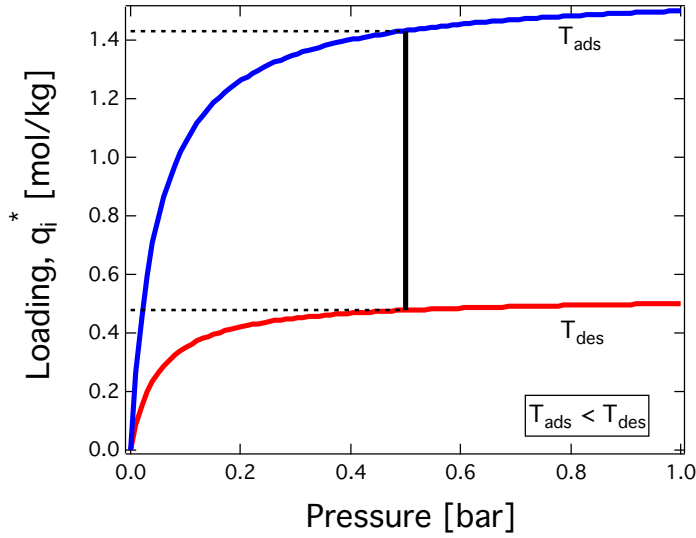
Figure 1.4: A temperature swing adsorption process represented on the isotherm. The first step is at T_{ads} and 0.5 bar. The second step is at T_{des} and 0.5 bar. This process is assumed to be isobaric. The solid black line is the process path and the black dashed lines show the process' working capacity.

The difference between the black dashed lines in Figure 1.4 yields the working capacity of this process. The working capacity, defined in Equation 1.1, is the amount of moles of gas i that can be separated per kg of adsorbent using a specific process.

$$\Delta q_i^* = q_{i,ads}^* - q_{i,des}^* \tag{1.1}$$

1.3.2 Pressure Swing Adsorption

During a pressure swing adsorption, PSA, process, a mixture of gases flows through a column packed with an adsorbent at a given pressure, P_{ads}, and temperature, T. After a given amount of time, the flow through the column is stopped and the column pressure is reduced to P_{des} to remove accumulated gases. Again, this is the most basic example; actual adsorption cycling can become much more complicated. Figure 1.5 shows the process graphically for an isothermal process. The black line is the PSA process' path. Many PSA processes are not isothermal; therefore the process path is slightly different than shown in Figure 1.5. However, if the P_{ads} and P_{des} are at the same temperature, than the working capacity, Δq_i^*, would be the same. For PSA processes, the best working capacities will be found as P_{des} approaches 0 bar.
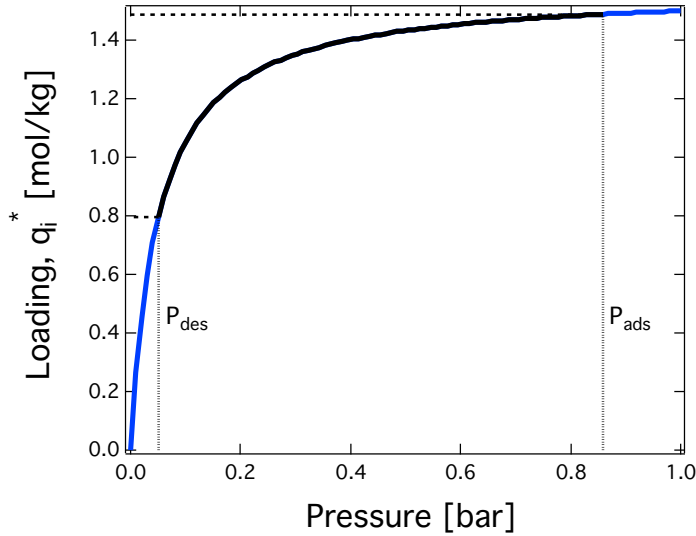
Figure 1.5: A pressure swing adsorption process represented on the isotherm. The first step is at P_{ads} and temperature T. The second step is at P_{des}. This process is assumed to be isothermal. The blue line is the isotherm at temperature T. The solid black line is the process path and the black dashed lines (on the y-axis) show the process' working capacity.

1.3.3 Adsorption in Packed Beds

To perform temperature and pressure swing adsorption processes, a column packed with adsorbent is utilized. When a packed column is first installed, the adsorbent must be activated, or regenerated; both terms mean that the adsorbent should either be brought to low pressures, high temperatures or both to remove all trapped gases from the adsorbent. After activation, feed gas can be injected into the column. Since adsorption is a transient process, after some time the column will be saturated with the feed gas. At this point, the gas that enters and leaves the column have the same concentration. To desorb the column, a step function of inert, or weakly adsorbing, gas is injected into the column or the column's pressure is reduced. All of these processes are shown in Figure 1.6. The strongly adsorbing component's concentration front, normalized by the feed concentration, C_0, is also shown in Figure 1.6. For this thesis, a column is assumed to be one-dimensional and concentration does not change radially, only axially. Concentration breakthrough is the time when the feed gas leaves the packed bed. This can be visualized as the shock transition in the elution profile from Figure 1.6a to Figure 1.6b. This, however, does not fully represent breakthrough in general. To say a gas has broken through the column, both the concentration and thermal fronts must go to the feed conditions. As the gas adsorbs, heat is released, raising the column's temperature. As the column cools down, more gas is adsorbed. Thermal breakthrough is the same concept as concentration breakthrough, but with feed temperature instead of concentration. Thermal breakthrough, seen in Figure 1.6, usually takes much longer than concentration breakthrough.

6
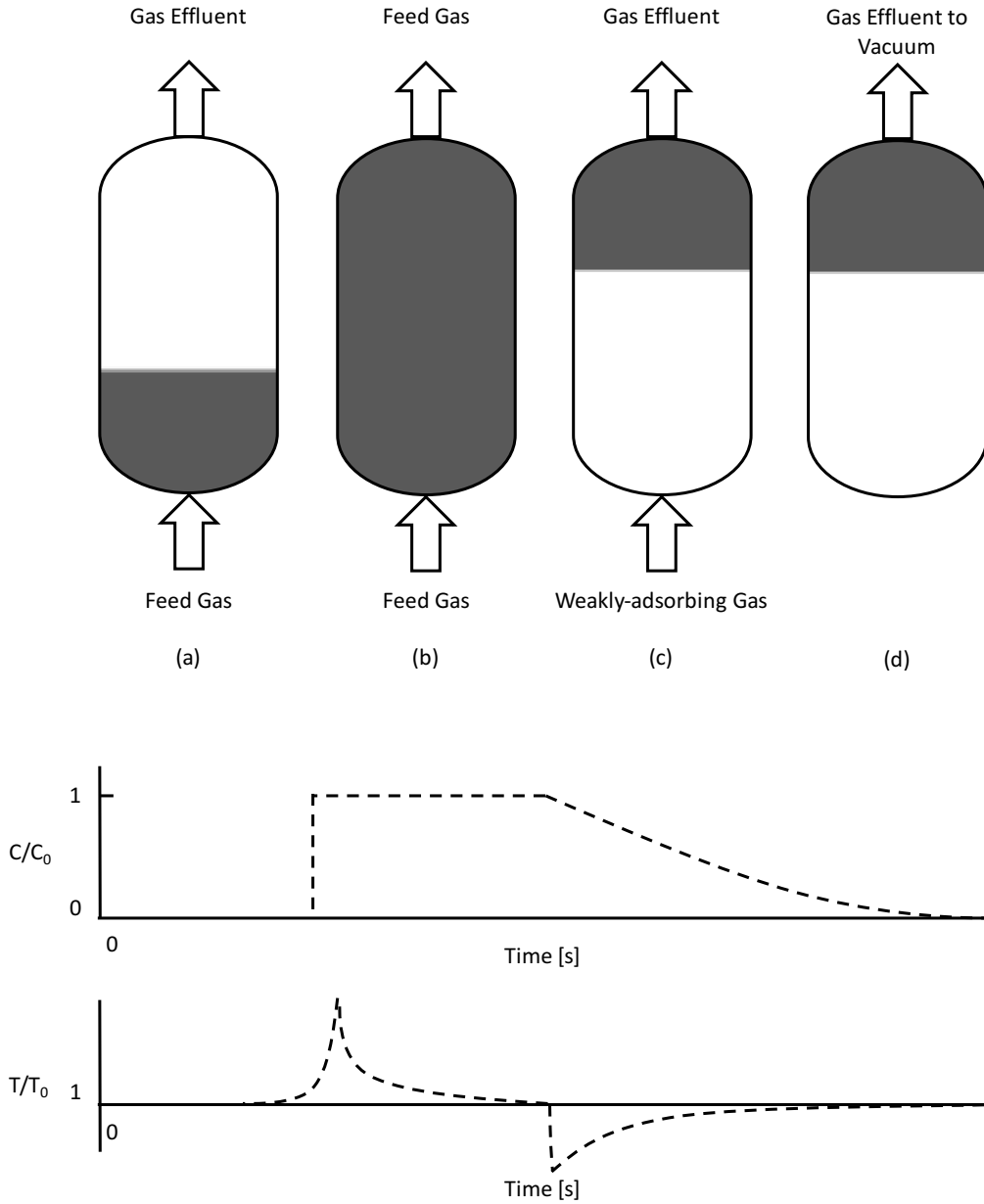
Figure 1.6: Common adsorptive processes in packed beds with corresponding elution profiles. (a) shows an adsorption step where an adsorbing feed gas is injected into the column. (b) shows a column that has been saturated with feed gas; this gas has broken through the column. (c) shows a desorption step where an inert, or weakly adsorbing, gas is injected into the column as a step. (d) also shows a desorption step, but instead of injecting a weakly adsorbing gas, the column is vacuumed from one end. Both (c) and (d) produce similar elution profiles. Gray shows the strongly adsorbing component's concentration front traveling through the column at some time.

1.4 Adsorbent Materials for Pre- and Post-Combustion Carbon Capture

Many adsorbent materials exist for pre- and post-combustion carbon capture. Most carbon capture materials separate CO_2 via an equilibrium separation. These adsorbents have a strong affinity to CO_2 when compared to H_2 or N_2; CO_2 is preferentially adsorbed onto the adsorbent. This thesis will deal with a very small subset of the available adsorbents detailed in the following sections.

1.4.1 Zeolites

Zeolites are porous aluminosilicates that are created by a framework of SiO_4 and AlO_4 assembled in tetrahedra and bonded by shared oxygen atoms [13]. The framework is an open crystalline lattice that allows other molecules to enter. A zeolite's micropore is controlled by the crystalline lattice, therefore there is almost no distribution in pore size [13]. Zeolites are classified based on their crystalline lattice, Al to Si ratio and pore size. For post-combustion carbon capture, zeolite 13X has been heavily studied [9, 14–17]. This is due to its high CO_2 capacity at vacuum pressures, rectangular isotherm and cheap cost. Zeolite 13X is the benchmark adsorbent for post-combustion carbon capture. Zeolite 13X has a very low affinity for N_2 and O_2, but an extremely high affinity for H_2O; because of this, zeolite 13X performs the best in non-humid conditions [18]. At higher pressures (> 5 bar), the CO_2 to N_2 selectivity drops. This makes zeolite 13X a bad candidate for pre-combustion carbon capture.

1.4.2 Activated Carbons

Activated carbons are made from carbonaceous materials, such as coal or biomass [13]. Activated carbons undergo a thermal activation at very high temperatures, normally between 700-1100°C, to remove trapped materials and to open the pores for adsorption [13]. Activated carbons usually have a large distribution of pore sizes and are hydrophobic [13]. At atmospheric and vacuum pressures, there is not a great selectivity of CO_2 over N_2, but there is essentially no H_2O affinity. Therefore, it is possible to use activated carbons for post-combustion carbon capture, but the separation is not as great as dry post-combustion flue gas on zeolite 13X [19]. For this study, TDA Research Inc. has provided an activated carbon called TDA 2015 (a pseudonym for patent protections), which expresses high CO_2 capacity at high pressures ($\approx 3 - 11$ bar). TDA 2015 has almost no affinity for H_2. Like other activated carbons, it is hydrophobic. For these reasons, TDA 2015 is a great candidate for pre-combustion carbon capture.

1.5 Thesis Objectives and Outline

The focus of this thesis is to characterize and model adsorbent materials for pre- and post-combustion carbon capture. Pressure swing adsorption (PSA) processes have become very popular for carbon capture within the past two decades. It is necessary to design good PSA processes

in a cheap manner. With greater computing, it is now possible to design PSA processes using numerical simulators. In these studies, PSA models are created for pre- and post-combustion carbon capture systems from small scale equilibrium and dynamic column breakthrough experiments. From small scale experiments, these models and simulations can be used to predict large scale systems with great accuracy [17].

The main objectives of this thesis are:

1. to characterize and model a new adsorbent, TDA 2015, by TDA Research Inc. for pre-combustion carbon capture.

2. to characterize and model humid post-combustion carbon capture on standard and premium zeolite 13X (Zeochem Z10-02 and Z10-02ND, respectively).

These are all previously unmodeled or non-validated systems.

Modeling TDA 2015 would allow future researchers to optimize process conditions for adsorptive pre-combustion carbon capture on TDA 2015. This would include determining which adsorbent cycles separate CO_2 best on TDA 2015 using the least amount of energy. The TDA 2015 model could be used to maximize efficiency in the entire IGCC process as well. This could determine whether TDA 2015 is a feasible adsorbent for a full scale IGCC plant or if other adsorbents should be considered.

Characterizing the competition between H_2O and CO_2 on zeolite 13X would show whether it is feasible to use zeolite 13X in a humid post-combustion carbon capture process. The vast majority of the literature neglects H_2O adsorption on zeolite 13X, despite the fact that H_2O and CO_2 are extremely competitive and non-ideal. This would allow adsorbent cycles to be designed and optimized to maximize CO_2 purity and recovery while using the least amount of energy possible. Also, this model would be the first to be validated by experimental breakthrough experiments.

Chapter 2 details the theory and methods used in this study. General methodology, purpose and mathematics for volumetry, gravimetry and dynamic column breakthrough are discussed. Equilibrium isotherm models for single and multicomponent systems are detailed. The mathematical model for the in-house adsorption simulator is explained.

Chapter 3 deals with the characterization of TDA 2015, an activated carbon for pre-combustion carbon capture. This activated carbon shows great promise, as it has a greater CO_2 loading than previous TDA Research Inc. materials, such as TDA AMS 19. Equilibrium data for CO_2 was measured through volumetry and dynamic column breakthrough. A model was developed using specific adsorbent and column properties. Simulations were performed and predict the

equilibrium loading well. At higher concentrations, the simulations do not fit the qualitative trend of the experimental concentration or temperature breakthrough profiles well.

Chapter 4 deals with the characterization of standard (Zeochem Z10-02) and premium (Zeochem Z10-02ND) zeolite 13X for humid post-combustion carbon capture. The competition between CO_2 and H_2O was studied. Equilibrium data was collected for CO_2, H_2O and N_2 through volumetry, gravimetry, dynamic column breakthrough and previous studies. Using specific adsorbent and column properties a model was developed, as in Chapter 3. Simulations were able to predict dynamic breakthrough concentration and temperature profiles well. Loadings between simulations and experiments were matched. Competitive CO_2/H_2O breakthrough experiments were also performed and simulated.

Chapter 5 summarizes the conclusions of this study and provides recommendations for future work.

Chapter 2

Adsorption Equilibria and Column Dynamics

2.1 Introduction

Many physical and numerical experiments were necessary to model and simulate adsorbent systems for pre- and post-combustion processes. Adsorption equilibrium on a particular adsorbent must be described well. It is critical to have a good isotherm model to predict adsorptive behavior. Adsorption equilibrium, and dynamics, can be determined through various physical experiments on small scale systems. After adsorption equilibrium and dynamics data have been collected, they are modeled and simulated using an in-house adsorption simulator. This simulator uses an isotherm to predict fluid and solid concentration, temperature and pressure profiles along the adsorbent bed. The experiments and simulator used in this thesis will be presented in this chapter.

2.2 Adsorption Equilibrium

Understanding gas, or vapor, equilibrium on a solid adsorbent is essential to predict adsorptive behavior. Equilibrium, quantified as moles of gas per kg of adsorbent, is measured as a function of concentration of a pure component. There are many different experimental procedures to collect adsorption equilibrium data. Some of the most common techniques are volumetry, gravimetry and dynamic column breakthrough.

Before detailing the specifics of each of the previously mentioned methods, it is important to explain what it being measured during an equilibrium experiment. Adsorption equilibrium can be represented as an absolute, excess or net amount depending on the reference state chosen [20]. The difference between these reference states can be seen graphically in Figure 2.1.
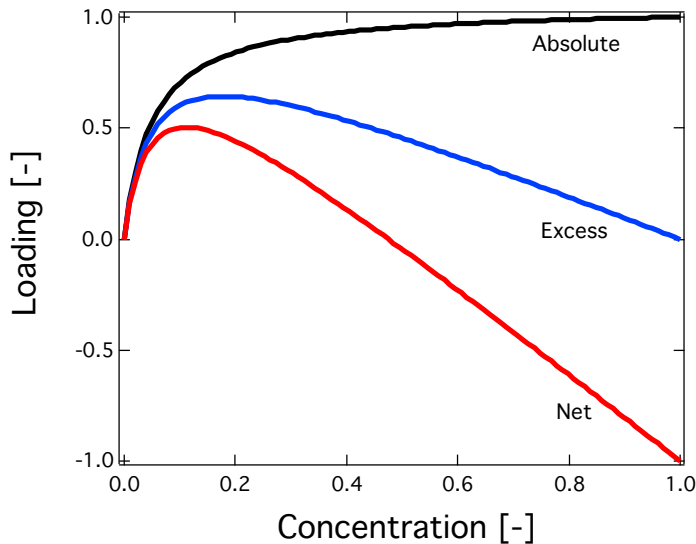
Figure 2.1: Absolute, excess and net isotherms for a hypothetical system.

The absolute amount of gas adsorbed, n_{abs}, is defined as the total number of moles of gas adsorbed in a microporous solid [20]. Thermodynamically, absolute adsorption is the most correct way to describe adsorption [21, 22]. However, it is not easy to determine absolute equilibrium data since information about the microporous structure must be known.

All equilibrium experiments measure excess adsorption. Excess adsorption, n_{ex}, is the total moles of gas adsorbed into an accessible volume, defined in Equation 2.1.

$$n_{ex} = n_{abs} - (V_s - V_{NA})\rho_i \tag{2.1}$$

The accessible volume is defined as the difference between the total adsorbent volume, V_s, which consists of the macro and micropore volumes, and the inaccessible volume, V_{NA} [22]. The inaccessible volume is the volume of the adsorbent that the gas can not diffuse into. ρ_i is the density of the gas. However, this becomes an over correction when the gas approaches supercritical conditions [23]. At lower pressures, excess and absolute adsorption are essentially the same and can be used interchangeably [21].

The net amount adsorbed is similar to the excess amount adsorbed. For net adsorption, both the non-adsorbed gas within the solid and the entire volume of the solid are removed, as shown in Equation 2.2 [22, 24].

$$n_{net} = n_{abs} - V_s\rho_i \tag{2.2}$$

The resulting amount adsorbed is the total amount of gas within experiment minus the amount that would exist without the adsorbent [24]. This definition, reduces the ambiguity of adsorption measurements by removing the need for pore volume or inaccessible volumes [24].

2.2.1 Volumetry

Volumetry uses a calibrated volume to determine the volume of gas adsorbed into an adsorbing solid. A simple volumetric unit is shown in Figure 2.2.
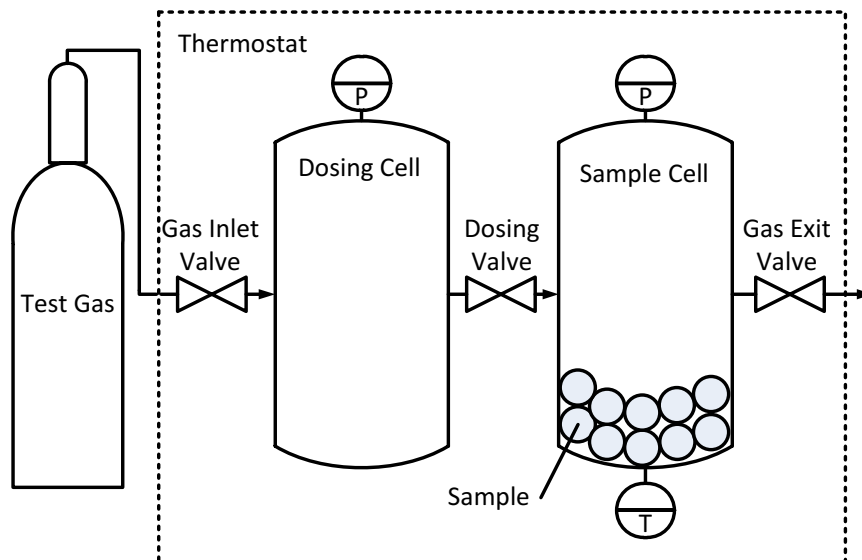
Figure 2.2: A generalized volumetry apparatus.

A volumetric experiment contains two cells: the dosing cell and the sample cell. The dosing cell contains a known volume of gas, V_{dose}. The sample cell's volume is calculated in Equation 2.3 as the difference between the empty cell volume, V_{empty}, and the adsorbent solid's volume, V_s.

$$V_{sc} = V_{empty} - V_s \tag{2.3}$$

These two cells are connected via a valve, called the dosing valve, that is opened at $t = 0$ and closed after some time. After the dosing valve is closed, the pressure in the sample cell is monitored. Once the pressure stops changing in the system, adsorption equilibrium has been reached. This can be continued until a desired equilibrium pressure is reached. The dosed number of moles is calculated by Equation 2.4 after each pressure dosing step, j. The pressure and temperature difference, between dosing and equilibrium, will give the dosed number of moles, $n_{dosed,j}$.

$$n_{dosed,j} = n_{dosed,j-1} + n(P_{dosed}, V_{sc}, T_{dosed}) - n(P_{eq}, V_{sc}, T_{eq}) \tag{2.4}$$

P_{dosed} and T_{dosed} are the pressure and temperature at the time that dosing occurs. P_{eq} and T_{eq} are the pressure and temperature when equilibrium is reached. This is added to the previous number of dosed moles, if a previous dosing has occured, $n_{dosed,j-1}$. Any suitable equation of state can be used to determine the gaseous moles dosed. The free space accumulation, $n_{FS,j}$,

must be subtracted, using Equation 2.5, to determine the amount of moles adsorbed in the solid, $n_{ads,j}$.

$$n_{ads,j} = n_{dosed,j} - n_{FS,j} \tag{2.5}$$

The loading, q_i^*, can be found using Equation 2.6 by taking the moles adsorbed and dividing it by the mass of the adsorbent, m_{ads}.

$$q_{i,j}^* = \frac{n_{ads,j}}{m_{ads}} \tag{2.6}$$

The volumetric apparatus used in this study is a Micromeritics ASAP 2020. This unit is capable of measuring pure component equilibrium up to approximately 1.2 bar. The sample cell can be heated to approximately 160°C. Measurements can be done automatically or manually.

2.2.2 Gravimetry

Gravimetry measures the mass of gas adsorbed into an adsorbent using a mass balance. A schematic of a magnetic suspension balance is shown in Figure 2.3. A known pressure of gas flows past a cell that contains the adsorbing solid. As the gas is adsorbed, the mass of the adsorbent changes and is recorded. Once the change in the adsorbent mass stops, equilibrium has been reached.
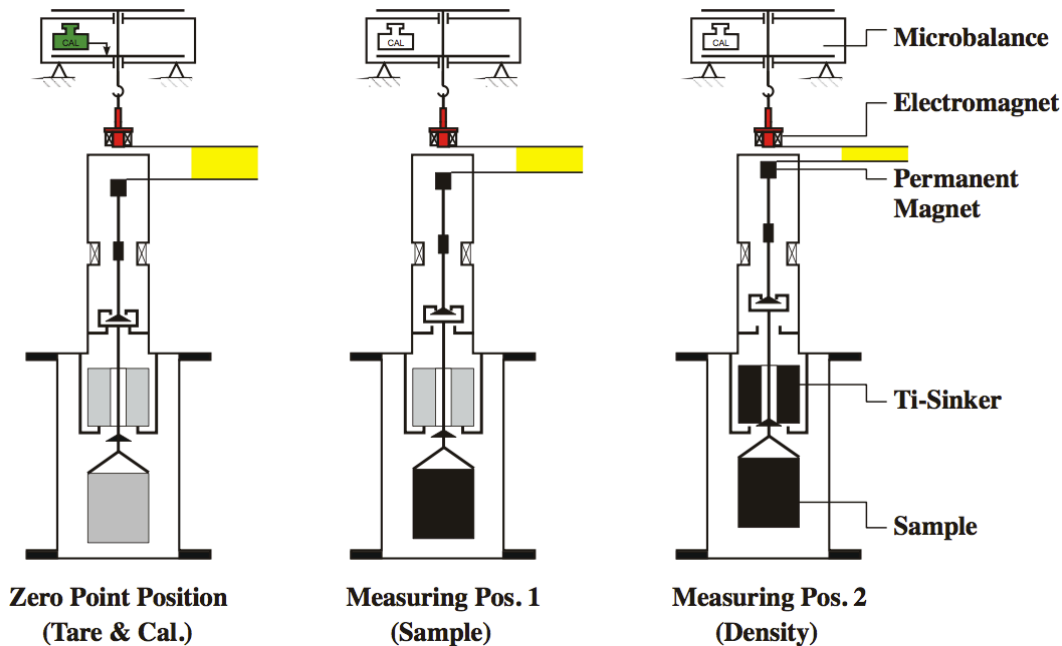
Figure 2.3: A schematic of the magnetic suspension balance's operational positions [25]. The black objects indicate the parts that are lifted at each step. Gray objects are not lifted.

The magnetic suspension balance operates in three modes shown in Figure 2.3. The first position is the "zero point". As seen in Figure 2.3, when the magentic suspension balance operates at the zero point, the balance does not lift the sample container or the sinker. At this position

the initial calibration and the tare weight are determined, M_0. For the majority of the unit's operation, "measuring position 1" is measured. At this position, only the sample container is lifted to measure the sample container's weight, M_1. At "measuring point 2," the sample container and sinker are lifted to determine M_2, which is used to calculate the bulk gas density.

Using these measured values, M_0, M_1 and M_2, and the fact that the sinker has a calibrated mass, m_{sink}, and volume, V_{sink}, the mass uptake can be measured. A series of preliminary experiments must be performed to characterize some unknown masses and volumes. The sample container's mass, m_{samp}, is calculated by Equation 2.7 through an experiment at vacuum and high temperature.

$$m_{samp} = M_1(\rho_{bulk} \to 0, T \to \infty) = M_1(0, \infty) \tag{2.7}$$

This minimizes the bulk density, ρ_{bulk}, within the apparatus to minimize buoyancy effects [23]. At any given conditions, the bulk density is determined from Equation 2.8 [23].

$$\rho_{bulk} = \frac{m_{sink} + M_1(\rho_{bulk}, T) - M_2(\rho_{bulk}, T)}{V_{sink}} \tag{2.8}$$

To determine the sample container and sorbent volume, V_{samp} and V_s, experiments are performed in an inert environment, usually helium. A series of experiments at different bulk densities, performed by varying the pressure, will yield a graph of measured weight, M_1, against the bulk density. From a linear regression, V_{samp} is found.

A similar process is followed to find V_s. Experiments are performed at different bulk densities in a non-adsorbing environment. A plot of bulk density as a function of measured weight (M_1) is produced to yield the total volume, V_{tot}, which is the addition of the sorbent and sample container volume, shown in Figure 2.4.

V_s is found from the difference of the total and sample container volumes, shown in Equation 2.9.

$$V_s = V_{tot} - V_{samp} \tag{2.9}$$

After these unknowns are found, the adsorbed mass, m_{sorb}, can be found from Equation 2.10 [23].

$$m_s = M_1(\rho_{bulk}, T) - M_1(0, \infty) + \rho_{bulk} V_s \tag{2.10}$$

The m_s calculated in gravimetric experiments are absolute adsorption measurements. Before the buoyancy experiment, the raw data is an excess measurement. The buoyancy experiment corrects the measured excess isotherm points to absolute adsorption measurements, by determining ρ_{bulk} as a function of total pressure.
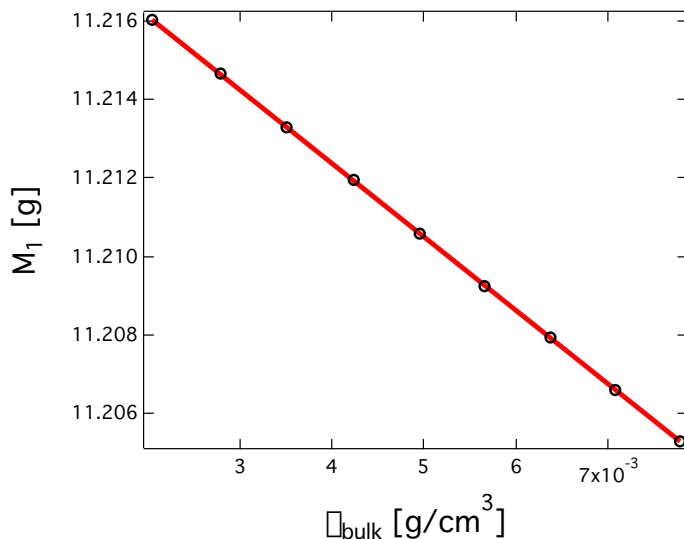
Figure 2.4: The buoyancy measurement gives the total volume, which is the the sample container's volume plus the adsorbent's volume. The black circles are experimentally collected points. The red line is a linear trendline, $M_1 = -1.85\rho_{bulk} + 11.22$. The total volume, 1.85 cm^3, is found from the slope.

2.2.3 Dynamic Column Breakthrough

A dynamic column breakthrough apparatus (DCB) is a small column packed with a known mass of adsorbent that can determine adsorption equilibrium and column dynamics. The DCB used in this study is shown in Figure 2.5.
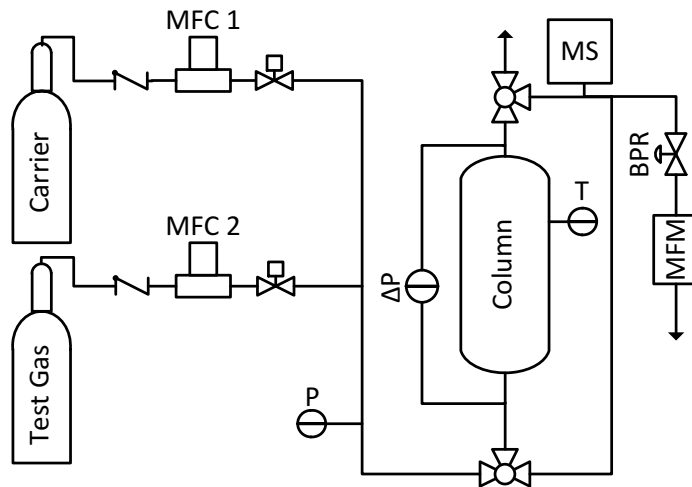
Figure 2.5: The dynamic column breakthrough apparatus. In this schematic: BPR = back-pressure regulator, MFC = mass flow controller, MFM = mass flow meter, MS = mass spectrometer, P = pressure transducer, ΔP = differential pressure transducer and T = thermocouple.

At time $t < 0$ an inert gas flows through the column. At $t = 0$, a step signal of pure or mixed gas

is sent through the column. The outlet concentration, inlet and outlet flows, pressure, pressure drop and temperature are recorded. This step signal continues for some time until the concentration and thermal breakthrough are finished. Breakthrough is when the inlet concentration is observed exiting the column. After thermal breakthrough, where the inlet temperature is observed at the outlet, the column is saturated with the adsorbing gas. The resulting response is due to adsorption onto the adsorbent. After breakthrough, at some time $t > t_{ads}$, the step signal of adsorbing gas is turned off and an inert gas passes through the column again. The observed response is due to desorption.

A mass balance around the column gives the equilibrium after breakthrough. The process is transient and there is accumulation of mass within the column. Since there is no reaction within the column, a mole balance can be performed.

$$n_{in} - n_{out} = n_{acc} \tag{2.11}$$

The accumulation, n_{acc}, is the difference between the moles entering the column, n_{in}, and the moles leaving the column, n_{out}. A graphical representation of the accumulation is shown in Figure 2.6. Part of the accumulation is in the solid phase and the remaining amount is in the fluid. Assuming that the ideal gas law is valid, the individual terms can be expanded to Equation 2.12.

$$\int_0^{t_{ads}} \left(\frac{y_{i,in} P_{in} Q_{in}}{R T_{in}} \right) dt - \int_0^{t_{ads}} \left(\frac{y_{i,out} P_{out} Q_{out}}{R T_{out}} \right) dt = m_{ads} q_i^* + \frac{y_{i,in} P_{avg}}{RT} V_b \epsilon + \frac{y_{i,in} P_{avg}}{RT} V_d \tag{2.12}$$

In Equation 2.12, y_i is the mole fraction of gas i, P is the total pressure, Q is the gas flowrate, T is the temperature, R is the universal gas constant, ϵ is the column void fraction, V_b is the total bed volume, V_d is the dead volume and q_i^* is the bulk equilibrium loading. Solving Equation 2.12 for q_i^* yields the equilibrium loading for the adsorbent for the particular set of conditions. For DCB experiments, only one equilibrium point is found per breakthrough. Dynamic column breakthrough experiments are used to validate the adsorption simulator, since these experiments provide the true adsorption dynamics for a particular system. Often, dynamic column breakthrough experiments must be corrected for dead volume to ensure the correct loadings are measured [26, 27]. This is especially important for weakly adsorbing components. The dead volume in the system can be characterized by the dead time in an non-adsorbing system, calculated in Equation 2.13.

$$t_d = \frac{L}{v} \tag{2.13}$$

A blank experiment is performed to determine the true column response, R_t. A blank experiment uses the same apparatus as the dynamic column breakthrough experiment, shown in Figure 2.5, but without the column. Instead, the column is replaced with a small piece of tubing of negligible volume. Then a dynamic column breakthrough experiment is performed and recorded. An example of a blank response is shown in Figure 2.7 as R_d. The blank response mass balance can be integrated in the same way as Equation 2.12 to determine the dead volume of the system.

It is best to design a dynamic column breakthrough apparatus with as little dead volume as possible [27]. This blank response must be subtracted from the dynamic column breakthrough experiment to ensure that only intra-column effects are observed [27]. There are few methods to obtain the true column response [27, 28]. For this study, the point-by-point correction was used.
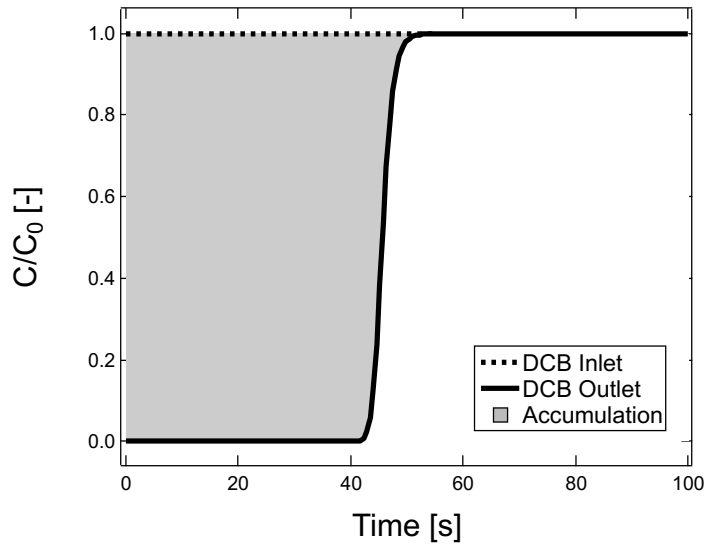
Figure 2.6: The accumulation, shown in gray, is the difference between the inlet and outlet dynamic column breakthrough concentrations at each time.
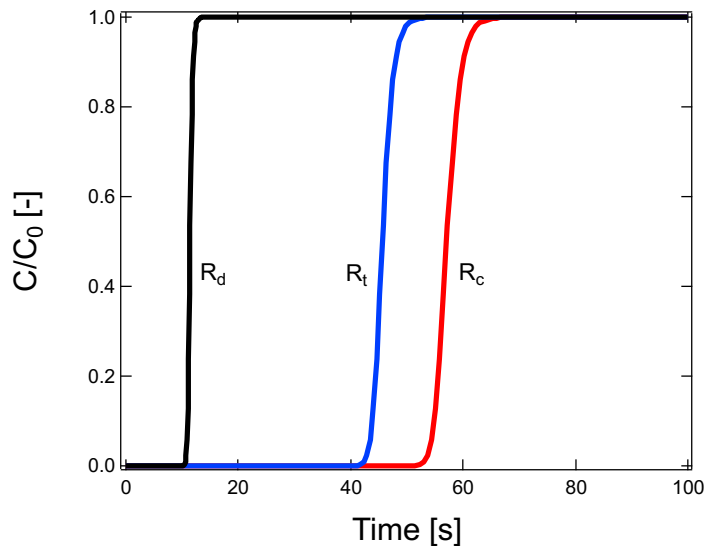
Figure 2.7: The blank (black), true (blue) and composite (red) responses of a hypothetical system.

To use the point-by-point correction, two responses are needed: a blank response, R_d, and a composite response, R_c, at the same conditions [28]. A composite response is a dynamic column

breakthrough experiment with dead volume contributions, as shown in Equation 2.14. The true column response is R_t.

$$R_c = R_d + R_t \tag{2.14}$$

The true response time is found in Equation 2.15 from the subtraction of the blank response from the composite response at a given concentration [28]. A graphical representation of this subtraction is shown in Figure 2.7.

$$R_t = R_c - R_d \tag{2.15}$$

2.3 Modeling Adsorption Equilibrium Data

After equilibrium data is collected, it is fit to an isotherm equation. An isotherm is an equilibrium model that describes adsorptive loading as a function of concentration at a given temperature. The isotherm can then be used in process simulations to predict adsorbent behavior.

2.3.1 Isotherm Types

Equilibrium data can come in many varieties. The Brunauer classifications are shown in Figure 2.8 and are normalized by the gas' saturation pressure, p_s [13, 29].
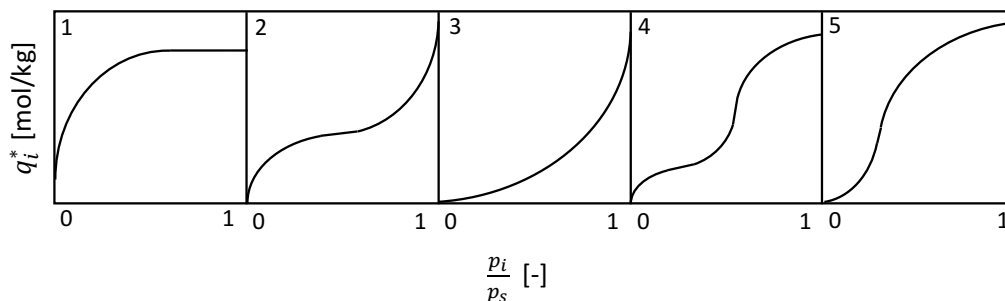
Figure 2.8: Brunauer isotherm types adapted from the literature [13, 29].

Most materials fall under the type 1 class. Type 1 materials adsorb gas until a saturation capacity is reached. This is observed when the pore size of the adsorbent micropores is only slightly larger than the size of the molecule [13]. Most isotherm models were defined or derived for type 1 behavior. Type 2 and 3 isotherm behavior is found when condensation within the adsorbent occurs [29]. Type 4 isotherm behavior steams from multilayer adsorption that occurs only after saturation of the first layer; generally a larger pore is filled completely before a smaller pore is then filled [13]. Type 5 isotherms are found when intermolecular attractions between pores are extremely strong [13].

2.3.2 Langmuir Isotherm

The Langmuir model, that describes type 1 behavior, is the most well known and widely used isotherm model [30].

$$q_i^* = \frac{q_i^{sat} b_i p_i}{1 + \sum_{i=1}^{n_{comp}} b_i p_i} \tag{2.16}$$

q_i^{sat} is the saturation capacity of component i on the adsorbent, b_i is the nonlinearity constant and p_i is the partial pressure of gas i. The isotherm can be derived by equating the rate equations for adsorption and desorption. The Langmuir isotherm assumes that there are a finite number of binding sites, that each binding site is energetically identical, each site contains only one adsorbed molecule and lateral energies between sites do not exist [31]. Often the Langmuir isotherm is extended to be dependent on temperature [32]; this is thermodynamically incorrect, but works well as an empirical model [31]. For temperature dependence, b_i is fit to an Arrhenius model.

$$b_i = b_{i,0} exp\left(\frac{-\Delta H}{RT}\right) \tag{2.17}$$

$b_{i,0}$ is the Arrhenius prefactor and ΔH is the heat of adsorption. For a Langmuir isotherm, ΔH is constant and selectivity between two components is constant. The selectivity, $\alpha_{1,2}$, is defined in Equation 2.18 as the ratio of a component's loading to a second component's loading.

$$\alpha_{1,2} = \frac{q_1^*}{q_2^*} \tag{2.18}$$

If more than one component is present, the Langmuir isotherm can be extended to be the competitive Langmuir isotherm. This is shown as the sum in the denominator of Equation 2.16. Only the single component constants of each gas are needed to use the competitive Langmuir isotherm.

An adsorbent's surface area, S_A, can be determined from the saturation capacity, q_i^{sat}, in the Langmuir isotherm. This surface area is called the Langmuir surface area, $S_{A,Lang}$, and is found by Equation 2.19 [33].

$$S_{A,Lang} = \frac{q_i^{sat} N_a A_{x,i}}{MW_i} \tag{2.19}$$

In Equation 2.19, N_a is Avogadro's number, $A_{x,i}$ is the adsorbate's cross sectional area and MW_i is the adsorbate's molecular weight. One major assumption that the Langmuir surface area makes is that all adsorbed gas is adsorbed onto a single layer [33].

2.3.3 Linear Isotherm

At low pressures the Langmuir isotherm collapses to a linear isotherm, shown in Equation 2.20.

$$q_i^* = q_i^{sat} b_i p_i = \mathcal{H}_i p_i \tag{2.20}$$

In this case, the product of q_i^{sat} and b_i is the Henry's constant, $\mathcal{H}_i$. The linear isotherm is particularly useful when a component is very weakly adsorbing. The linear isotherm is only thermodynamically consistent as a limiting case at low pressures.

2.3.4 Dual-Site Langmuir Isotherm

Many real adsorbents do not strictly follow the Langmuir isotherm, usually because adsorbents are not homogenous. The dual-site Langmuir isotherm is essentially the Langmuir isotherm, but with two types of binding sites that are energetically different.

$$q_i^* = \frac{q_{i,b}^{sat} b_i p_i}{1 + \sum_{i=1}^{n_{comp}} b_i p_i} + \frac{q_{i,d}^{sat} d_i p_i}{1 + \sum_{i=1}^{n_{comp}} d_i p_i} \tag{2.21}$$

Again, this model can be extended to be a function temperature.

$$b_i = b_{i,0} exp\left(\frac{-\Delta H_b}{RT}\right) \tag{2.22}$$

$$d_i = d_{i,0} exp\left(\frac{-\Delta H_d}{RT}\right) \tag{2.23}$$

However, now the model does not have a constant selectivity. The dual-site Langmuir isotherm can also be extended to become a competitive dual-site Langmuir isotherm. Like before, all that is needed are the pure component dual-site constants. Competition is expressed again as the sums in the denominators of Equation 2.21.

2.3.5 Toth Isotherm

The Toth isotherm is an empirical isotherm model designed to deal with adsorbent heterogeneity [34]. Unlike the dual-site Langmuir isotherm, it is an empirical model [16, 34].

$$q_i^* = \frac{q_i^{sat} b_i p_i}{\left(1 + (b_i p_i)^t\right)^{\frac{1}{t}}} \tag{2.24}$$

As before, q_i^{sat} is the saturation loading and b_i is the nonlinearity constant. b_i can be made temperature dependent like in the Langmuir isotherm. The Toth isotherm performs especially well with very strongly adsorbing components [16]. While it is an empirical model, the lower thermodynamic limits are achieved [34]. At low loading, the Toth isotherm reduces to a linear isotherm. Even though it provides a very good fit to strongly adsorbing nonlinear equilibrium data, it can not be extended into a competitive isotherm easily.

2.3.6 LRC Isotherm

The loading ratio correlation, LRC, isotherm is similar to the Toth isotherm. However, now the partial pressure in the numerator and the denominator are exponentiated [35]. The LRC isotherm is shown in Equation 2.25.

$$q_i^* = \frac{q_i^{sat} b_i (p_i)^t}{1 + b_i (p_i)^t} \tag{2.25}$$

All parameters are defined using Arrhenius relationships, as shown in Equations 2.26 to 2.28.

$$q_i^{sat} = q_{i,0}^{sat} exp\left(\frac{-k_q}{RT}\right) \tag{2.26}$$

$$b_i = b_{i,0} exp\left(\frac{-\Delta H}{RT}\right) \tag{2.27}$$

$$t = t_{i,0} exp\left(\frac{-k_t}{RT}\right) \tag{2.28}$$

Like the Toth isotherm, the LRC isotherm is an empirical fit [35]. Due to these changes, it becomes very easy to fit a wide range of type 1 isotherms.

2.3.7 BET Isotherm

The Brunauer, Emmett and Teller, or BET, isotherm was first published in 1938 to describe multilayer adsorption [36]. The BET isotherm, shown in Equation 2.29, is categorized as a type 2 isotherm; the low pressure region is type 1, and the high pressure region is type 3 [13, 29].

$$q_i^* = \frac{q_i^{sat} b_i \frac{p_i}{p_s}}{\left(1 - \frac{p_i}{p_s}\right)\left(1 + (1 - b_i)\frac{p_i}{p_s}\right)} \tag{2.29}$$

A new parameter is added in the BET isotherm called the saturation pressure, p_s, that describes the pressure where, at a given temperature, pore condensation occurs. The nonlinearity term, b_i, can be described using an Arrhenius relation, as shown in Equation 2.17.

The BET isotherm is thermodynamically consistent. At pressures much lower than p_s, the isotherm collapses to a linear isotherm. It was derived using kinetic theory, like the Langmuir isotherm. The BET isotherm assumes that multilayer adsorption occurs through interactions between adsorbed molecules and gas phase molecules; also that equilibrium exists between the upper adsorbed layer and the bulk gas phase [36]. As the pressure approaches the saturation pressure, the amount of molecules adsorbed on top of each other goes to infinity [36].

The BET isotherm is commonly used to determine the surface area of adsorbents. This surface area is called the BET surface area, $S_{A,BET}$, shown in Equation 2.30 [33].

$$S_{A,BET} = \frac{q_i^{sat}(\frac{p_s}{p_i} - 1)N_a A_{x,i}}{MW_i} \tag{2.30}$$

The BET surface area has a correction that allows multilayer adsorption; it arises from the linearization of the BET isotherm. Due to this correction, the BET surface area is always smaller than the Langmuir surface area. This makes sense, since molecules are not limited to only single layer adsorption.

2.3.8 Quadratic-Langmuir Isotherm

The quadratic-Langmuir isotherm, shown in Equation 2.31, is a combination of both the quadratic and Langmuir isotherms; it provides a type 4 isotherm fit [37].

$$q_i^* = \frac{q_{1,i}^{sat} p_i(b_{1,i} + 2b_{2,i}p_i)}{1 + b_{1,i}p_i + b_{2,i}p_i^2} + \frac{q_{2,i}^{sat} b_{3,i}p_i}{1 + b_{3,i}p_i} \tag{2.31}$$

This isotherm model is empirical and only has limited application. It can be extended to multiple components [38].

2.3.9 Ideal Adsorbed Solution Theory

It is much easier to describe pure component equilibrium than competitive equilibrium on an adsorbent. It is also easier to collect pure component data than competitive data. To describe competitive adsorption, Meyers and Prausnitz developed the ideal adsorbed solution theory (IAST) [39]. IAST can describe competitive equilibrium with pure component equilibrium data. It works best when the loadings of both components are similar at given partial pressures of each gas. At equilibrium all binding sites will be filled. The fractional amount of an adsorbed component is the fractional loading, x_i. The sum of all component fractional loadings must be equal to 1.

$$\sum_{i=1}^{n_{comp}} x_i = 1 \tag{2.32}$$

The equilibrium between the adsorbent and the components, shown in Equation 2.33, is then described with an expression analogous to Raoult's Law.

$$y_i P = P_i^o(\pi) x_i \tag{2.33}$$

$P_i^o(\pi)$ is defined as the component pressure which all component spreading pressures, π, are the same. This is analogous to the vapor pressure in Raoult's law.

$$\int_0^{P_i^o(\pi)} \frac{q_i^o(p_i)}{p_i} dp_i = \frac{\pi A}{RT} \tag{2.34}$$

To close the overall mass balance the total loading must be determined.

$$\frac{1}{q_{tot}} = \sum_{i=1}^{n_{comp}} \frac{x_i}{q_i^o} \tag{2.35}$$

With these equations, known component partial pressures and single component isotherms, competitive equilibrium can be predicted. It's important to note these equations can be applied to any number of components in a mixture. Using IAST, the competitive Langmuir isotherm can be derived. The only condition to derive this isotherm is that the total loading of all sites must be the same for all components.

2.3.10 Virial Excess Mixing Coefficients

IAST works well for many systems, but it has it's limitations. As explained, IAST works best for a system where all components have a similar loadings at given partial pressures. If the loadings of a mixture of gases are very different at their respective partial pressures, IAST starts to break down. In this case, IAST will over and underpredict the loading of the weaker component significantly. To improve competitive predictions in these cases, Qi and LeVan developed a method they called the Virial Excess Mixing Coefficient (VEMC) corrections [40].

VEMC is an extension of IAST when a system does not mix ideally. The spreading pressure relation can be broken into parts to show the ideal and mixing portions for a binary system, shown in Equation 2.36.

$$\frac{\pi A}{RT} = \left(\frac{\pi A}{RT}\right)_1 + \left(\frac{\pi A}{RT}\right)_2 + \left(\frac{\pi A}{RT}\right)_{mix}^{ideal} + \left(\frac{\pi A}{RT}\right)_{mix}^{ex} = \left(\frac{\pi A}{RT}\right)_{IAST} + \left(\frac{\pi A}{RT}\right)_{mix}^{ex} \qquad (2.36)$$

The excess mixing spreading relation can be extended using virial mixing coefficients, shown in Equation 2.37 [40]. These would be fitted using experimentally measured competitive isotherm data.

$$\frac{\pi A}{RT} = \left(\frac{\pi A}{RT}\right)_{IAST} + \frac{2}{A}B_{12}^{ex}q_1q_2 + \frac{3}{A^2}C_{112}^{ex}q_1^2q_2 + \frac{3}{A^2}C_{122}^{ex}q_1q_2^2 \qquad (2.37)$$

To determine competitive binary loadings, the pure component isotherms must be found first for each species in the system. Then for a set of partial pressures ($p_{IAST,1}$ and $p_{IAST,2}$), perform IAST, Equations 2.32 to 2.35. After the loadings for each component is found using IAST, the partial pressures will be adjusted using VEMC in Equations 2.38 and 2.39 [40].

$$ln(p_{VEMC,1}) = ln(p_{IAST,1}) + \frac{2}{A}B_{12}^{ex}q_2 + \frac{3}{A^2}C_{112}^{ex}q_1q_2 + \frac{3}{2A^2}C_{122}^{ex}q_2^2 \qquad (2.38)$$

$$ln(p_{VEMC,2}) = ln(p_{IAST,2}) + \frac{2}{A}B_{12}^{ex}q_1 + \frac{3}{A^2}C_{122}^{ex}q_1q_2 + \frac{3}{2A^2}C_{112}^{ex}q_1^2 \qquad (2.39)$$

For a set of partial pressures, $p_{VEMC,1}$ and $p_{VEMC,2}$, the equilibrium loadings, q_1 and q_2, are found. Unfortunately, these VEMC corrections make the system implicit; the given IAST partial pressures are not the VEMC partial pressures at the competitive equilibrium.

2.3.11   Isosteric Heat of Adsorption

The isosteric heat of adsorption, ΔH_{iso}, shows the amount of energy released during adsorption [41]. The isosteric heat of adsorption can be found using the Clausius-Clapeyron equation, shown in Equation 2.40, after equilibrium data has been collected.

$$\left[\frac{\partial ln(p_i)}{\partial(1/T)}\right]_{q_i} = -\frac{\Delta H_{iso}}{R} \qquad (2.40)$$

ΔH_{iso} is a function of loading, q_i. A useful graph shows the dependence of ΔH_{iso} on q_i. If an increase in ΔH_{iso} is observed with increasing loading, then adsorption becomes more favorable due lateral interactions between adsorbed molecules [41]. The opposite is true if ΔH_{iso} decreases with increasing loading. ΔH_{iso} becomes the heat of adsorption, ΔH, at very low loadings [13].

The Langmuir isotherm model expresses a constant ΔH_{iso} for any loading; in this case, $\Delta H_{iso} = \Delta H$. Any material that shows a constant ΔH_{iso} is said to be energetically homogenous. In this case the Langmuir isotherm should work fairly well [31]. In any other case, the adsorbent is energetically heterogeneous.

2.4 Process Simulation

It is necessary to optimize adsorbent cycles before they are implemented at the industrial scale. Using a simulator can greatly reduce the amount of time required to physically optimize a process to achieve the desired separation. Optimization can also determine the adsorbents that perform best for a particular process. To perform a process optimization, a model must be developed and validated. The process simulator for this study was developed in MATLAB using finite volume techniques. This simulator is fast and able to handle stiff problems associated with adsorbent processes [9].

2.4.1 Model Equations

A simulator was developed in MATLAB to model column dynamics obtained by dynamic column breakthrough experiments [9, 42]. The simulator assumes the following:

1. The gas phase is ideal

2. The column is one-dimensional and there are no radial gradients for concentration or temperature

3. An axially dispersed plug flow model adequately describes the flow through the column

4. The ambient temperature is uniform

5. Darcy's law adequately describes the pressure drop in the column

6. The gas and solid phases achieve thermal equilibrium instantaneously

7. Adsorbent and bed properties are uniform throughout the column

8. The linear driving force model adequately describes the solid phase mass transfer rate

With these assumptions, the gas phase component mass balance is constructed in Equation 2.41. This gas phase mass balance accounts for dispersive, convective and adsorptive effects within the column.

$$\frac{\partial c_i}{\partial t} = \frac{\partial}{\partial z}\left(cD_L \frac{\partial y_i}{\partial z} + c_i v\right) - \frac{1 - \epsilon}{\epsilon}\frac{\partial q_i}{\partial t} \tag{2.41}$$

For the dependent variables, z is the axial length and t is the time. For the independent variables, c is the concentration of gas, i denotes the component, y is the gas phase mole fraction, v is the interstitial velocity, ϵ is the bed void fraction and q is the loading and D_L is the axial dispersion coefficient. If the ideal gas law is assumed, c in Equation 2.41 can be expanded. For an ideal gas $c = \frac{P}{RT}$, where P is the pressure, R is the universal gas constant and T is the temperature.

$$\frac{\partial y_i}{\partial t} + \frac{y_i}{P}\frac{\partial P}{\partial t} - \frac{y_i}{T}\frac{\partial T}{\partial t} = D_L\frac{T}{P}\frac{\partial}{\partial z}\left(\frac{P}{T}\frac{\partial y_i}{\partial z}\right) - \frac{T}{P}\frac{\partial}{\partial z}\left(\frac{y_i P}{T}v\right) - \frac{RT}{P}\frac{1 - \epsilon}{\epsilon}\frac{\partial q_i}{\partial t} \tag{2.42}$$

If all component mass balances are summed, the overall mass balance, Equation 2.43, is found.

$$\frac{1}{P}\frac{\partial P}{\partial t} - \frac{1}{T}\frac{\partial T}{\partial t} = -\frac{T}{P}\frac{\partial}{\partial z}\left(\frac{P}{T}v\right) - \frac{RT}{P}\frac{1-\epsilon}{\epsilon}\sum_{i=1}^{n_{comp}}\frac{\partial q_i}{\partial t} \tag{2.43}$$

Mass transfer in the solid phase is described by the linear driving force model.

$$\frac{\partial q_i}{\partial t} = k_i(q_i^* - q_i) \tag{2.44}$$

q^* is the equilibrium loading, q is the loading in the column at some time and k_i is the mass transfer coefficient. Darcy's law describes the axial pressure drop across the column.

$$-\frac{\partial P}{\partial z} = \frac{150}{4}\frac{1}{r_p^2}\left(\frac{1-\epsilon}{\epsilon}\right)^2\mu v \tag{2.45}$$

r_p is the particle radius and μ is the viscosity which is assumed to be constant during the process. The column energy balance includes thermal effects due to conduction through the column wall, convection along the bed and adsorption.

$$\left[\frac{1-\epsilon}{\epsilon}(\rho_s C_{p,s} + C_{p,a}\sum_{i=1}^{n_{comp}}q_i)\right]\frac{\partial T}{\partial t} = \frac{K_z}{\epsilon}\frac{\partial^2 T}{\partial z^2} - \frac{C_{p,g}}{R}\frac{\partial}{\partial z}(vP) - \frac{C_{p,g}}{R}\frac{\partial P}{\partial t}$$
$$-\frac{1-\epsilon}{\epsilon}C_{p,a}T\sum_{i=1}^{ncomp}\frac{\partial q_i}{\partial t} + \frac{1-\epsilon}{\epsilon}\sum_{i=1}^{ncomp}\left[(-\Delta H_i)\frac{\partial q_i}{\partial t}\right] - \frac{2h_{in}}{\epsilon r_{in}}(T-T_w) \tag{2.46}$$

ρ_s is the particle density, $C_{p,s}$ is the solid heat capicity, $C_{p,g}$ is the gas heat capacity, $C_{p,a}$ is the adsorbed phase heat capacity, K_z is the thermal conductivity of the gas, ΔH_i is the heat of adsorption of component i, h_{in} is the internal heat transfer coefficient, r_{in} is the internal radius of the column and T_w is the column wall temperature. T_w is found from Equation 2.47.

$$\rho_w C_{p,w}\frac{\partial T_w}{\partial t} = K_w\frac{\partial^2 T_w}{\partial z^2} + \frac{2r_{in}h_{in}}{r_{out}^2 - r_{in}^2}(T-T_w) - \frac{2r_{out}h_{out}}{r_{out}^2 - r_{in}^2}(T_w - T_{amb}) \tag{2.47}$$

ρ_w is the density of the column wall, $C_{p,w}$ is the heat capacity of the column wall, K_w is the thermal conductivity of the column wall, r_{out} is the external radius of the column wall, h_{out} is the external heat transfer coefficient and T_{amb} is the ambient temperature outside of the column.

D_L is a lumped parameter that is a combination of the molecular diffusion, D_m, and turbulent mixing which is shown as the multiplication of the interstitial velocity, v, and particle diameter, d_p [13]. D_m can be determined by the Chapman-Enskog equation [43].

$$D_L = 0.7D_m + 0.5vd_p \tag{2.48}$$

k_i is a lumped parameter for macropore diffusion resistance [13, 44].

$$k_i = \frac{15\epsilon_p D_p}{r_p^2} \tag{2.49}$$

ϵ_p is the particle void fraction and D_p is the macropore diffusivity, which is a function of molecular diffusion and the adsorbent tortuosity, τ.

$$D_p = \frac{D_m}{\tau} \tag{2.50}$$

2.4.2 Boundary Conditions

Three types of boundary conditions are defined in the simulator, all are shown in Figure 2.9.
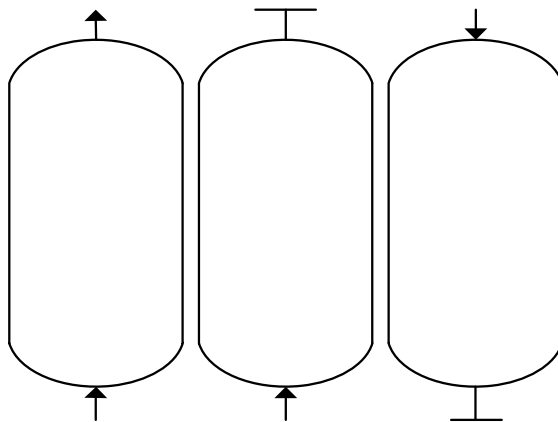
Figure 2.9: The three types of boundary conditions (from left to right): open-open, open-closed and closed-open.

The open-open boundary condition is used to simulate an adsorption step, or any other step where gas flows through the column. The inlet concentration is known and pressure at the outlet of the column is maintained at a certain value. The inlet for the component mass balance can be represented with Danckwert's boundary conditions for dispersed flow, shown in Equations 2.51 to 2.52 [9].

$$D_L \frac{\partial y_i}{\partial z}\bigg|_{z=0} = -v|_{z=0}(y_{i,feed} - y_i|_{z=0}) \tag{2.51}$$

$$\frac{\partial y_i}{\partial z}\bigg|_{z=L} = 0 \tag{2.52}$$

The same idea can be applied to the heat transfer equations, resulting in Equations 2.53 to 2.54 [9].

$$K_z \frac{\partial T}{\partial z}\bigg|_{z=0} = -\epsilon v|_{z=0}\rho_g C_{p,g}(T_{feed} - T|_{z=0}) \tag{2.53}$$

$$\frac{\partial T}{\partial z}\bigg|_{z=L} = 0 \tag{2.54}$$

The wall boundary conditions are formed using Dirichlet boundary conditions, assuming that at $z = 0$ and $z = L$ the column has a large thermal capacity [9].

$$T_w|_{z=0} = T_w|_{z=L} = T_{amb} \tag{2.55}$$

Since the total mass balance is second order with respect to pressure, two boundary conditions for pressure are needed. The column effluent pressure is controlled in the most real apparatuses, resulting in Equation 2.56. From Darcy's law, velocity is a function of the pressure gradient yielding Equation 2.57.

$$P|_{z=L} = P_H \tag{2.56}$$

$$v|_{z=0} = v_{feed} \tag{2.57}$$

Open-closed boundary conditions are applied when the column needs to be pressurized [9]. The only boundary condition that will change is the pressure at the outlet, shown in Equation 2.56. This now should be a Nuemann boundary condition, Equation 2.56 becomes Equation 2.58.

$$\left.\frac{\partial P}{\partial z}\right|_{z=L} = 0 \tag{2.58}$$

A closed-open case is needed for reverse-pressurization. All boundary conditions for the open-open case will stay the same, except for Equations 2.51 and 2.53, which change to Equations 2.59 and 2.60 respectively.

$$\left.\frac{\partial y_i}{\partial z}\right|_{z=0} = 0 \tag{2.59}$$

$$\left.\frac{\partial T}{\partial z}\right|_{z=0} = 0 \tag{2.60}$$

Also, since $v_{feed} = 0$ at the inlet, the pressure at the inlet becomes Equation 2.60.

$$\left.\frac{\partial P}{\partial z}\right|_{z=0} = 0 \tag{2.61}$$

2.5 Conclusions

The experimental methods for collecting adsorbent equilibrium data and dynamics were explained in detail for volumetry, gravimetry and dynamic column breakthrough. These experiments are essential to the following chapters. A brief discussion on the types of equilibrium data and isotherms were detailed. A series of thermodynamic and empirical isotherm models were presented to model collected equilibrium data. Advantages and disadvantages of these models were explained. A non-isothermal, non-isobaric in-house adsorption simulator was presented to compare simulated and experimental dynamic column breakthrough experiments. The simulator can produce temperature, pressure, fluid and solid concentration profiles in an adsorbent bed.

Chapter 3

Characterization of TDA 2015 − An Adsorbent for Pre-Combustion Carbon Capture

3.1   Introduction

In a pre-combustion carbon capture process, a fuel is gasified to produce syngas, which is primarily CO and H_2. Syngas is made through the water-gas shift reaction, where the fuel is partially combusted by carefully controlling the O_2 concentration in the gasifier feed [45]. CO is then passed through a catalytic converter to produce CO_2. The CO_2 is captured to yield a high purity stream of H_2, which is used as a fuel in a gas turbine to generate energy. Generally the feed concentration of CO_2 is between 15-60 mol% and 20-70 bar total pressure [8]. Due to these conditions, normally weak adsorbents, such as activatived carbons, can be utilized for CO_2 capture. Since CO_2 is separated at a high pressure, the energy consumption and the CO_2 compression costs are reduced [8]. Examples of adsorptive pre-combustion carbon capture already exist; most notably the plant in Port Arthur, Texas that captures 1 Mt/year of CO_2 [8]. Some limitations do exist for pre-combustion capture, the main one being how few pre-combustion power plants there are in operation around the world [7].

To utilize these opportunities, adsorbents must be developed for pre-combustion capture. Activated carbons have been strongly considered due to their physical properties and low cost [46,47]. Activated carbons normally have very linear loadings at vacuum pressures [46]. CO_2 uptake becomes much stronger at elevated pressures for activated carbons; this facilitates desorption as well [47]. CO_2 uptake in activated carbons could be as high as 60-70 wt% in pre-combustion conditions [48]. The US Department of Energy granted funding to TDA Research Inc. to develop pre-combustion carbon capture adsorbents. This chapter details the characterization of one of their new adsorbents, TDA 2015.

3.2 Adsorption Equilibrium on TDA 2015

TDA 2015 is an activated carbon that is synthesized by TDA Research Inc. (Wheat Ridge, CO, USA). Adsorption equilibrium data was collected for TDA 2015 using volumetry (Micromeritics ASAP 2020, Norcross, GA, USA) at pressures below 1.2 bar and a dynamic column breakthrough apparatus for high pressures.

3.2.1 Equilibrium Data

At this stage, only pure CO_2 equilibrium has been characterized on TDA 2015. H_2 is very weakly adsorbed on TDA 2015, so for this study it will be neglected. Figure 3.1a shows a summary of the equilibrium data used around the conditions for a pre-combustion process. Figure 3.1b contains more CO_2 loadings at lower temperatures; most data in this figure are not within the process' operating range. As seen in Figures 3.1a and b, the CO_2 loadings at low partial pressures seem to be consistent with a type 1 isotherm [13]. However, at higher loadings, the isotherm might have a type 3 shape, making it a BET isotherm (type 2) [13, 36].
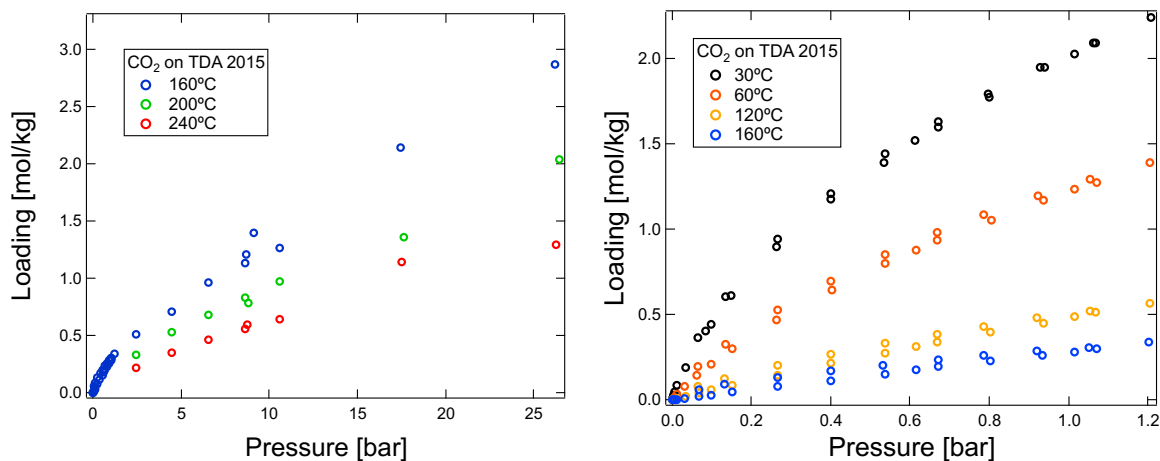
(a) CO_2 equilibrium data at the proposed process conditions

(b) Additional CO_2 data at lower temperatures

Figure 3.1: CO_2 loadings on TDA 2015 from 30 to 240°C collected via volumetry and dynamic column breakthrough. Data up to 1.2 bar was collected via volumetry. Above 1.2 bar, equilibrium was measured using dynamic column breakthrough.

The equilibrium data was fit between 0 and 12 bar to a range of isotherm models. As explained in Chapter 2, the Langmuir isotherm is the simplest model; therefore, the equilibrium data was fit to a Langmuir isotherm as a preliminary check on the adsorbent's homogeneity. All isotherm models used in this study are shown in Table 3.1. The parameters are shown in Table 3.2.

Table 3.1: Isotherm models used to fit CO_2 equilibrium data on TDA 2015. In the Langmuir, LRC and BET isotherms $b_i = b_0 e^{\left(\frac{-\Delta U}{RT}\right)}$. In the LRC isotherm, $q_i^{sat} = q_0^{sat} e^{\left(\frac{-k_q}{RT}\right)}$ and $t = t_0 e^{\left(\frac{-k_t}{RT}\right)}$.

Langmuir isotherm	$q_i^* = \frac{q_1^{sat} b_i C_i}{1 + \sum_{i=1}^{n_{comp}} b_i C_i}$
LRC isotherm	$q_i^* = \frac{q_1^{sat} b_i (C_i)^t}{1 + b_i (C_i)^t}$
BET isotherm	$q_i^* = \frac{q_1^{sat} b_i \frac{p_i}{p_s}}{\left(1 - \frac{p_i}{p_s}\right)\left(1 + (1-b_i)\frac{p_i}{p_s}\right)}$
Quadratic-Langmuir isotherm	$q_i^* = \frac{q_1^{sat} C_i (b_1 + 2b_2 C_i)}{1 + b_1 C_i + b_2 C_i^2} + \frac{q_2^{sat} b_3 C_i}{1 + b_3 C_i}$

As seen in Figure 3.2a, the Langmuir isotherm does not fit the data well at higher pressures and at lower temperatures; however, at lower pressures and higher temperatures, the Langmuir isotherm fits the experimental data well. This shows there is some heterogeneity in the adsorbent binding sites [31]. Not all binding sites will be energetically identical. To account for heterogeneity, the data was fit to a LRC isotherm, shown in Figure 3.2b. The parameters are shown in Table 3.2. As explained in Chapter 2, the LRC isotherm is an empirical fit. Therefore, the LRC isotherm is not thermodynamically consistent like the Langmuir isotherm [31]. Despite these drawbacks, the isotherm fit is greatly improved.

Table 3.2: CO_2 isotherm parameters for different isotherm models on TDA 2015. Note that b_0 is unitless in the BET isotherm.

Parameter	Langmuir	LRC	BET	Quadratic-Langmuir
q_0^{sat} [mol/kg]	-	0.2544	-	-
q_1^{sat} [mol/kg]	6.085	-	2.511	0.80
q_2^{sat} [mol/kg]	-	-	-	1.40
b_0 [m^3/mol]	1.46×10^{-6}	3.45×10^{-4}	1.36×10^{-3} [-]	-
b_1 [m^3/mol]	-	-	-	-3.50×10^{-3}
b_2 [m^6/mol^2]	-	-	-	6.57×10^{-6}
b_3 [m^3/mol]	-	-	-	1.49×10^{-2}
k_q [kJ/mol]	-	-10.01	-	-
k_t [kJ/mol]	-	0.4672	-	-
ΔU [kJ/mol]	-24.56	-5.559	-30.27	-
p_s [Pa]	-	-	6.99×10^6	-
t_0 [-]	-	0.9900	-	-

There were some discrepancies in the equilibrium data at higher pressures of CO_2. Due to these discrepancies, a BET isotherm was fit, as seen in Figure 3.2c. The BET isotherm is shown in Table 3.1. However, the fit was not able to capture the equilibrium data like the LRC isotherm. The equilibrium data suggests that the isotherm is type 1, not type 2.

Although the data appears to be type 1, the quadratic-Langmuir isotherm, a type 4 isotherm, was also fit. The quadratic-Langmuir model is shown in Table 3.1. The isotherm parameters are found in Table 3.2. The quadratic-Langmuir isotherm was only fit for one temperature (160°C), shown in Figure 3.2d, to use in a case study that will be explained later this chapter. As seen in Figure 3.2d, this isotherm fit is poor. The loadings are equal only at low pressures and 10.56 bar. Again, this confirms that the equilibrium data is type 1.

(a) Langmuir isotherm

(b) LRC isotherm

(c) BET isotherm

(d) Quadratic-Langmuir isotherm
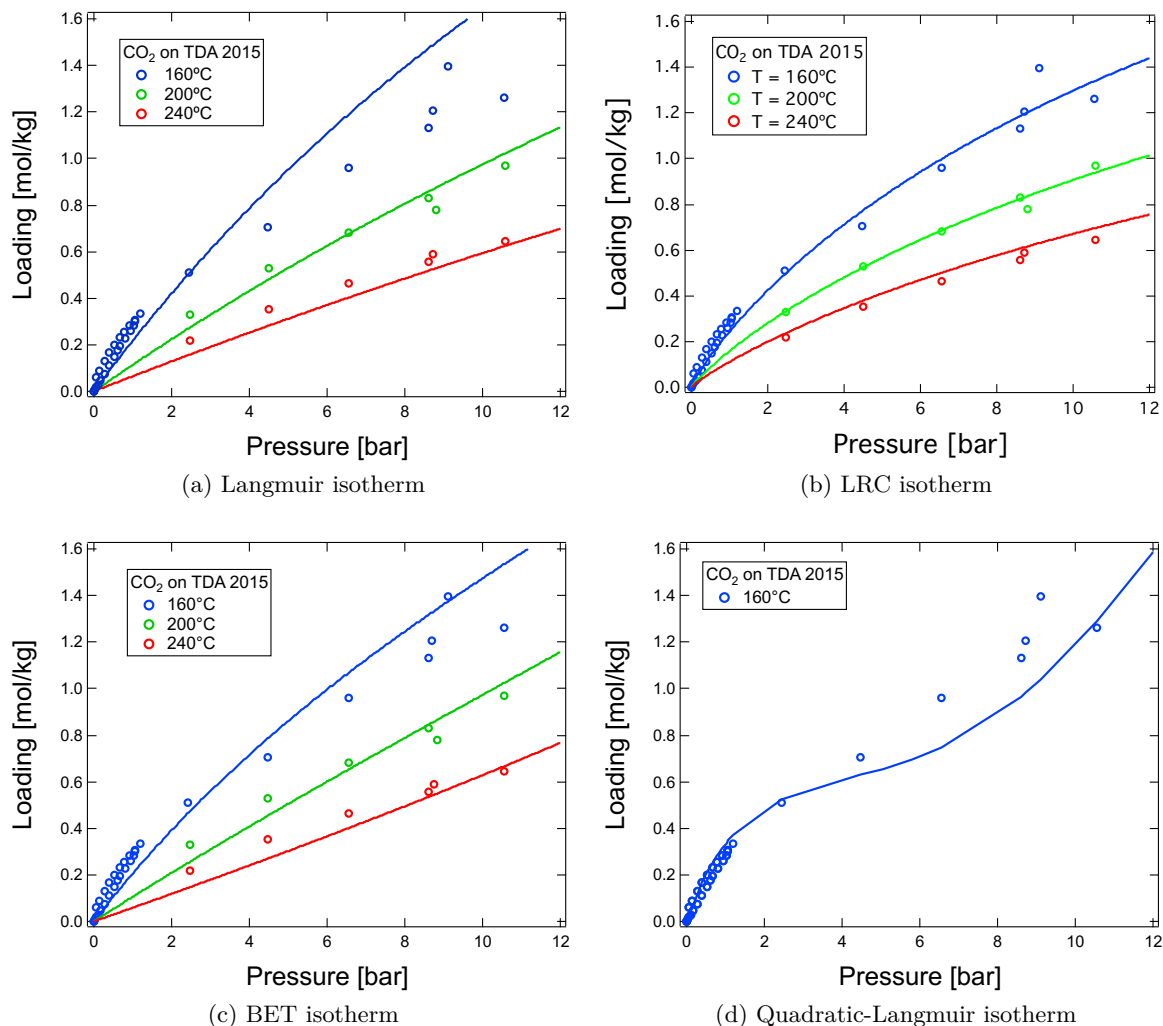
Figure 3.2: CO_2 isotherms on TDA 2015 fit to different isotherm models.

3.2.2 Isosteric Heat of Adsorption

The isosteric heat of adsorption was determined via the volumetry and dynamic column break-through equilibrium data. Figure 3.3 was found using the Clausius-Clapeyron equation, shown

in Equation 3.1.

$$\left[\frac{\partial ln(p_i)}{\partial (1/T)}\right]_{q_i} = -\frac{\Delta H_{iso}}{R} \qquad (3.1)$$

The volumetry equilibrium experiments at lower temperatures (30, 60, 120 and 160°C) show that with increasing loading, the isosteric heat decreases. At higher pressures, the isosteric heat is more ambiguous depending on the isotherm chosen isotherm fit. Less energy is released as loading increases, until ≈ 0.2 to 0.3 mol/kg, where the energy released is constant or increasing, depending on the model. This shows that adsorption is more energetically favorable as adsorbent loading increases [41].
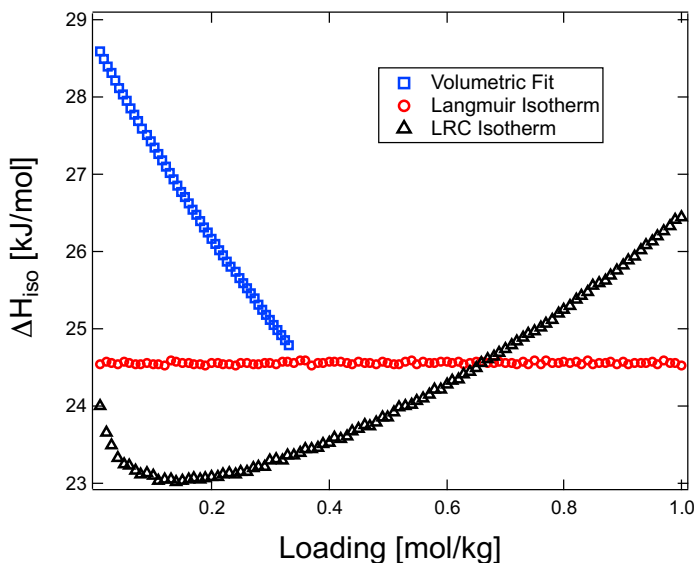
Figure 3.3: The isosteric heat of adsorption, ΔH_{iso}, for CO_2 on TDA 2015. The blue curve was determined using an empirical fit of low temperature (30, 60, 120 and 160°C) volumetric equilibrium data. The red curve was determined using the Langmuir isotherm, this value is constant within the solver's error tolerances. The black curve was determined using the LRC isotherm.

3.3 Dynamic Column Breakthrough

A series of dynamic column breakthrough experiments were performed in an apparatus similar to Figure 2.5. The main difference between Figure 2.5 and the experimental apparatus used in this study is the removal of the mass spectrometer and the addition of two CO_2 analyzers (NOVA, Niagara Falls, NY, USA and CAI, Orange, CA, USA). The NOVA analyzer can measure CO_2 mole fractions from 0 to 0.35 and the CAI analyzer can measure the full scale of mole fractions. The inlet flowrate was fixed to 2.2 SLPM for breakthrough experiments. Desorption experiments were also performed. After CO_2 breakthrough occurs, the flow is changed to pure He. After some time the CO_2 concentration decreases to zero.

3.3.1 CO₂ Breakthrough Measurements

The dynamic column breakthrough experiments were performed on TDA 2015 at $\approx$ 160, 200 and 240°C and $\approx$ 2.5, 4.5, 6.5, 8.5 and 10.5 bar of CO_2 on an apparatus at TDA Research Inc. A summary of these experiments is shown in Table 3.3. All experiments were repeatable. Helium was used as a carrier gas. A thermocouple was located near the end of the column (80% down the length of the column). All experiments were then simulated using our in-house simulator. The results are shown in Figure 3.4. The LRC isotherm was used in the simulations to model CO_2 equilibrium.

Table 3.3: A summary of the CO_2 breakthrough experiments on TDA 2015.

T [°C]	P_{CO_2} [bar]	P [bar]	q^*_{exp} [mol/kg]	q^*_{sim} [mol/kg]	Error [%]
164	2.44	8.13	0.5087	0.4913	3.34
167	4.48	14.93	0.7042	0.7164	1.74
165	6.56	21.87	0.9587	0.97501	1.71
165	8.91	29.70	1.1332	1.1744	3.63
165	10.56	35.20	1.2613	1.3257	5.11
203	2.46	8.20	0.3288	0.3322	1.03
203	4.49	14.97	0.5276	0.5444	3.19
204	6.56	21.87	0.6807	0.6978	2.51
204	8.61	28.70	0.8294	0.8852	6.73
204	10.57	35.23	0.9691	1.0553	8.90
241	2.47	8.23	0.2189	0.2160	1.32
240	4.49	14.97	0.3505	0.3414	2.58
241	6.57	21.90	0.4647	0.4492	3.34
241	8.62	28.73	0.5575	0.5168	7.73
242	10.58	35.27	0.6438	0.5784	10.17

The experimental parameters used in the simulator are shown in Table 3.4. The column used was an ANSI 2" diameter schedule 40 stainless steel pipe. The internal and external diameters were given by the manufacturer and checked with a caliper. The column was designed to be 12.5" (0.3175 m) long. The column's density, ρ_w, thermal conductivity, K_w, and specific heat capacity, $C_{p,w}$, were taken from the literature for stainless steel. The bulk density, ρ_{bulk}, was measured by weighing a volume of TDA 2015 from a graduated cylinder after the particles had been well packed. The particle density, ρ_p, and particle void fraction, ϵ_p, were measured using volumetry (Micromeritics, Norcross, GA, USA). The column void fraction, ϵ, was calculated via both the bulk and particle densities.

$$\epsilon = \frac{\rho_p - \rho_{bulk}}{\rho_p} \tag{3.2}$$

The tortuosity was assumed to be a value of 3 based on typical values reported in the literature [9, 49]. The gas' properties were determined using the thermodynamics program REFPROP. Heat transfer coefficients, h_{in} and h_{out}, were determined through a parameteric study to reduce

the error between experiment and simulation. They were within the range predicted by the Leva correlation [13]. The heat capacity of the adsorbed phase, $C_{p,a}$, was assumed to be the same as the specific heat capacity of the gas, $C_{p,g}$, since $C_{p,a}$ is difficult to measure. A sensitivity analysis showed that a 10% change of $C_{p,a}$ did not change the simulated results. The specific heat capacity of the adsorbent, $C_{p,s}$, was unknown; it was assumed to be the same as TDA AMS 19, a similar adsorbent by TDA Research [50].

Table 3.4: Simulation parameters for the TDA 2015 pre-combustion process.

Parameter	Value	Source
Column Properties		
column length, L [m]	0.3175	measured
inner column diameter, d_i [m]	5.258×10^{-2}	measured
outer column diameter, d_o [m]	6.033×10^{-2}	measured
column void fraction, ϵ	0.2505	measured
particle void fraction, ϵ_p	0.368	measured
tortuosity, τ	3	assumed
Properties and Constants		
universal gas constant, R [m^3 Pa mol^{-1} K^{-1}]	8.314	standard value
adsorbent particle density, ρ_p [kg m^{-3}]	830.5	measured
column wall density, ρ_w [kg m^{-3}]	7800	standard value
specific heat capacity, $C_{p,g}$ [J mol^{-1} K^{-1}]	1010.6	standard value
specific heat capacity of adsorbed phase, $C_{p,a}$ [J mol^{-1} K^{-1}]	1010.6	assumed
specific heat capacity of adsorbent, $C_{p,s}$ [J mol^{-1} K^{-1}]	1877.2	assumed
specific heat capacity of column wall, $C_{p,w}$ [J mol^{-1} K^{-1}]	502.0	standard value
fluid viscosity, μ [kg m^{-1} s^{-1}]	2.89×10^{-5}	standard value
molecular diffusion, D_m [m s^{-2}]	1.30×10^{-5}	standard value
effective gas thermal conductivity, K_z [W m^{-1} K^{-1}]	9.03×10^{-2}	assumed
thermal conductivity of column wall, K_w [W m^{-1} K^{-1}]	16.0	standard value
internal heat transfer coefficient, h_{in} [W m^{-2} K^{-1}]	25.0	fitted
external heat transfer coefficient, h_{out} [W m^{-2} K^{-1}]	25.0	fitted

As seen from Figure 3.4, the simulations were able to predict experiments at 2.5 and 4.5 bar of CO_2 quite well at all feed temperatures. These profiles all show classic shock transitions, associated with a type 1 isotherm. The adsorbent becomes saturated with almost no frontal dispersion for a shock transition; this is also called plug flow.

However, at high partial pressures of CO_2, ≥ 8.5 bar, the qualitative match between the experiments and simulations were not in agreement. Loadings were very similar for experiments and simulations, all had an error less than 10%. The concentration and temperature breakthrough profiles at pressures ≥ 8.5 bar of CO_2 are very dispersed. It appears that the concentration breakthrough dynamics have been broken into two parts for the high concentration feeds. First, a shock transition is seen, which is normal with a type 1 isotherm such as a Langmuir or LRC isotherm. Afterwards, the uptake of CO_2 seems to slow down, which yields the second, less sharp

slope. After some time, TDA 2015 becomes saturated with CO_2 and the exiting concentration reaches the feed concentration.

For every breakthrough experiment, a concentration desorption profile was also recorded. The results are in Figure 3.5. Desorption experiments were carried out in an nearly isothermal environment. Some time after the adsorbent had been saturated, the mixture of CO_2/He inlet was switched to pure He. These experiments were run until the CO_2 concentration was zero. From Figure 3.5 it appears that the desorption profiles are from a type 1 isotherm. A simple wave decay is what is expected from a type 1 isotherm [13]. The main observation from these desorption profiles is that there is no strange behavior in the concentration desorption profiles ≥ 8.5 bar CO_2.
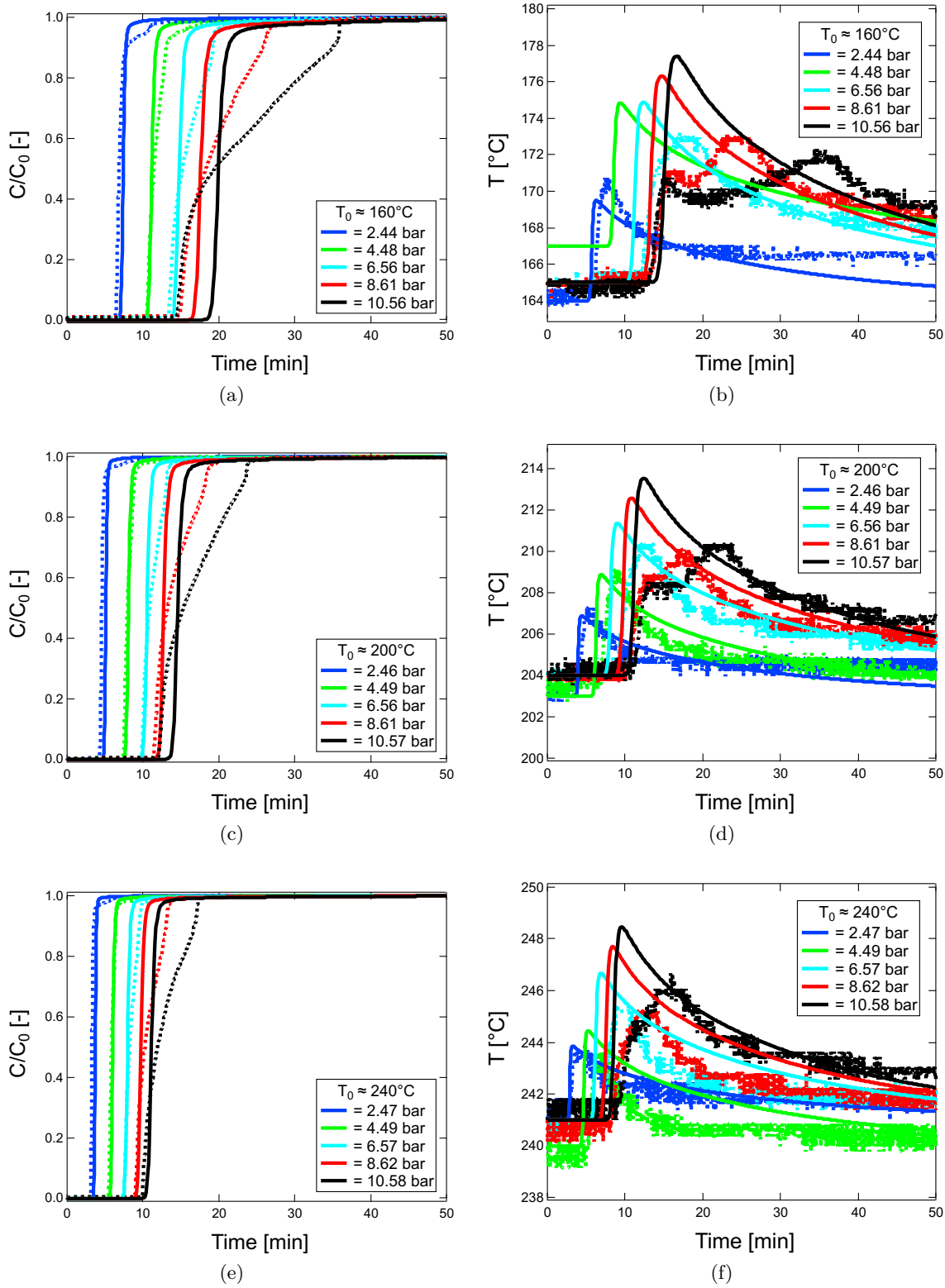
Figure 3.4: CO_2 concentration and temperature breakthrough profiles on TDA 2015 at $\approx$ 160, 200 and 240°C and $\approx$ 2.5, 4.5, 6.5, 8.5 and 10.5 bar of CO_2. $y_{CO_2,0} = 0.3$ for all experiments. Experiments are the dashed lines and simulations are the solid lines.
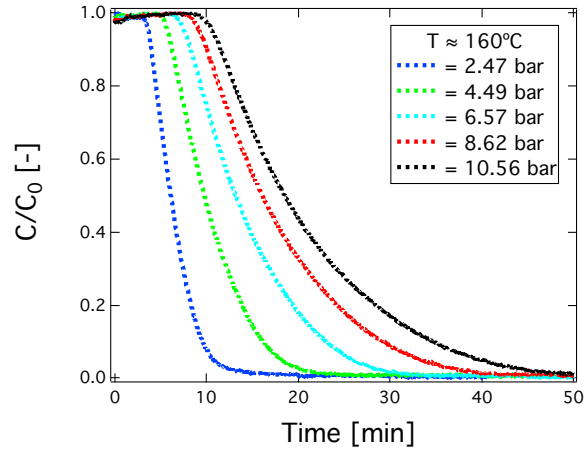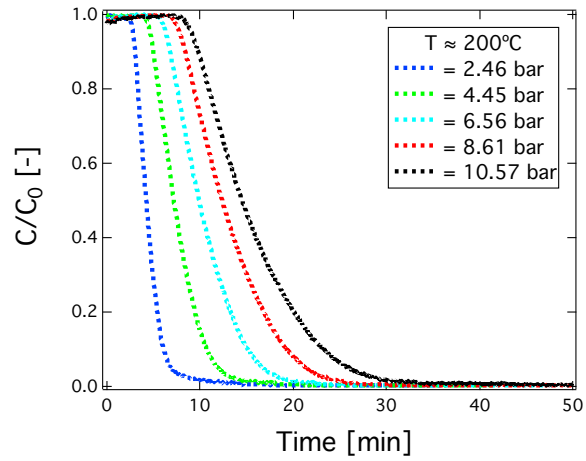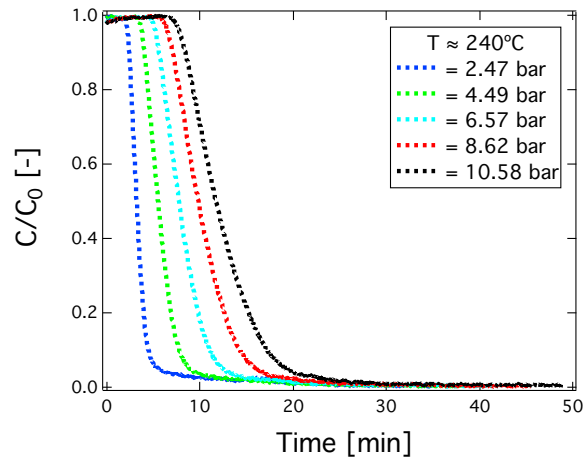
Figure 3.5: Experimental CO_2 concentration desorption profiles on TDA 2015 at $\approx$ 160, 200 and 240°C and $\approx$ 2.5, 4.5, 6.5, 8.5 and 10.5 bar of CO_2. $y_{CO_2,0} = 0.3$ for all experiments.

3.4 Qualitative Breakthrough Trends

At higher partial pressures of CO_2, the concentration and temperature breakthrough profiles become very dispersed. This is easily seen in Figure 3.4 for the highest two pressures at every temperature. After searching through the literature, there are a few of explanations for this behavior. The three main factors are mass transfer effects, heat effects and equilibrium effects.

3.4.1 Mass Transfer and Kinetic Effects

Mass transfer effects describe the resistance a gas molecule has when diffusing into an adsorbent. Kinetic effects describe how long the system takes to go to equilibrium. The mass transfer model used in this work is the linear driving force, shown in Equation 3.3

$$\frac{\partial q_i}{\partial t} = k_i(q_i^* - q_i) \tag{3.3}$$

where k_i is the lumped mass transfer coefficient. For the simulations, k_i includes all resistances due to microporous mass transfer [13, 44].

$$k_i = \frac{15\epsilon_p D_p}{r_p^2} \tag{3.4}$$

It is possible to extend k_i to include macropore and film resistances as well.

$$\frac{1}{k_i} = \frac{r_P H_i}{3k_f} + \frac{r_P^2 H_i}{15\epsilon D_p} + \frac{r_p^2}{15D_c} \tag{3.5}$$

In the extended model, r_P is the macropore radius, r_p is the particle radius, H_i is the Henry constant, k_f is the external film mass transfer coefficient, D_c is micropore diffusivity and D_p is the bulk molecular diffusivity [51]. k_i effects the concentration breakthrough profile's spread, as seen in Figure 3.6.
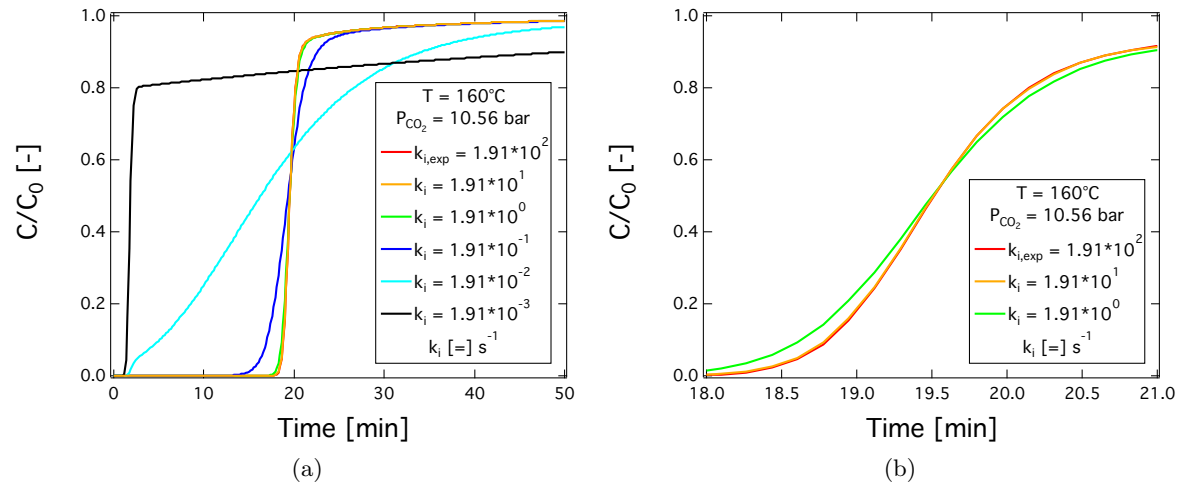
Figure 3.6: Simulated CO_2 breakthrough profiles on TDA 2015 using the LRC isotherm with a variable k_i at 160°C and 10.56 bar. (a) contains a wide range of k_i values, while (b) shows a zoomed view of large k_i values.

Depending on the size of the micropores, there could be heavy mass transfer resistance within the adsorbent [51]. This is usually observed in kinetic systems, such as carbon molecular sieves, where the adsorbent's pore size in only slightly larger than the target molecule [52]. A parametric study on k_i is shown in Figure 3.6. However, to get these extremely dispersed breakthrough profiles, the particle radius must be ≈ 320 times larger than measured. This seems much too large to be reasonable. None of these profiles seems to describe the trends in Figure 3.4.

3.4.2 Heat Effects

Breakthrough profiles can be significantly changed due to how quickly or slowly the column transfers heat [53]. At first, the simulations used the same parameters for a similar activated carbon, TDA AMS 19 by TDA Research Inc. [50, 54]. The dynamic column breakthrough experiments performed on TDA 2015 were all fairly isothermal. Figure 3.7 shows the 10.56 bar of CO_2 breakthrough at 165°C under isothermal conditions; it looks very similar to the other simulations with heat effects in Figure 3.4, since the maximum temperature gain in the column is ≈ 15°C.

Convective heat transfer is modeled in the simulator using lumped heat transfer coefficients for the fluids inside and outside the column, h_{in} and h_{out} respectively. Changing the heat transfer coefficients can qualitatively change breakthrough profiles by spreading the breakthrough profile. An increase in the heat transfer coefficients causes the initial breakthrough ($C/C_0 \approx 0$) to occur earlier and the end of breakthrough ($C/C_0 \approx 1$) to occur later than an isothermal experiment at the same process conditions [53]. Under adiabatic conditions, there is no heat transfer outside of the system, $h_{out} = 0$. When a system is adiabatic, the temperature profile steps to a constant value with the concentration shock transition. After some time the temperature drops and the mole fraction increases with the drop. For the TDA 2015 system, this transition is difficult to see in Figure 3.7. As stated previously, this second shock transition appears due to the step temperature change in the column. The start and magnitude of the step can be significantly changed by changing the solid heat capacity, $C_{p,s}$. Figure 3.8 shows a parametric study on $C_{p,s}$ under adiabatic conditions. It seems that the qualitative breakthrough profiles could be fit by changing $C_{p,s}$, especially at very low values of $C_{p,s}$. This effect stems from the factor β in Equation 3.7, that is multiplied by $\frac{\partial T}{\partial t}$ in the column temperature energy balance, shown in Equation 3.6. A parametric study on β produced similar results to Figure 3.8. When a parametric study was run on $C_{p,a}$, less extreme effects were observed.

$$\left[\frac{1-\epsilon}{\epsilon}(\rho_s C_{p,s} + C_{p,a} \sum_{i=1}^{n_{comp}} q_i) \right] \frac{\partial T}{\partial t} = \frac{K_z}{\epsilon} \frac{\partial^2 T}{\partial z^2} - \frac{C_{p,g}}{R} \frac{\partial}{\partial z}(vP) - \frac{C_{p,g}}{R} \frac{\partial P}{\partial t}$$

$$- \frac{1-\epsilon}{\epsilon} C_{p,a} T \sum_{i=1}^{ncomp} \frac{\partial q_i}{\partial t} + \frac{1-\epsilon}{\epsilon} \sum_{i=1}^{ncomp} \left[(-\Delta H_i) \frac{\partial q_i}{\partial t} \right] - \frac{2h_{in}}{\epsilon r_{in}}(T - T_w) \quad (3.6)$$

$$\beta = \frac{1-\epsilon}{\epsilon}(\rho_s C_{p,s} + C_{p,a} \sum_{i=1}^{n_{comp}} q_i) \quad (3.7)$$

(a) Isothermal simulation   (b) Adiabatic simulation
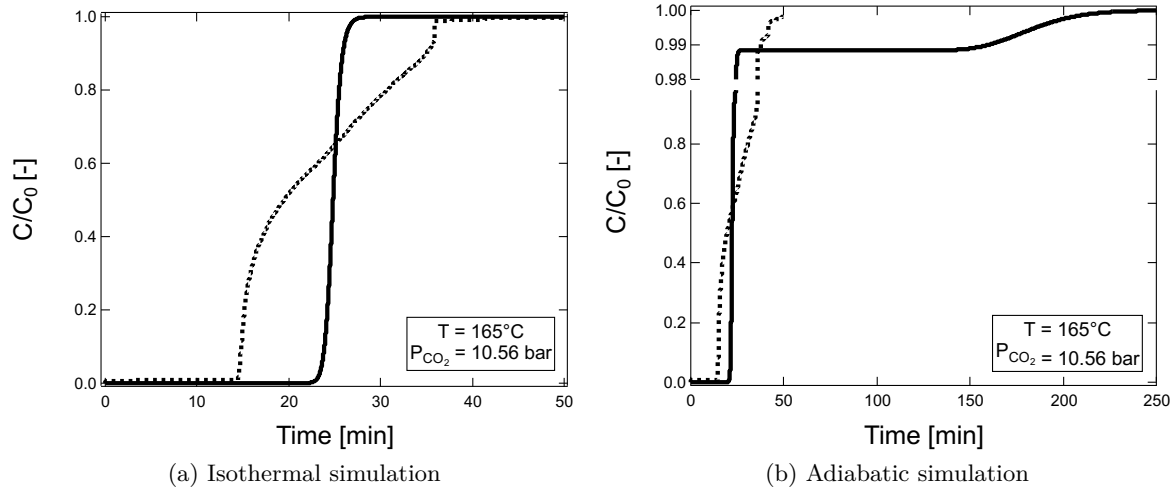
Figure 3.7: CO_2 concentration breakthrough on TDA 2015 at 165°C and 10.56 bar using the LRC isotherm under isothermal and adiabatic condidtions. Experiments are the dashed lines and simulations are the solid lines.

(a)   (b)
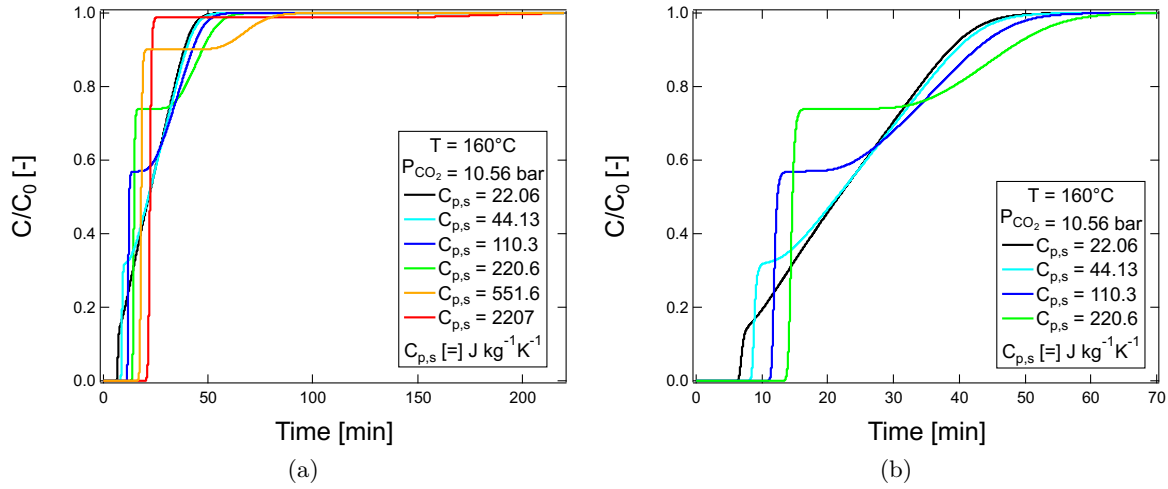
Figure 3.8: Simulated adiabatic CO_2 breakthrough profiles on TDA 2015 using the LRC isotherm with a variable solid heat capacity, $C_{p,s}$, at 160°C and 10.56 bar of CO_2. (a) contains a wide range of $C_{p,s}$ values, while (b) shows a zoomed view of low $C_{p,s}$ values.

Minimizing the loading error between the experiment at 165°C and 10.56 bar of CO_2 and the simulation by changing the parameters $C_{p,s}$, h_{in} and h_{out} yields a decent fit, Figure 3.9a. However, in Figure 3.9b the temperature gain associated with the change in $C_{p,s}$ is too massive. Also, the value of $C_{p,s}$ is too low to be physically possible.

Another interesting observation that seems to influence the concentration breakthrough shape are the temperature profiles. In Figure 3.4, above 8.6 bar CO_2, the temperature profiles deviate

from a shock to a simple wave decay. There seems to be two distinct temperature regions; initially the temperature rises quickly, then it continues to rise but at a slower rate. The simple wave decay occurs after the maximum temperature is reached. The is behavior is similar to some articles in the literature [55]. The more the temperature profile "bends" the more dispersed the concentration breakthrough becomes. However, no model that was implemented captured the temperature dynamics properly.

(a) Concentration breakthrough

(b) Thermal breakthrough
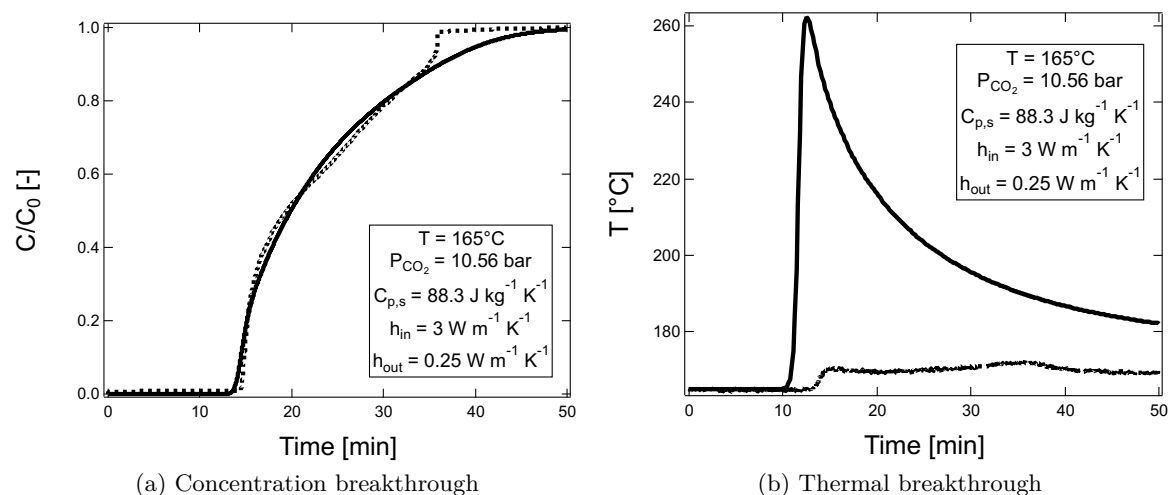
Figure 3.9: CO_2 concentration and thermal breakthrough profiles on TDA 2015 using the LRC isotherm with a variable solid heat capacity, $C_{p,s}$ at 165°C and 10.56 bar of CO_2. Experimental results are the dashed lines and the simulations are the solid lines.

3.4.3 Equilibrium Effects

Equilibrium effects refer to changes in concentration or thermal breakthrough shape due to adsorptive equilibrium. This is normally seen in isotherms other than type 1. A few case studies were performed to see how a change in isotherm could effect the breakthrough profiles. Detailed studies exist in the literature [56].

For type 1 equilibrium data, concentration and thermal breakthrough profiles look very similar to what is observed in Figure 3.4 at the lowest pressure (≈ 2.45 bar) at every feed temperature. This shock transition is due to a favorable isotherm with fast kinetic behavior. However, if an isotherm includes favorable and unfavorable sections, a mixture of shock transitions and waves will be observed [56]. As seen in Figure 3.4, the experimental breakthrough profiles at ≈ 10.57 bar seem as if the concentration profiles are a shock followed by a short simple wave. These dynamics could be seen from a BET (type 2) isotherm. A BET isotherm describes adsorption near pore condensation, when loading goes to infinity at the liquid-gas phase transition [36]. A series of breakthrough simulations were run using the isotherm fit shown in Figure 3.2. One of these simulations is shown in Figure 3.10.

42
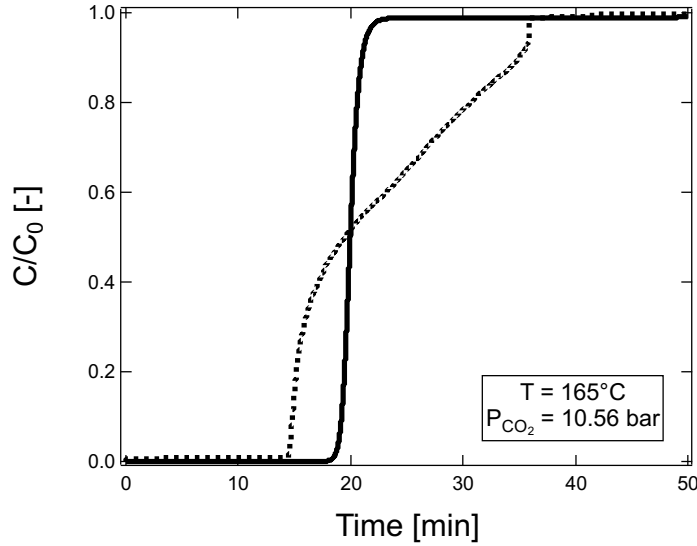
Figure 3.10: CO_2 concentration breakthrough on TDA 2015 at 165°C and 10.56 bar using the BET isotherm. Experimental results are the dashed lines and the simulations are the solid lines.

The BET isotherm shows a shock and a wave combined profile, but only at pressures close to the saturation pressure. For this fit, $p_s = 69.9$ bar. The experimental partial pressure, which is 10.56 bar, is not very close to the p_s; under these conditions the simple wave would not be seen. The elongated breakthrough behavior is better seen near the BET isotherm transition from concave down to concave up; in other words, when the gas begins to form multiple layers in the binding sites. If the concentration is two times larger, a slight deformation at the top of the simulated curve is seen in Figure 3.11, but the shape is still not the same as the experiment.
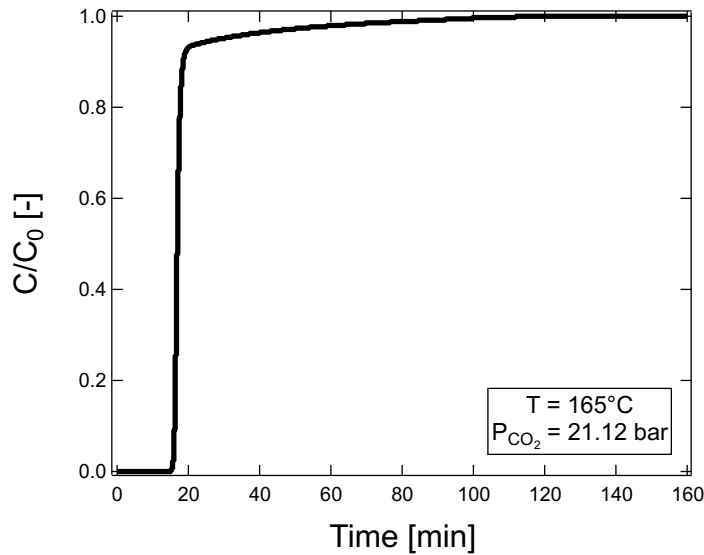
Figure 3.11: Simulated CO_2 concentration breakthrough on TDA 2015 at 165°C and 21.12 bar using the BET isotherm.

43

The breakthrough profile in Figure 3.11 was twice as concentrated as in Figure 3.10. From these simulations it does not seem likely that the BET isotherm will match the experimentally observed breakthrough profiles.

The quadratic-Langmuir isotherm was also tried. It does not fit the experimental data for TDA 2015 well, but it was tested to determine if the shape was possible. This isotherm has a type 4 shape, therefore it is possible to get a mixed shock and wave breakthrough profile. The results are in Figure 3.12. It seems that the simulated profile does look better qualitatively, but still does not fit the experiment well. If the quadratic-Langmuir isotherm parameters are changed slightly to those in Table 3.5, the qualitative breakthrough from the simulation in Figure 3.13b looks much better. However, the isotherm fit, shown in Figure 3.13a, is much worse. If the same hypothetical isotherm in Figure 3.13a is simulated and compared against the 2.44 bar experiment at 164°C, a large error in loading is seen in Figure 3.14.

Table 3.5: Hypothetical quadratic-Langmuir isotherm parameters for pure CO_2.

	q_1^{sat} [mol/kg]	b_1 [m^3/mol]	b_2 [m^6/mol^2]	q_2^{sat} [mol/kg]	b_3 [m^3/mol]
CO_2	1.00	-3.85×10^{-3}	1.50×10^{-5}	1.00	1.49×10^{-2}
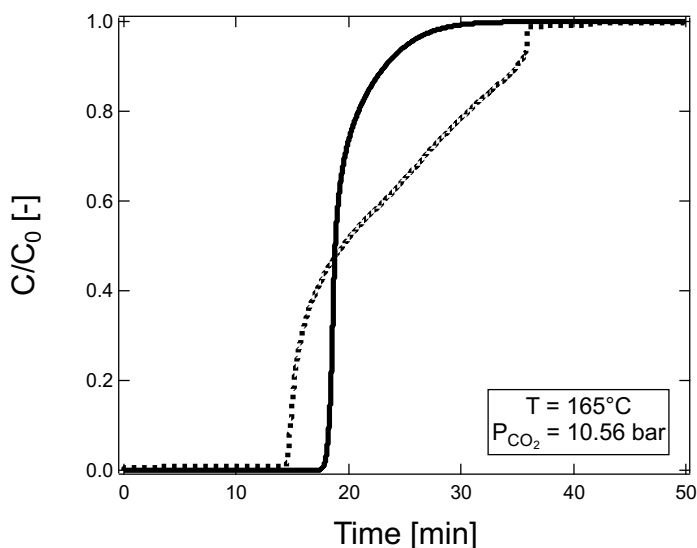
Figure 3.12: CO_2 concentration breakthrough on TDA 2015 at 165°C and 10.56 bar using the quadratic-Langmuir isotherm. Experimental results are the dashed lines and the simulations are the solid lines.

Another factor that makes the equilibrium effects argument weaker is that the desorption profiles look like type 1 desorption profiles, shown in Figure 3.5. From equilibrium theory, a type 1 isotherm will produce a shock transition for adsorption and a simple wave decay for desorption [57]. If equilibrium theory is extended to a type 4 isotherm, a mixture shock transition and

simple wave is seen in both the adsorption and desorption profiles [58]. Both a shock and simple wave will be seen only if the concentration is greater than the concave down portion of the isotherm. Therefore, if equilibrium effects were occurring, it is likely that the very dispersed breakthrough profiles would also have mixture shock and simple wave desorption profile.
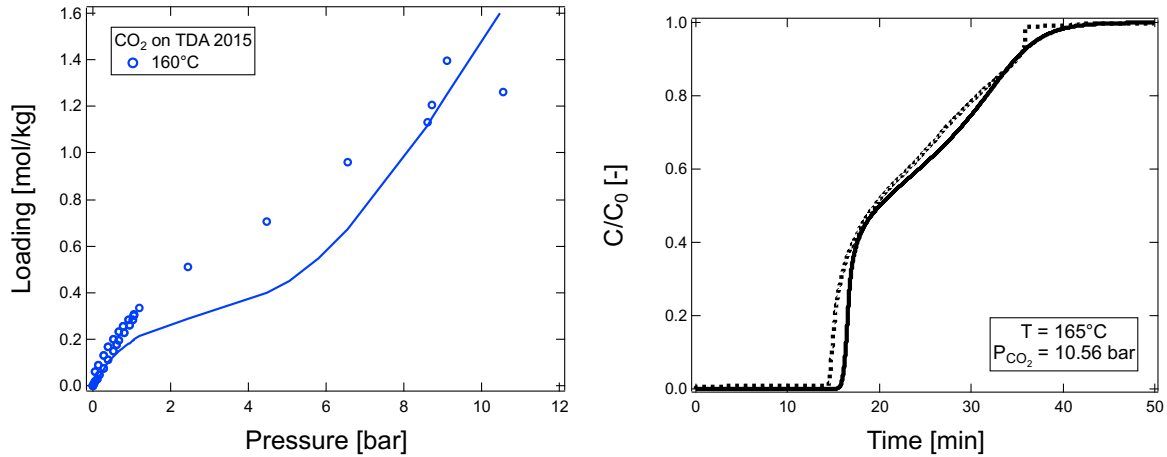
(a) The hypothetical quadratic-Langmuir isotherm

(b) The experimental and simulated breakthrough

Figure 3.13: The hypothetical quadratic-Langmuir isotherm (a) and the experimental and simulated breakthrough of TDA 2015 at 165°C and 10.56 bar of CO_2 (b). In (b), experimental results are the dashed lines and the simulations are the solid lines.
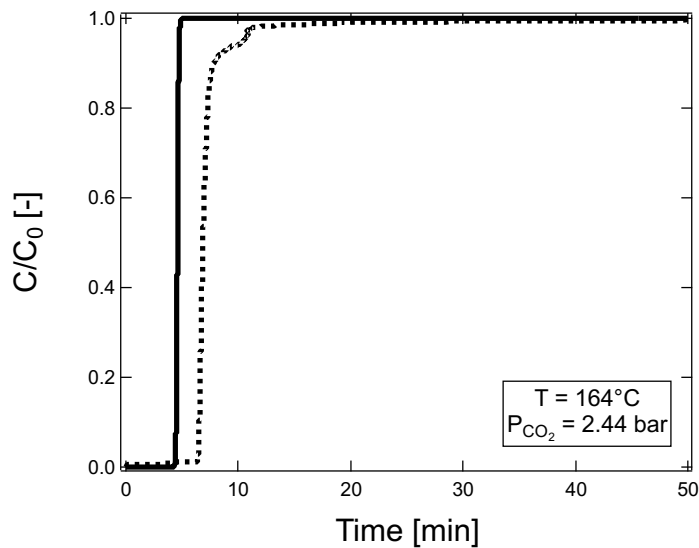
Figure 3.14: CO_2 concentration breakthrough on TDA 2015 at 164°C and 2.44 bar using the quadratic-Langmuir isotherm. Experimental results are the dashed lines and the simulations are the solid lines.

3.4.4 Possible Explanations for Dispersion in the TDA 2015 Breakthrough Profiles

It's difficult to say which effect is dominating. From the temperature profiles in Figure 3.4, it seems apparent that the temperature breakthroughs are either a cause or an effect of the concentration breakthrough. However, most parameters didn't seem to change the temperature profiles too greatly. The heat capacity of the adsorbent, $C_{p,s}$, did seem to change the qualitative concentration breakthrough shape in Figure 3.9a, but the resulting temperature profile was very wrong, as seen in Figure 3.9b. No parametric study or change tried was able to model the "plateau" shape of the temperature profiles at CO_2 partial pressures ≥ 8.5 bar. The temperature profiles in Figure 3.4 even started bending at ≈ 6.5 bar in the 165°C and 204°C experiments. Something peculiar about the data is the relatively small temperature change over the process; this fact makes it hard to believe that temperature is the sole driving force for the large dispersion.

The collected equilibrium data looks like it's a type 1 isotherm. From Figure 3.2, the best isotherm fits are also for type 1 isotherms. The case study in Figure 3.13 showed it is possible to get the qualitative breakthrough shape with a type 4 isotherm, but the corresponding quadratic-Langmuir isotherm does not work for other concentrations, as seen in Figure 3.14. A paper by Park et. al. claims that, if this dispersion is due to the isotherm shape, the isotherm can't be type 1 [56]. The study presented in Park et. al. was able to model breakthrough dispersion like observed in Figure 3.4, but the desorption profiles also had a mixture shock and simple wave trend [56]. The observed desorption profiles in Figure 3.4, do not show anything other than a simple wave decay.

While the experiments have been successfully modeled at lower CO_2 concentrations, it would be a good idea to try to observe these breakthrough profiles on another apparatus and also to test it in a high pressure gravimetery unit. This would eliminate any doubt on the measured dynamic column breakthrough loadings. It is also possible that the TDA 2015 sample has been irreversibly damaged. If the TDA 2015 sample had been damaged, the observed dynamics would not be actual dynamics of the adsorbent. A fresh sample of TDA 2015 should be used in future experiments. There is also a possibility that CO_2 has condensed within the pores of TDA 2015; this could be studied with a gravimeter at high pressures of CO_2.

3.5 Conclusions

In this study the use of TDA 2015 as a pre-combustion carbon capture adsorbent was explored. CO_2 equilibrium was characterized using volumetry and dynamic column breakthrough. The equilibrium data was fit to various isotherms; the LRC isotherm provided the best fit. H_2 equilibrium was not characterized, but is known to be very weakly adsorbing on TDA 2015. Dynamic

column breakthrough experiments also provided the concentration and temperature dynamics of the adsorbent bed. These experiments were modeled using mass and energy balances and simulated in our in-house adsorption simulator. The simulator was able to predict the experiments at $\approx$ 2.5 and 4.5 bar of CO_2 well. However, at higher concentrations, especially 8.5 bar of CO_2 and above, the simulator was unable to qualitatively describe the experimental breakthroughs. The breakthrough experiments above 8.5 bar of CO_2 all had extremely dispersed concentration fronts. The corresponding temperature profiles seemed flattened, when compared to the results below 6.5 bar of CO_2. All simulations were able to quantitatively match the experimental loadings well. Desorption experiments were also performed; all these experiments show that desorption was a simple wave, regardless of inlet CO_2 concentration. Many explanations for the qualitative breakthrough trends were presented for mass transfer, heat and equilibrium effects. From a parametric study on k_i, it seemed unlikely that mass transfer effects could explain the dispersion. Equilibrium effects were shown to qualitatively predict the observed experimental breakthroughs. However, the qualitative fit was with a type 4 quadratic-Langmuir isotherm that does not fit the equilibrium data or other concentrations well. Also, the desorption profiles are all simple waves, further disproving the idea. Heat effects are the most likely cause; but there might be other effects that were unexplored during this study. At this time, the proposed LRC isotherm for CO_2 works qualitatively best at concentrations at or under 6.5 bar of CO_2. The LRC isotherm quantitatively works for all experiments.

Future work should prove whether or not the observed breakthrough profiles are system-specific. At this time only one dynamic column breakthrough apparatus has tested TDA 2015. It would also be useful to measure pure CO_2 in a high pressure gravimeter. This would confirm whether the observed dynamic column breakthrough loadings were correct. A fresh sample of TDA 2015 should be used in future experiments to ensure that sample hasn't been irreversibly damaged. Once the model is more finely tuned, purity and recovery optimizations should be performed to determine the best cycles and conditions for this pre-combustion capture capture process.

Chapter 4

Characterization of Zeolite 13X for Humid Post-Combustion Carbon Capture

4.1 Introduction

In a traditional power plant, fuel and air are fed to a reactor and combusted. The reaction products are primarily H_2O and CO_2. N_2 from the air remains mostly unreacted. There are also small amounts of NO_x and SO_x. Often, more H_2O is added to remove the SO_x, saturating the product gas stream. The effluent waste gas would be H_2O, CO_2, and N_2, but, in many papers H_2O is neglected [9, 15, 19]. This is due to the extremely strong affinity of H_2O on some post-combustion adsorbents, such as zeolite 13X [13, 59]. Zeolite 13X is the benchmark adsorbent for post-combustion carbon capture; this is partially due its large selectivity of CO_2 over N_2, but also because it is extremely cheap. Adsorption cycling using zeolite 13X under dry conditions can produce a CO_2 purity $> 95\%$ with a recovery $> 90\%$ [19].

Under wet conditions much less is known. If ideal competition is assumed, Krishnamurthy et. al. states that a post-combustion process with wet flue gas can achieve CO_2 purites $> 95\%$ and recoveries $> 90\%$, but at the expense of more energy and a lower productivity than a dry process [18]. A lower productivity and higher energy is associated with H_2O cycling because H_2O "kills" part of the bed that no longer participates in CO_2 capture [59].

One of the main challenges of humid post-combustion carbon capture using zeolite 13X is quantifying the competition between CO_2 and H_2O. Competitive adsorption of CO_2 and H_2O on zeolite 13X does not follow ideal adsorbed solution theory because the mixture is extremely nonideal [60]. At low H_2O concentrations, ideal adsorbed solution theory over predicts CO_2 adsorption and at higher H_2O concentrations there is an under prediction of CO_2 loading. Wang and LeVan collected CO_2/H_2O competitive equilibrium data and fit the data to a Virial excess mixing coefficient model (VEMC), their results at 25°C are in Figure 4.1 [60]. Even measuring

pure H_2O equilibrium data is difficult, since at post-combustion conditions the concentration of H_2O is very small and at low temperatures. Also it is difficult to prevent condensation within the experimental apparatuses. For humid post-combustion carbon capture, the column feed is around 25°C and 1 bar total pressure with $y_{CO_2} = 0.15$, $y_{N_2} = 0.83$ and $y_{H_2O} = 0.02$.
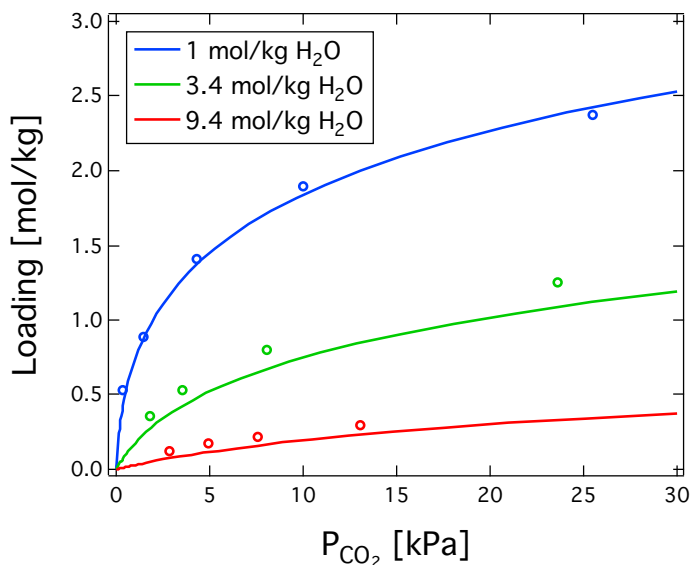
Figure 4.1: Competitive CO_2/H_2O isotherm for CO_2 on standard zeolite 13X (Grace Davison) at 25°C [60]. Experimental data are the circles and the solid lines are a VEMC fit, both found by Wang and LeVan [60].

4.2 Adsorption Equilibrium on Zeolite 13X

Two zeolite 13X samples were obtained from Zeochem (Uetikon am See, Switzerland); one is a standard zeolite 13X (Z10-02) and the other is a premium zeolite 13X (Z10-02ND). Not much is known about the premium zeolite 13X, except that it has a higher CO_2 capacity than the standard zeolite 13X.

4.2.1 Standard Zeolite 13X (Z10-02)

CO_2 and N_2 adsorption on the standard zeolite 13X has been characterized and modeled in many previous papers [9, 17, 18]. The standard zeolite 13X (Z10-02) appears to behave very similarly to other zeolite 13X adsorbents prepared by other companies [16]. Since the standard zeolite 13X has been well studied, only a few experiments were performed to determine equilibrium behavior. Pure component equilibrium for CO_2 and N_2 were determined between 25°C and 100°C to 1.2 bar using a Micromeritics ASAP 2020 volumetry apparatus (Norcross, GA, USA). All samples were activated at 350°C under vacuum for 12 hours before isotherm measurement. These results are shown in Figure 4.2. CO_2 and N_2 equilibrium data are consistent with what has been reported in the literature for the same standard zeolite 13X (Zeochem Z10-02) [17].

The CO_2 equilibrium data is $\approx 11\%$ stronger on the standard (Z10-02) zeolite 13X from Zeochem than the Grace Davison zeolite 13X that was reported in Wang and LeVan [16].

(a) CO_2

(b) N_2
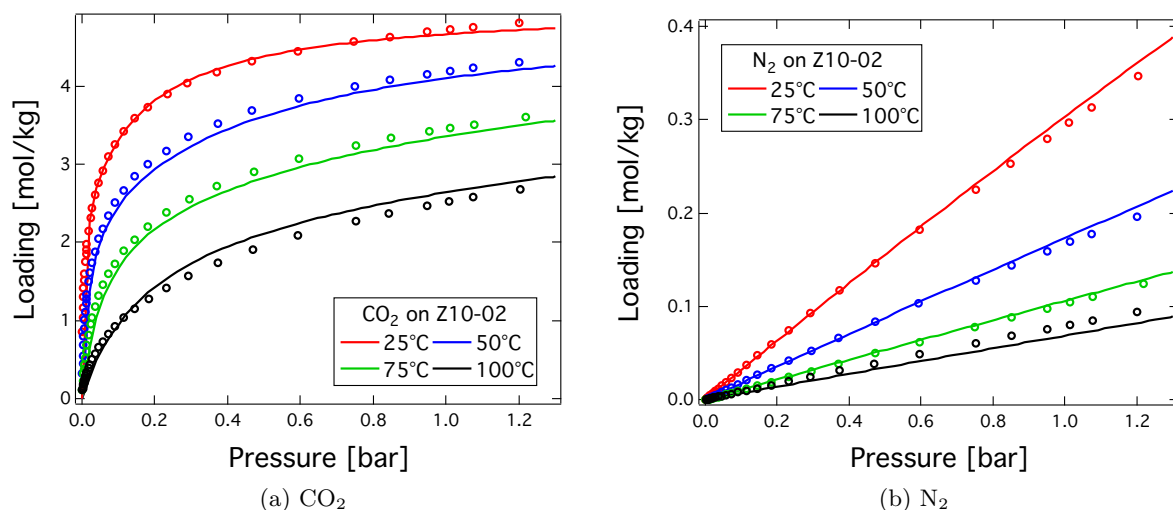
Figure 4.2: Pure adsorption equilibrium on the standard zeolite 13X (Z10-02) collected via volumetry. Volumetric data are circles and the dual-site Langmuir fits are lines.

Table 4.1: Dual-site Langmuir isotherm parameters for pure components on standard (Z10-02) and premium (Z10-02ND) zeolite 13X.

Material	Gas	q_{sb} [mol/kg]	b_0 [m^3/mol]	ΔU_b [kJ/mol]	q_{sd} [mol/kg]	d_0 [m^3/mol]	ΔU_d [kJ/mol]
Z10-02	CO_2	2.366	1.76×10^{-7}	-42.97	2.672	1.21×10^{-7}	-34.91
Z10-02	N_2	6.173	1.96×10^{-6}	-16.07	0	0	0
Z10-02	H_2O	10.190	2.35×10^{-7}	-55.72	6.263	7.99×10^{-8}	-45.48
Z10-02ND	CO_2	3.257	2.09×10^{-7}	-42.67	3.240	1.06×10^{-7}	-32.21
Z10-02ND	N_2	5.030	2.50×10^{-6}	-15.10	0	0	0
Z10-02ND	H_2O	11.209	2.35×10^{-7}	-55.72	6.890	7.99×10^{-8}	-45.48

The equilibrium data was fit to a dual-site Langmuir isotherm, where b_i and d_i are functions of temperature. The parameters are in Table 4.1.

$$q_i^* = \frac{q_{i,b}^{sat} b_i C_i}{1 + \sum_{i=1}^{n_{comp}} b_i C_i} + \frac{q_{i,d}^{sat} d_i C_i}{1 + \sum_{i=1}^{n_{comp}} d_i C_i} \tag{4.1}$$

$$b_i = b_{i,0} exp\left(\frac{-\Delta U_b}{RT}\right) \tag{4.2}$$

$$d_i = d_{i,0} exp\left(\frac{-\Delta U_d}{RT}\right) \tag{4.3}$$

Pure water vapor isotherms were collected via volumetry by Wang and LeVan on a similar standard zeolite 13X (Grace Davison) [16]. The data was fit to a dual-site Langmuir isotherm

by Krishnamurthy et al [18]. However, as stated earlier the CO_2 data was 11% stronger for the Zeochem standard zeolite 13X than the reported Grace Davison zeolite 13X. Therefore, the H_2O saturation loading was assumed to be 11% larger for both sites. The isotherm fit is shown in Figure 4.3.
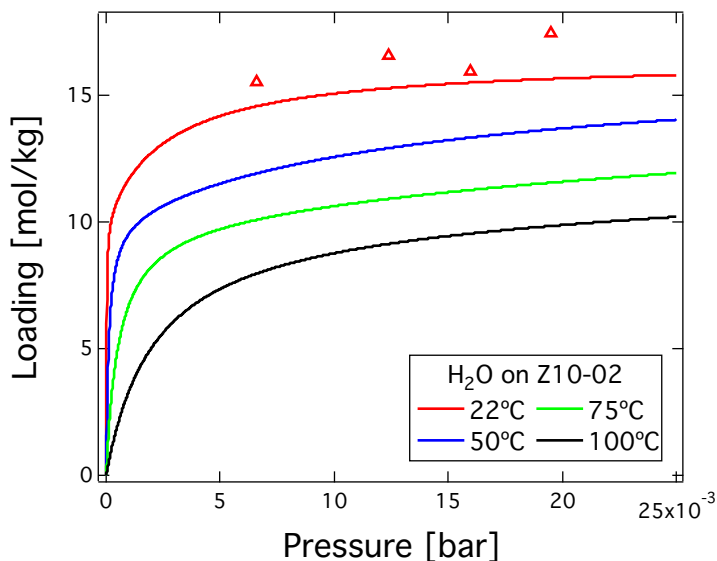
Figure 4.3: Pure H_2O adsorption equilibrium on the standard zeolite 13X (Z10-02) at 22, 50, 75 and 100°C. Experimental equilibrium points were collected via dynamic column breakthrough.

4.2.2 Premium Zeolite 13X (Z10-02ND)

The premium zeolite 13X, to our knowledge, has not been studied. It appears to have a less invasive binder that promotes adsorption. Since this material has not been previously characterized a more extensive CO_2 and N_2 experimental campaign was performed. Some volumetric experiments were performed using the Micromeritics ASAP 2020 (Norcross, GA, USA) for temperatures between 0°C and 100°C to 1.2 bar. To measure equilibrium at higher temperatures and pressures a Rubotherm Magnetic Suspension Balance Type E10 was used (Bochum, Germany). Again, these samples were activated at 350°C for 12 hours under vacuum. These results are shown in Figure 4.4. Dual-site Langmuir isotherm parameters are shown in Table 4.1.

After the pure H_2O dynamic column breakthrough experiments were completed, saturation loadings at ≈ 22°C were found. The H_2O isotherm found by Krishnamurthy et. al. was modified to model the measured premium zeolite 13X loadings. This was done by multiplying the saturation loading of both sites by a factor to fit the measured equilibrium points. The fit can be seen in Figure 4.5.
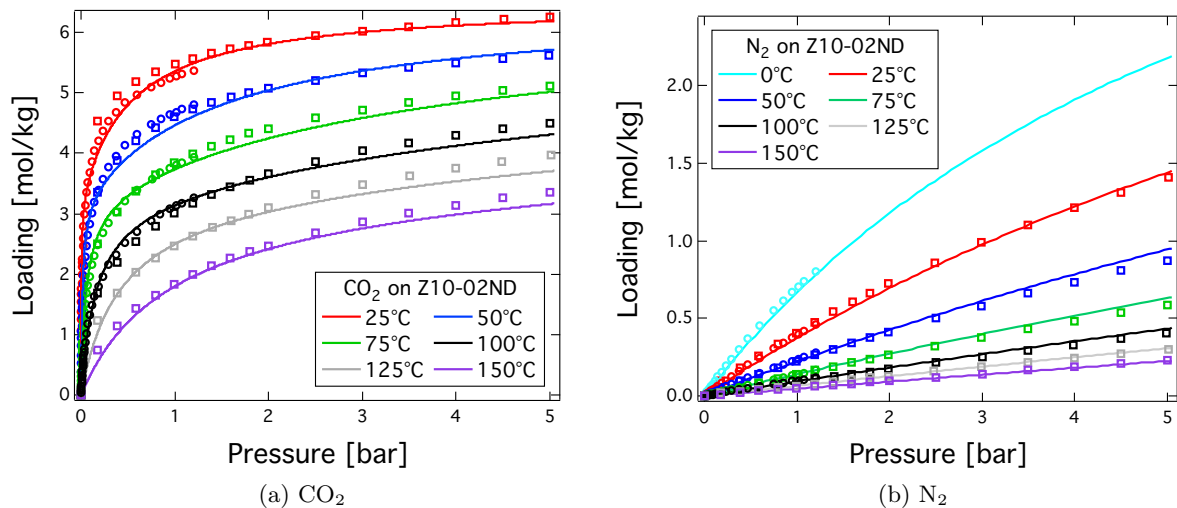
Figure 4.4: Pure adsorption equilibrium on the premium zeolite 13X (Z10-02ND). Volumetric data are circles, gravimetric data are squares and the dual-site Langmuir fits are lines.
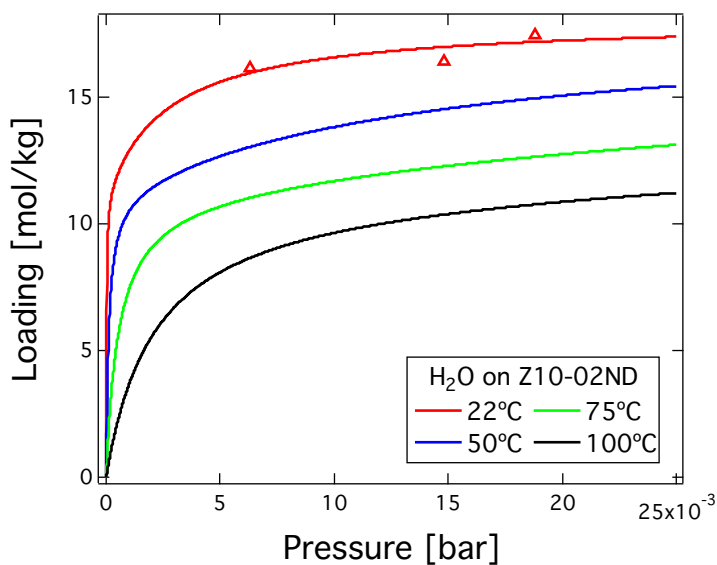
Figure 4.5: Pure H_2O adsorption equilibrium on the premium zeolite 13X (Z10-02ND) at 22, 50, 75 and 100°C. Experimental equilibrium points were collected via dynamic column breakthrough.

4.2.3 Comparison of the Standard and Premium Zeolite 13X Materials

A comparison of the standard and premium isotherms at 25°C is shown in Figure 4.6. As shown, the premium zeolite 13X has a greater capacity for CO_2. It also, unfortunately, has a greater capacity for N_2; this could lead to a worse separation between CO_2 and N_2 in the premium zeolite 13X [19].
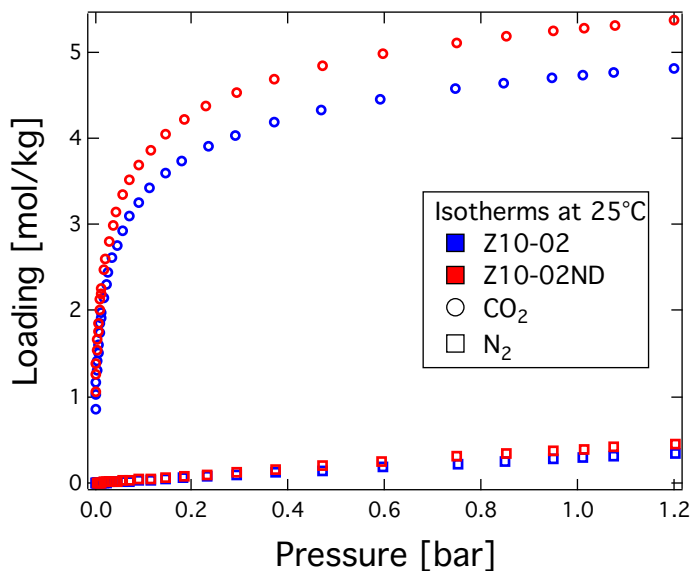
Figure 4.6: Comparison of the standard (Z10-02) and premium (Z10-02ND) zeolite 13X samples at 25°C.

N_2 volumetric isotherms at -196°C were measured to determine the surface area and internal volumes of both materials; these values are shown in Table 4.2. As seen in Table 4.2, both zeolites have very similar Langmuir and BET surface areas and internal volumes. This suggests that the binder ratio for both materials are very similar. In Figure 4.7, the pore volume is shown as a function of pore width. From Figure 4.7, it is apparent that the two samples only differ at the mesopores, which would have no effect on the material's adsorption strength.
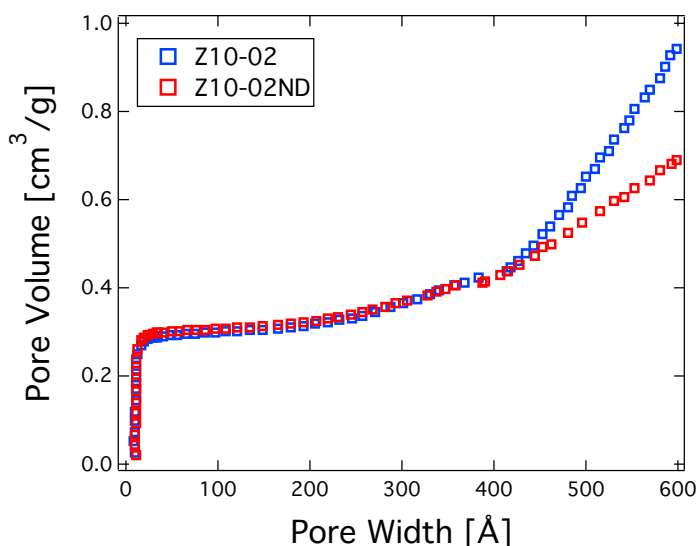
Figure 4.7: Comparison of the standard (Z10-02) and premium (Z10-02ND) zeolite 13X pore volumes. These values were measured via volumetric liquid N_2 isotherms at -196°C.

A liquid N_2 isotherm will not give any meaningful information of the micropore's size. It is

possible that the micropore sizes are slightly different for both materials; but a liquid argon measurement would need to be made for a definitive conclusion. It is possible that the premium zeolite 13X contains an active binder that has an affinity to polar molecules.

Table 4.2: Surface area and internal volume measurements on standard (Z10-02) and premium (Z10-02ND) zeolite 13X. These values were measured via volumetric liquid N_2 isotherms at -196°C.

Material	$S_{A,Lang}$ [m^2/g]	$S_{A,BET}$ [m^2/g]	$V_{internal}$ [m^3/g]
Z10-02	829 ± 2	564 ± 20	2.921×10^{-7}
Z10-02ND	859 ± 2	575 ± 21	2.995×10^{-7}

4.2.4 Isosteric Heat of Adsorption

The isosteric heat of adsorption, shown in Figure 4.8, was determined via the volumetry equilibrium data.

(a) CO$_2$ (b) N$_2$
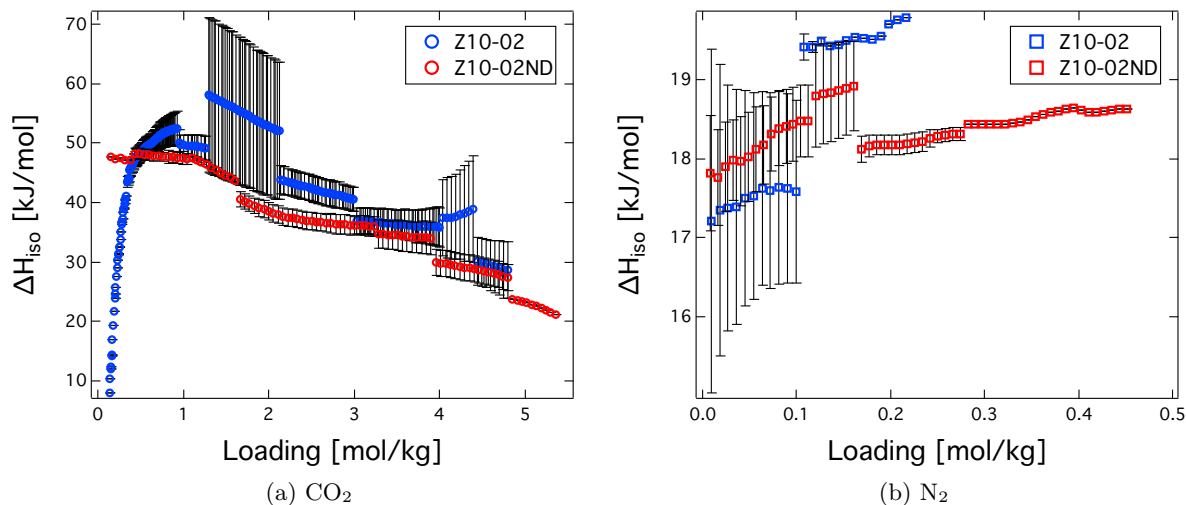
Figure 4.8: The isosteric heat, ΔH_{iso}, on standard (Z10-02) and premium (Z10-02ND) zeolite 13X.

Figure 4.8 was found using the Clausius-Clapeyron equation, shown in Equation 4.4.

$$\left[\frac{\partial ln(p_i)}{\partial (1/T)} \right]_{q_i} = -\frac{\Delta H_{iso}}{R} \tag{4.4}$$

The isosteric heat of adsorption on both the standard and premium zeolite 13X adsorbents are almost identical. This suggests that there is no difference between the binding sites of both adsorbents, since ΔH_{iso} is a measure of the energy released during adsorption at a specific loading [41]. The calculated data is in agreement with values in the literature [61].

4.3 Dynamic Column Breakthrough

Pure CO_2 breakthrough experiments are performed using the apparatus shown in Figure 2.5. For the H_2O breakthrough experiments, the setup is slightly different than the general breakthrough apparatus. The H_2O DCB schematic is shown in Figure 4.9.
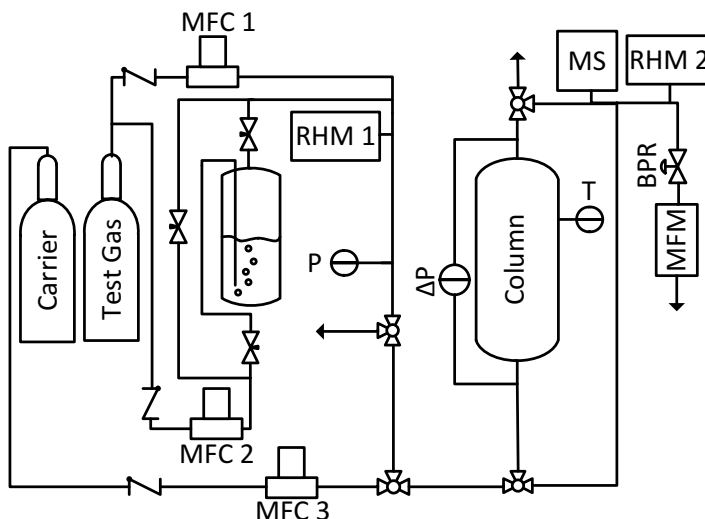
Figure 4.9: The dynamic column breakthrough apparatus with the bubbler humidifier. In this schematic: BPR = back-pressure regulator, MFC = mass flow controller, MFM = mass flow meter, MS = mass spectrometer, P = pressure transducer, ΔP = differential pressure transducer, RHM = relative humidity meter and T = thermocouple.

All experiments were performed in a 40 mL column. Before each breakthrough experiment, the column was swept with instrument air or He for H_2O and CO_2, respectively. To generate humid carrier gas, a bubbler humidifier is utilized. A bubbler humidifies a gas stream by flowing a carrier stream through deionized water. The exiting stream, depending on the design of the bubbler, is at or just below saturation. The humidified stream then mixes with a dry carrier stream. Fixing the flowrates of MFC 1 and MFC 2 gives a constant relative humidity. The wet and dry streams do not become well mixed instantaneously, therefore a purge was included to allow mixing dynamics to become steady before the combined stream is injected into the column.

4.3.1 Pure Component Breakthrough Measurements

Pure H_2O and CO_2 breakthrough experiments were performed at 1.02 bar and 22°C. Table 4.3 has a summary of the breakthrough experiments. They were then simulated with our in-house adsorption simulator for both zeolite 13X adsorbents. Parameters for the experiments and simulations are in Table 4.4. Two 40 mL cylinders (304L-HDF2-40) were obtained by Swagelok (Edmonton, AB, Canada). The column length, inner and outer diameters were given by the manufacturer. The outer diameter and length were checked with a caliper and ruler respectively.

The bulk density, ρ_{bulk}, was measured by weighing a volume of adsorbent from a graduated cylinder after the particles had been well packed. The bulk void fraction, ϵ, was assumed using a common value [62]. The particle void fraction, ϵ_p, the specific heat capacity of the adsorbent, $C_{p,s}$, and tortuosity, τ, were assumed to be the same as in Haghpanah et. al., which used the same standard zeolite 13X [9]. The specific heat capacity of the column wall, $C_{p,w}$, the thermal conductivity of the wall, K_w, and the column density, ρ_w, were all taken as standard values for stainless steel. The specific heat capacity of the gas, $C_{p,g}$ and the fluid viscosity, μ, were taken as standard values for a CO_2/He, H_2O/Air or CO_2/H_2O mixture. The specific heat capacity of the adsorbent, $C_{p,a}$, was assumed to be the same as $C_{p,g}$ since no information was known about $C_{p,a}$. The molecular diffusion, D_m, for all mixtures was found using the Chapman-Enskog equation [43]. The internal and external heat transfer coefficients, h_{in} and h_{out}, and the effective gas thermal conductivity, K_z, were determined via an optimization to match the thermal breakthrough profiles.

Table 4.3: A summary of the experimental single component breakthrough experiments on premium (Z10-02ND) and standard (Z10-02) zeolite 13X. Single component experiments include either helium or instrument air as a carrier for CO_2 and H_2O respectively. The error is the percent difference between the experiment and simulation for a particular single component experiment.

Material	Gas	T [°C]	RH [%]	P_{H_2O} [bar]	P_{CO_2} [bar]	$q^*_{H_2O}$ [mol/kg]	$q^*_{CO_2}$ [mol/kg]	Error [%]
Z10-02	H_2O	22.7	25.0	6.62×10^{-3}	-	15.56	-	5.08
Z10-02	H_2O	23.2	44.4	1.24×10^{-2}	-	16.58	-	5.97
Z10-02	H_2O	23.2	56.3	1.60×10^{-2}	-	15.96	-	0.55
Z10-02	H_2O	22.3	73.9	1.95×10^{-2}	-	17.50	-	8.17
Z10-02ND	H_2O	23.1	23.8	6.33×10^{-3}	-	16.18	-	0.62
Z10-02ND	H_2O	22.6	55.1	1.48×10^{-2}	-	16.46	-	4.74
Z10-02ND	H_2O	22.4	70.5	1.88×10^{-2}	-	17.49	-	0.11
Z10-02ND	CO_2	21.9	-	-	4.864×10^{-1}	-	4.685	3.65
Z10-02ND	CO_2	21.8	-	-	1.523×10^{-1}	-	3.854	4.39

For pure water vapor breakthrough experiments, dry instrument air was used as a carrier. For CO_2 breakthrough experiments, helium was used as a carrier gas. The experimental time, t, was non-dimensionalized, $\bar{t}$, by a factor of the residence time, $\frac{L}{v}$, in the column, where L is bed length and v is the feed velocity.

$$\bar{t} = \frac{tv}{L} \tag{4.5}$$

All CO_2 breakthrough experiments are shown in Figure 4.11. Single component CO_2 experiments were only performed on the premium zeolite 13X. All experiments were repeatable. Loadings on the premium zeolite 13X agree with the isotherm experiments. The CO_2 breakthrough experiments were at two different flowrates. The 15% CO_2 experiments were done at 700 ccm while the 50% CO_2 experiments were at 350 ccm. This was due to limitations of the flow controllers utilized in the breakthrough apparatus. Due to this, a single internal heat transfer

coefficient, h_{in}, could not be used to model the temperature breakthrough profiles for both experiments; h_{in} is a function of the flowrate in the column. The value of h_{in} reported in Table 4.4 fits the 50% CO_2 experiment at 350 ccm, but not the 15% CO_2 experiment; however, if h_{in} is changed to 1 W m^{-2} K^{-1}, the 15% CO_2 thermal breakthrough at 700 ccm can be fitted.

Table 4.4: Simulation parameters for the standard and premium zeolite 13X post-combustion processes.

Parameter	Value	Source
Column Properties		
adsorbent mass, m [g]	22.03	measured
column length, L [m]	6.4×10^{-2}	measured
inner column diameter, d_i [m]	2.82×10^{-2}	measured
outer column diameter, d_o [m]	3.18×10^{-2}	measured
column void fraction, ϵ	0.4	measured
particle void fraction, ϵ_p	0.35	measured
tortuosity, τ	3	assumed
Properties and Constants		
universal gas constant, R [m^3 Pa mol^{-1} K^{-1}]	8.314	standard value
adsorbent particle density, ρ_p [kg m^{-3}]	961.7	measured
column wall density, ρ_w [kg m^{-3}]	7800	standard value
specific heat capacity, $C_{p,g}$ [J mol^{-1} K^{-1}]	1404.0 (CO_2) 1028.2 (H_2O)	standard value
specific heat capacity of adsorbed phase, $C_{p,a}$ [J mol^{-1} K^{-1}]	1404.0 (CO_2) 1028.2 (H_2O)	assumed
specific heat capacity of adsorbent, $C_{p,s}$ [J mol^{-1} K^{-1}]	1070	assumed
specific heat capacity of column wall, $C_{p,w}$ [J mol^{-1} K^{-1}]	502.0	standard value
fluid viscosity, μ [kg m^{-1} s^{-1}]	1.812×10^{-5}	standard value
molecular diffusion, D_m [m s^{-2}]	1.6×10^{-5} (CO_2) 5.0×10^{-6} (H_2O)	standard value
effective gas thermal conductivity, K_z [W m^{-1} K^{-1}]	4.0×10^{-1}	assumed
thermal conductivity of column wall, K_w [W m^{-1} K^{-1}]	16.0	standard value
internal heat transfer coefficient, h_{in} [W m^{-2} K^{-1}]	4.0 (CO_2) 12.0 (H_2O)	assumed
external heat transfer coefficient, h_{out} [W m^{-2} K^{-1}]	10.0	assumed

All pure H_2O breakthroughs were done at 1.2-1.3 SLPM total flow. Figures 4.10 and 4.11 shows H_2O concentration and temperature breakthroughs at $\approx$ 25, 45, 55 and 70% relative humidity. All experiments were repeatable. All H_2O breakthroughs are shock transitions, suggesting type 1 isotherm behavior, as observed in the literature [59,63]. A comparison of the H_2O concentration breakthrough experiments, Figures 4.10 and 4.11, shows that premium zeolite 13X adsorbs more H_2O than the standard zeolite 13X. Both 40 mL columns were loaded with $\approx$ 23 g of premium or standard zeolite 13X. Also, the ρ_{bulk} of both materials was essentially the same and so it is acceptable to directly compare the breakthroughs on these materials.
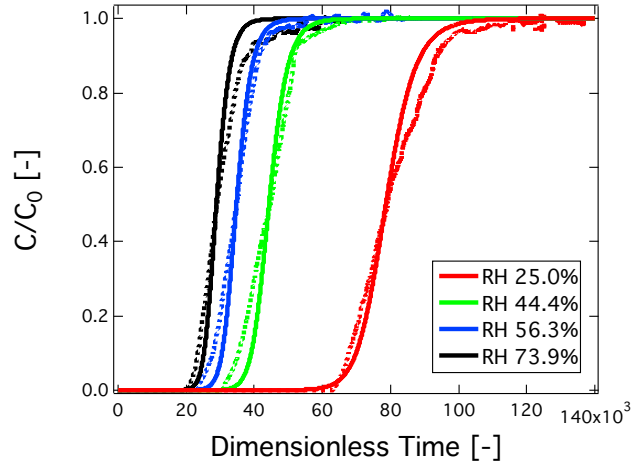
(a) H₂O concentration breakthrough
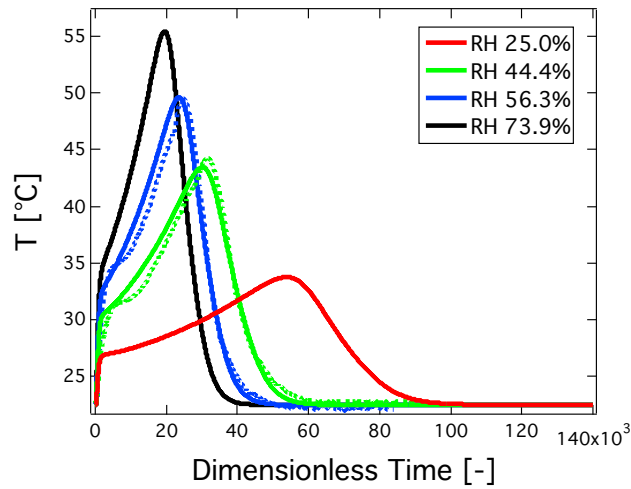
(b) H₂O thermal breakthrough

Figure 4.10: Single component H$_2$O concentration and temperature breakthrough profiles on standard zeolite 13X (Z10-02) at $\approx 22°$C and 25, 45, 55 and 70% relative humidity. Experiments are the dotted lines and simulations are the solid lines. Temperature is measured at $z = 0.8L$. The experiments at 25.0% and 73.9% relative humidity did not have a thermocouple inside the column.

An interesting trend is observed in the temperature profiles, as seen in Figures 4.10 and 4.11. All temperature profiles for the pure H$_2$O breakthrough experiments initially increase rapidly, but then slow down until a peak is reached. Then the temperature drops similarly to other temperature profiles noticed in type 1 isotherms, such as CO$_2$ on zeolite 13X in Figure 4.11c. For all standard zeolite 13X experiments, the second temperature increase becomes more rapid as the peak is reached. These temperature profiles displayed a greater bed thermal conductivity, K_z, than expected [13]. Since the flow was high, $\approx$ 1.2-1.3 SLPM, and the concentration front was slow, conductivity heated the column up faster than the adsorptive heat front [64]. In this case the particle reynolds number, Re_p, was ≈ 4. For comparison, Re_p was ≈ 1 in the CO$_2$

breakthrough experiments. A larger than expected K_z has been noticed in other papers as well [58].

(a) CO_2 concentration breakthrough

(b) H_2O concentration breakthrough

(c) CO_2 thermal breakthrough

(d) H_2O thermal breakthrough
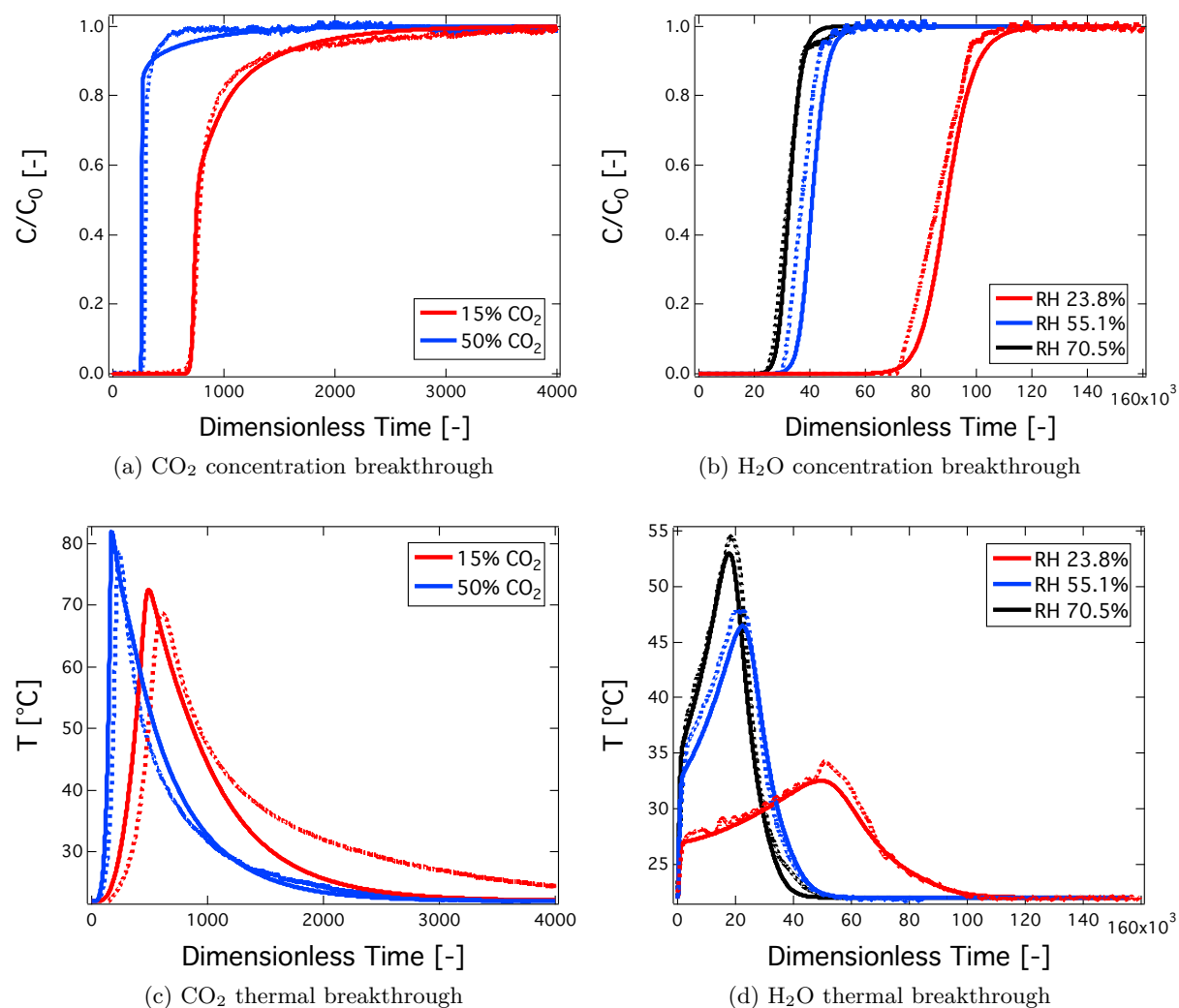
Figure 4.11: Single component CO_2 and H_2O concentration and temperature breakthrough profiles on premium zeolite 13X (Z10-02ND) at $\approx 22°C$. The CO_2 experiments are at 15 and 50 mol% CO_2. The H_2O experiments are at 25, 55 and 70% relative humidity. Experiments are the dotted lines and simulations are the solid lines. Temperature is measured at $z = 0.8L$.

4.3.2 Multicomponent Breakthrough Measurements

After the pure components were characterized, competitive CO_2/H_2O breakthroughs were measured. A summary is shown in Table 4.5. Dynamic column breakthrough experiments were performed by changing the carrier gas from instrument air to CO_2. The H_2O concentration was varied in the same way as the pure component experiments. Total flows were kept the same to ensure that the desired relative humidity was achieved. Again the flowrates were ≈ 1.2 to 1.3 SLPM. The simulation parameters were taken from the pure CO_2 experiments except for the

internal heat transfer coefficient, h_{in}, which was taken from the pure H_2O experiments. h_{in} was kept the same as the pure H_2O experiments because the flowrates were similar. The results are shown in Figures 4.12 to 4.14.

Table 4.5: A summary of the experimental competitive breakthrough experiments on premium (Z10-02ND) and standard (Z10-02) zeolite 13X. Instrument air was used as a sweep in all experiments.

Material	T [°C]	RH [%]	P_{H_2O} [bar]	P_{CO_2} [bar]	$q^*_{H_2O}$ [mol/kg]	$q^*_{CO_2}$ [mol/kg]
Z10-02	23.1	43.8	1.19×10^{-2}	1.0081	12.29	2.44
Z10-02ND	22.9	44.1	1.24×10^{-2}	1.0076	12.35	2.16
Z10-02ND	22.7	61.1	1.67×10^{-2}	1.0033	14.42	2.46

As seen in Figures 4.12 to 4.14, the H_2O breakthrough profiles are predicted very well. It seems that the fit is better for the premium zeolite 13X than the standard sample. However, the CO_2 breakthrough profiles are not predicted well. This discrepancy exists due to the assumptions of the dual-site Langmuir isotherm. Competition in the dual-site Langmuir isotherm is similar to ideal sorbed solution theory (IAST). The dual-site Langmuir isotherm has been shown to predict non-ideal systems when the feed concentrations of both gases are similar [65]. IAST is not able to accurately predict competitive loadings when the components have very different pure loadings at their respective equilibrium pressures. For these experiments at 1.02 bar, CO_2 was maintained between ≈ 0.99 to 1.01 bar with the balance being H_2O. At these partial pressures, H_2O is ≈ 3 to 4 times stronger than CO_2 on both zeolite 13X adsorbents. IAST usually predicts the heavier component's loading well; but, the loading of the lighter component suffers a significant over or under prediction compared to the real competitive loading. This is amplified when one component is very strong compared to the other, like in the case of a CO_2/H_2O system. For these conditions, IAST predicts that CO_2 will adsorb much more than is actually observed in the experiments. This is likely because CO_2 is very concentrated compared to H_2O.

For both materials, the b adsorption site in the dual-site Langmuir isotherm was made the high energy binding site. Both H_2O and CO_2 strongly adsorb onto standard and premium zeolite 13X. The kinetic diameter of CO_2 is ≈ 3.3Å while for H_2O it is ≈ 2.6Å. Since both materials adsorb strongly and are similarly sized, it is a good assumption that the binding sites will treat both species similarly [65]. This is imposed in the simulations by making both b sites the high energy site and both d sites the low energy sites. For single component systems this choice is arbitrary; but, for competitive systems the denominator for the b and d sites change depending on b and d parameters for each species [65].

The temperature profiles are matched decently. The initial magnitude of the temperature peak, which is due to the adsorption of CO_2, is not as great as experimentally observed. This has been observed previously on the standard zeolite 13X by Krishnamurthy et. al. [17]. The adsorbent's

heat loss is also predicted to be much faster in the simulation than is observed in the experiments for the first temperature peak. The second temperature peak, which is due to the adsorption of H_2O, also has a smaller magnitude than seen experimentally. In Figures 4.13 to 4.14, the temperature profiles seem to follow the trends of the second temperature peak better. This is probably linked to the good H_2O concentration breakthrough predictions from the competitive dual-site Langmuir isotherm. This is surprising since the temperature profile peaks were able to be predicted in the single component experiments.

The main observation from the CO_2/H_2O multicomponent experiments is that mixture is non-ideal. To accurately simulate a CO_2/H_2O system, a nonideal adsorption equilibrium model must be employed. Wang and LeVan had success matching competitive CO_2/H_2O loadings on zeolite 13X (Grace Davison) using the VEMC model [60]. However, this model will not be straight-forward since it is an implicit model [60]. Other real adsorbed solution theory models will be considered in future work.
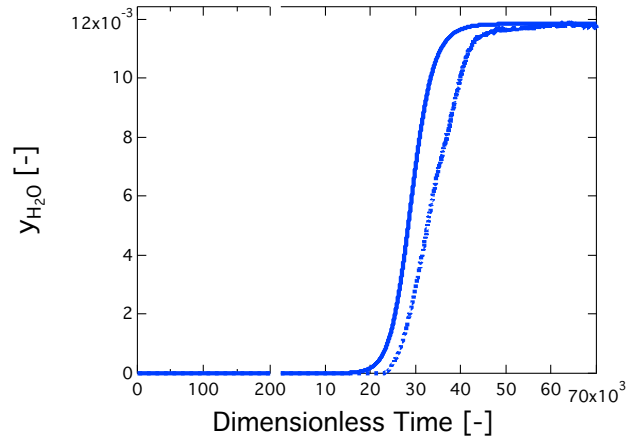
(a) H_2O concentration breakthrough
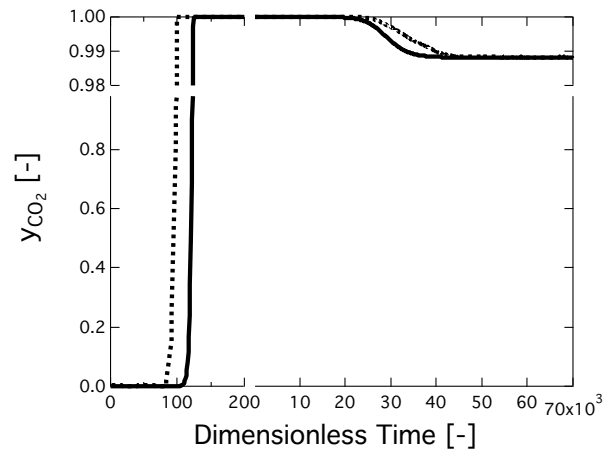
(b) CO_2 concentration breakthrough

Figure 4.12: Competitive CO_2/H_2O concentration breakthrough profiles on standard zeolite 13X (Z10-02) at 23.1°C and 43.8% relative humidity. Experiments are the dotted lines and simulations are the solid lines. This experiment did not have a thermocouple inside the column.
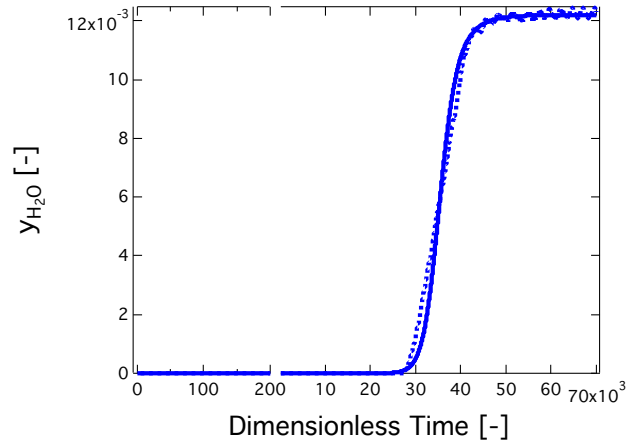
(a) H₂O concentration breakthrough
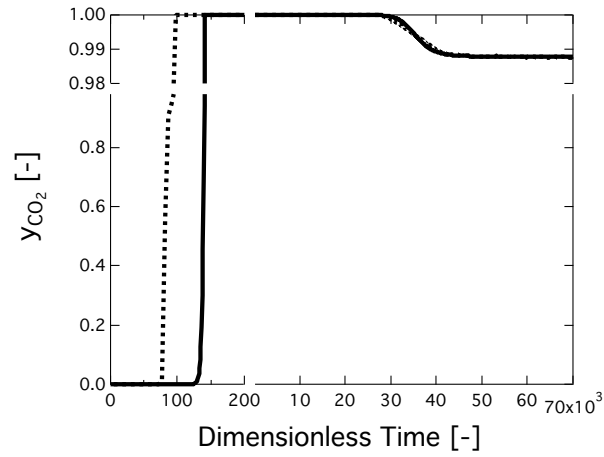
(b) CO₂ concentration breakthrough
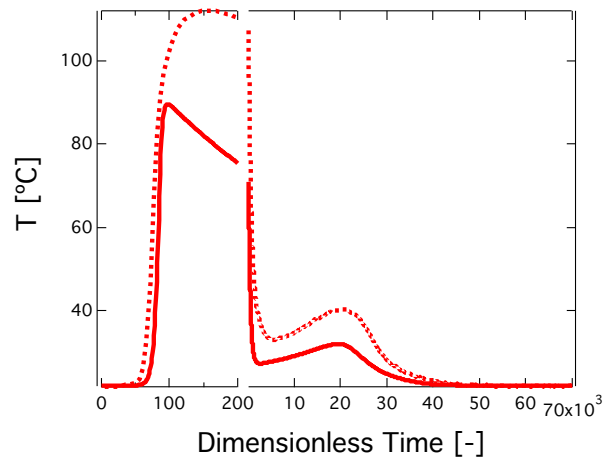
(c) CO₂/H₂O thermal breakthrough

Figure 4.13: Competitive CO_2/H_2O concentration and temperature breakthrough profiles on premium zeolite 13X (Z10-02ND) at 22.9°C and 44.1% relative humidity. Experiments are the dotted lines and simulations are the solid lines. Temperature is measured at $z = 0.8L$.
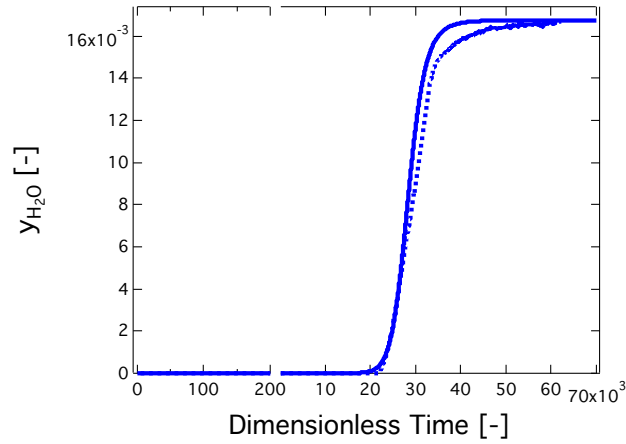
(a) H_2O concentration breakthrough
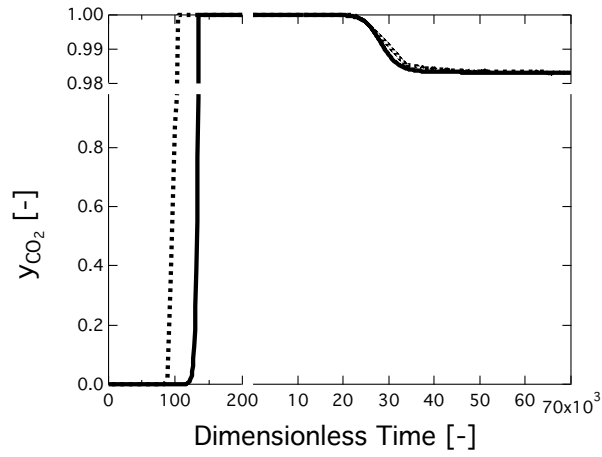
(b) CO_2 concentration breakthrough
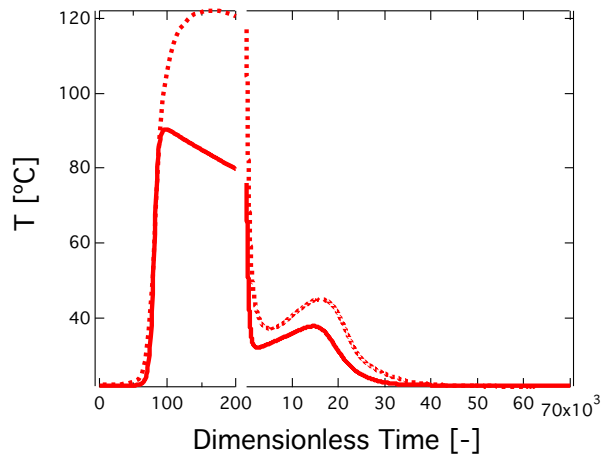
(c) CO_2/H_2O thermal breakthrough

Figure 4.14: Competitive CO_2/H_2O concentration and temperature breakthrough profiles on premium zeolite 13X (Z10-02ND) at 22.7°C and 61.1% relative humidity. Experiments are the dotted lines and simulations are the solid lines. Temperature is measured at $z = 0.8L$.

4.4   Conclusions

The benchmark adsorbent for post-combustion carbon capture is zeolite 13X. A typical post-combustion stream at 25°C could contain up to 3 mol% H_2O. However, in most studies water is neglected; instead a 15% CO_2, 85% N_2 flue is considered. H_2O adsorbs very strongly on zeolite 13X, therefore it is necessary to have some understanding of the competition between CO_2 and H_2O. Understanding this competition well will allow simulations to predict adsorptive behavior better. Two zeolite 13X samples were obtained (Zeochem, Uetikon am See, Switzerland) and characterized; one was a standard zeolite 13X (Z10-02) and the other was a premium zeolite 13X (Z10-02ND). Isotherms for CO_2 and N_2 were measured using volumetry and gravimetry at 0 (only N_2), 25, 50, 75, 100, 125 and 150°C. N_2 volumetric isotherms at -196°C were also performed to determine the surface area and internal volume of both adsorbents. H_2O equilibrium was measured using dynamic column breakthrough at 22°C. Measured equilibrium data for standard zeolite 13X was in agreement with the literature. H_2O equilibrium data for standard zeolite 13X from the literature was also used. Adsorption equilibrium data was fit to a dual-site Langmuir isotherm for all gases on all adsorbents. Carrier gases were humidified using a bubbler humidifier. Pure dynamic column breakthrough experiments for CO_2 and H_2O were performed at 1.02 bar and 22°C. Helium was used as a carrier for the CO_2 experiments and air for the H_2O experiments. Both were modeled and simulated using the adsorption simulator. The experiments and simulations displayed good agreement between both concentration and temperature breakthrough profiles. After pure components were simulated, competitive CO_2/H_2O breakthroughs were measured and simulated with the adsorption simulator. In the competitive CO_2/H_2O system, H_2O breakthrough profiles were matched well, but CO_2 profiles were not. This comes from the dual-site Langmuir isotherm, which assumes that competition is nearly ideal. From these experiments, it is obvious that IAST is not followed. To accurately predict CO_2 breakthrough profiles, a nonideal equilibrium model must be implemented. Nonideal equilibrium models, such as VEMC, will be explored in future work. After the competition between CO_2 and H_2O is described well, this model could be used to perform process studies and cycle optimization. The optimizations could maximize CO_2 purity, recovery and productivity while minimizing the required energy of the carbon capture process.

Chapter 5

Summary and Conclusions

5.1 Conclusions

This thesis characterized, modeled and simulated various adsorbent materials for adsorptive pre- and post-combustion carbon capture. Carbon capture and storage is a technology that aims to reduce CO_2 emissions while coal and fossil fuels are burned for power consumption in power plants. Reducing CO_2 emissions would help mitigate the harmful effects of climate change and directly reduce the ambient concentration of CO_2.

Chapter 2 details the theory and mathematics behind the experiments and process simulator used in this thesis. The chapter started with a discussion on different types of equilibrium data. At the low pressures used in this thesis, excess and absolute isotherms are essentially the same. Volumetry, gravimetry and dynamic column breakthrough equilibrium experiments were explained in detail. Volumetry is an equilibrium measurement that uses a known dosed volume of gas to determine an isotherm from a known mass of adsorbent. Volumetric isotherms are reported as excess isotherms. Gravimetry is an equilibrium measurement that weighs an adsorbent on a magnetic suspension balance as a gas is being adsorbed. Gravimetric measurements are reported as an absolute isotherm. Dynamic column breakthrough is an experiment that uses a adsorbent packed bed and a step function of inlet gas at a known concentration to determine column dynamics and equilibrium. Dynamic column breakthrough experiments are excess isotherm measurements. DCB measurements are then compared to the simulated dynamics. A series of isotherm models used in this thesis were explained with regard to thermodynamics and isotherm type. Ideal and real competitive isotherm models were explained. The adsorption simulator, a one-dimensional model with mass, momentum and heat balances, was presented. This simulator was built in MATLAB and solves a series of partial differential equations using necessary experimental parameters.

In Chapter 3 a new activated carbon adsorbent, TDA 2015, developed by TDA Research Inc. (Wheat Ridge, CO, USA) for pre-combustion carbon capture was characterized and compared against our in-house adsorption simulator. Volumetric isotherms were collected at 30, 60, 120

and 160°C on a Micromeritics ASAP 2020 (Norcross, GA, USA). A series of dynamic column breakthrough and desorption experiments measured CO_2 loading and dynamics at $\approx$ 2.5, 4.5, 6.5, 8.5 and 10.5 bar of CO_2 at $\approx$ 160, 200 and 240°C. All dynamic column breakthrough experiments remained fairly isothermal during adsorption. The largest temperature gain was $\approx$ 15°C. Concentration breakthrough profiles $\geq$ 8.5 bar of CO_2 show a significant amount of dispersion. All breakthrough experiments were simulated using the adsorption simulator. The error between experiments and simulation was at most 10%. At low concentrations, $\leq$ 4.5 bar CO_2, the simulator fit the qualitative breakthrough shape well. However, at $\geq$ 8.5 bar CO_2, the simulator was unable to model the qualitative breakthrough shape. A series of parametric studies on mass transfer and heat transfer parameters were done to determine possible explanations for the shape of the experimental curves. A series of isotherm models, with different isotherm shapes, were employed to determine possible equilibrium effects. These parametric studies and isotherm case studies show the simulator is able to model the dispersed breakthrough behavior seen at $\geq$ 8.5 bar CO_2, but none are consistent with the temperature breakthrough profiles or isotherm data. However, it does seem extremely likely that either the temperature profiles affect or are affected by the concentration breakthroughs.

CO_2 and H_2O competition in humid post-combustion carbon capture was studied in Chapter 4. Two zeolite 13X samples were obtained from Zeochem (Uetikon am See, Switzerland) and characterized; one was a standard zeolite 13X (Z10-02) and the other was a premium zeolite 13X (Z10-02ND). Isotherms for CO_2 and N_2 were measured using volumetry and gravimetry at 0 (only N_2), 25, 50, 75, 100, 125 and 150°C. H_2O equilibrium was measured using dynamic column breakthrough at 22°C. H_2O equilibrium data from the literature for standard zeolite 13X was also used. Adsorption equilibrium data was fit to a dual-site Langmuir isotherm for all gases on all adsorbents. Carrier gases were humidified using a bubbler humidifier. Pure dynamic column breakthrough experiments for CO_2 and H_2O were performed. Helium was used as a carrier for CO_2 experiments and air for H_2O. Both were modeled and simulated using the adsorption simulator. The experiments and simulations displayed good agreement between both concentration and temperature breakthrough profiles. After pure components were simulated, competitive CO_2/H_2O breakthroughs were measured and simulated with the adsorption simulator. In the competitive breakthroughs, only H_2O was predicted well. Competition in the dual-site Langmuir isotherm is nearly ideal. From the CO_2 breakthrough profiles, it is clear that the competition between CO_2 and H_2O is not ideal.

5.2 Future Work

Future work on TDA 2015 should confirm the cause of the dispersion in the concentration breakthrough profiles at $\geq$ 8.5 bar of CO_2. This could be done by testing TDA 2015 in another breakthrough apparatus. High pressure CO_2 equilibrium data on a gravimetric system would be useful to confirm dynamic column breakthrough equilibrium measurements performed up

to 10.5 bar of CO_2. High pressure CO_2 measurements could also confirm whether equilibrium effects are present. Low temperature dynamic column breakthrough experiments should induce the dispersion and might also be useful for future work.

For humid carbon capture on zeolite 13X, future work should focus on an implementation of a nonideal competitive isotherm model for CO_2 and H_2O, such as the VEMC model. This should predict CO_2 concentration breakthroughs better than the dual-site Langmuir isotherm can. Pure H_2O and competitive CO_2/H_2O isotherms should be measured. Afterwards, cycle studies and process optimization should be performed using these models to determine the best process conditions to maximize purity and recovery of CO_2.

Bibliography

[1] Christopher B Field, Vicente R Barros, K Mach, and M Mastrandrea. *Climate Change 2014: Impacts, Adaptation, and Vulnerability*, volume 1. Cambridge University Press Cambridge and New York, 2014.

[2] IEA. Energy, Climate Change and Environment - 2014 Insights. Technical report, International Energy Agency, 2014.

[3] R M Hoesly, S J Smith, L Feng, Z Klimont, G Janssens-Maenhout, Tyler Pitkanen, J J Seibert, L Vu, R J Andres, R M Bolt, et al. Historical (1750-2014) anthropogenic emissions of reactive gases and aerosols from the community emission data system (ceds). *Geosci. Model Dev. Discuss.*, pages 1–41, 2017.

[4] P Timothy, Wahlen Martin, B Robert, C Stephen, D Charles, Heimann Martin, A Harro, et al. Atmospheric CO_2 and CO_2 exchange with the terrestrial biosphere and oceans from 1978 to 2000: Observations and carbon cycle implications. *Scripps Institution of Oceanography UC San Diego*, 2005.

[5] Pieter Tans. Monthly CO_2 measurements from 1959 to may 2017. NOAA, May 2017.

[6] EPA. Inventory of U.S. Greenhouse Gas Emissions and Sinks – 1990-2015. Technical report, EPA, 2017.

[7] Dennis Y C Leung, Giorgio Caramanna, and M Mercedes Maroto-Valer. An overview of current status of carbon dioxide capture and storage technologies. *Renewable Sustainable Energy Rev.*, 39:426–443, 2014.

[8] Mike Haines, Jasmin Kemper, John Davison, John Gale, Prachi Singh, and Stanley Santos. Assessment of emerging CO_2 capture technologies and their potential to reduce costs. TR 4, IEAGHG, 2014.

[9] Reza Haghpanah, Aniruddha Majumder, Ricky Nilam, Arvind Rajendran, Shamsuzzaman Farooq, Iftekhar A Karimi, and Mohammad Amanullah. Multiobjective optimization of a four-step adsorption process for postcombustion CO_2 capture via finite volume simulation. *Industrial & Engineering Chemistry Research*, 52(11):4249–4265, 2013.

[10] Abass A Olajire. CO_2 capture and separation technologies for end-of-pipe applications–a review. *Energy*, 35(6):2610–2628, 2010.

[11] G Suresh Kumar, M Viswandham, A. V S S K S Gupta, and G Santosh Kumar. A review of pre-combustion CO_2 capture in IGCC. *Int J Res Eng Technology*, 2:847–853, 2013.

[12] Brad Page. The global status of CCS 2016. Technical report, Global CCS Institute, 2016.

[13] Douglas M Ruthven. *Principles of Adsorption and Adsorption Processes*. John Wiley & Sons, 1984.

[14] Federico Brandani and Douglas M Ruthven. The effect of water on the adsorption of CO_2 and C_3H_8 on type X zeolites. *Industrial & Engineering Chemistry Research*, 43(26):8339–8344, 2004.

[15] Penny Xiao, Jun Zhang, Paul Webley, Gang Li, Ranjeet Singh, and Richard Todd. Capture of CO_2 from flue gas streams with zeolite 13X by vacuum-pressure swing adsorption. *Adsorption*, 14(4-5):575–582, 2008.

[16] Yu Wang and M Douglas LeVan. Adsorption equilibrium of carbon dioxide and water vapor on zeolites 5A and 13X and silica gel: pure components. *Journal of Chemical & Engineering Data*, 54(10):2839–2844, 2009.

[17] Shreenath Krishnamurthy, Vemula Rama Rao, Sathishkumar Guntuka, Paul Sharratt, Reza Haghpanah, Arvind Rajendran, Mohammad Amanullah, Iftekhar A. Karimi, and Shamsuzzaman Farooq. CO_2 capture from dry flue gas by vacuum swing adsorption: A pilot plant study. *AIChE J.*, 60(5):1830–1842, 2014.

[18] Shreenath Krishnamurthy, Reza Haghpanah, Arvind Rajendran, and Shamsuzzaman Farooq. Simulation and optimization of a dual-adsorbent, two-bed vacuum swing adsorption process for CO_2 capture from wet flue gas. *Industrial & Engineering Chemistry Research*, 53(37):14462–14473, 2014.

[19] Ashwin Kumar Rajagopalan, Adolfo M Avila, and Arvind Rajendran. Do adsorbent screening metrics predict process performance? a process optimisation based study for post-combustion capture of CO_2. *Int. J. Greenhouse Gas Control*, 46:76–85, 2016.

[20] Alan L Myers and Peter A Monson. Physical adsorption of gases: the case for absolute adsorption as the basis for thermodynamic analysis. *Adsorption*, 20(4):591–622, 2014.

[21] A L Myers and P A Monson. Adsorption in porous materials at high pressure: theory and experiment. *Langmuir*, 18(26):10261–10273, 2002.

[22] Stefano Brandani, Enzo Mangano, and Lev Sarkisov. Net, excess and absolute adsorption and adsorption of helium. *Adsorption*, 22(2):261–276, 2016.

[23] A. Rajendran. *Adsorption and chromatography under supercritical conditions*. PhD thesis, ETH Zürich, 2004.

[24] Sasidhar Gumma and Orhan Talu. Net adsorption: a thermodynamic framework for supercritical gas adsorption and storage in porous solids. *Langmuir*, 26(22):17013–17023, 2010.

[25] Rubotherm GmbH. *Procedure of Performing Gravimetric Adsorption Measurements*, 2016.

[26] A Malek, S Farooq, MN Rathor, and K Hidajat. Effect of velocity variation due to adsorption-desorption on equilibrium data from breakthrough experiments. *Chem. Eng. Sci.*, 50(4):737–740, 1995.

[27] S Guntuka, S Farooq, and Arvind Rajendran. A-and b-site substituted lanthanum cobaltite perovskite as high temperature oxygen sorbent. 2. column dynamics study. *Industrial & Engineering Chemistry Research*, 47(1):163–170, 2008.

[28] Shamsuzzaman Farooq. Design and analysis of dynamic column breakthrough experiments. In *Fundamentals of Adsorption 12*, 2016.

[29] Stephen Brunauer, Lola S Deming, W Edwards Deming, and Edward Teller. On a theory of the van der waals adsorption of gases. *J. Am. Chem. Soc.*, 62(7):1723–1732, 1940.

[30] Irving Langmuir. The adsorption of gases on plane surfaces of glass, mica and platinum. *J. Am. Chem. Soc.*, 40(9):1361–1403, 1918.

[31] Shivaji Sircar. Comments on practical use of Langmuir gas adsorption isotherm model. *Adsorption*, 23(1):121–130, 2017.

[32] Reza Haghpanah, Ricky Nilam, Arvind Rajendran, Shamsuzzaman Farooq, and Iftekhar A Karimi. Cycle synthesis and optimization of a vsa process for postcombustion CO_2 capture. *AIChE J.*, 59(12):4735–4748, 2013.

[33] Seymour Lowell, Joan E Shields, Martin A Thomas, and Matthias Thommes. *Characterization of Porous Solids and Powders: Surface Area, Pore Size and Density*, volume 16. Springer Science & Business Media, 2012.

[34] József Tóth. Uniform interpretation of gas/solid adsorption. *Adv. Colloid Interface Sci.*, 55:1–239, 1995.

[35] Ralph T. Yang. *Gas Separation by Adsorption Processes*. Imperial College Press, 1997.

[36] Stephen Brunauer, Paul Hugh Emmett, and Edward Teller. Adsorption of gases in multimolecular layers. *J. Am. Chem. Soc.*, 60(2):309–319, 1938.

[37] Georges Guiochon, Attila Felinger, and Dean G G Shirazi. *Fundamentals of Preparative and Nonlinear Chromatography*. Academic Press, 2006.

[38] Johan Duane Baboolal. Evaluation of novel metal-organic framework materials for adsorptive post-combustion CO_2 capture. Master's thesis, University of Alberta, 2015.

[39] Alan L Myers and John M Prausnitz. Thermodynamics of mixed-gas adsorption. *AIChE J.*, 11(1):121–127, 1965.

[40] Nan Qi and M Douglas LeVan. Virial excess mixing coefficient corrections for the adsorbed solution theory. *Industrial & engineering chemistry research*, 44(10):3726–3732, 2005.

[41] S Sircar and DV Cao. Heat of adsorption. *Chemical engineering & technology*, 25(10):945–948, 2002.

[42] Reza Haghpanah, Arvind Rajendran, Shamsuzzaman Farooq, Iftekhar A Karimi, and Mohammad Amanullah. Discrete equilibrium data from dynamic column breakthrough experiments. *Industrial & Engineering Chemistry Research*, 51(45):14834–14844, 2012.

[43] Phillip C. Wankat. *Separation Process Engineering*. Prentice Hall, 2007.

[44] E Gleuckauf and J I Coates. The influence of incomplete equilibrium on the front boundary of chromatograms and the effectiveness of separation. *J. Chem. Soc.*, 1315, 1947.

[45] Shailesh Vora, Lynn Brickett, Pradeep Indrikanti, Ron Munson, James Murphy, Trixie Rife, Justin Strock, and Connie Zaremsky. DOE/NETL advanced carbon dioxide capture R&D program: Technology update. Technical report, DOE & NETL, 2013.

[46] Robert M. Davidson. Pre-combustion capture of CO_2 in IGCC plants. Technical report, IEA Clean Coal Centre, 2011.

[47] Trevor C Drage, O Kozynchenko, C Pevida, Marta G Plaza, F Rubiera, JJ Pis, Colin E Snape, and S Tennison. Developing activated carbon adsorbents for pre-combustion CO_2 capture. *Energy Procedia*, 1(1):599–605, 2009.

[48] Claudia F Martín, Marta G Plaza, JJ Pis, F Rubiera, C Pevida, and TA Centeno. On the limits of CO_2 capture capacity of carbons. *Sep. Purif. Technol.*, 74(2):225–229, 2010.

[49] Sayed Alireza Hosseinzadeh Hejazi, Arvind Rajendran, James A Sawada, and Steven M Kuznicki. Dynamic column breakthrough and process studies of high-purity oxygen production using silver-exchanged titanosilicates. *Industrial & Engineering Chemistry Research*, 55(20):5993–6005, 2016.

[50] A. K. Rajagopalan. Material selection and process design for adsorptive CO_2 capture. Master's thesis, University of Alberta, 2015.

[51] S Farooq, Huang Qinglin, and I A Karimi. Identification of transport mechanism in adsorbent micropores from column dynamics. *Industrial & Engineering Chemistry Research*, 41(5):1098–1106, 2002.

[52] Huang Qinglin, S M Sundaram, and S Farooq. Revisiting transport of gases in the micropores of carbon molecular sieves. *Langmuir*, 19(2):393–405, 2003.

[53] Shivaji Sircar, Ravi Kumar, and Kenneth J Anselmo. Effects of column nonisothermality or nonadiabaticity on the adsorption breakthrough curves. *Industrial & Engineering Chemistry Process Design and Development*, 22(1):10–15, 1983.

[54] Steven Dean Dietz, Gokhan Alptekin, and Ambalavanan Jayaraman. High capacity carbon dioxide sorbent, September 1 2015. US Patent 9,120,079.

[55] I Pentchev, K Paev, and I Seikova. Determination of the concentration curves for non-isothermal adsorption using an approach based on the incorporation of experimental temperature profiles in one-dimensional model. *Comptes Rendus de l'Academie Bulgare des Sciences*, 53(10):10–41, 2000.

[56] Illam Park and Kent S Knaebel. Adsorption breakthrough behavior: unusual effects and possible causes. *AIChE J.*, 38(5):660–670, 1992.

[57] Marco Mazzotti and Arvind Rajendran. Equilibrium theory-based analysis of nonlinear waves in separation processes. *Annual Review of Chemical and Biomolecular Engineering*, 4:119–141, 2013.

[58] Max Hefti, Lisa Joss, Dorian Marx, and Marco Mazzotti. An experimental and modeling study of the adsorption equilibrium and dynamics of water vapor on activated carbon. *Industrial & Engineering Chemistry Research*, 54(48):12165–12176, 2015.

[59] Gang Li, Penny Xiao, Paul Webley, Jun Zhang, Ranjeet Singh, and Marc Marshall. Capture of CO_2 from high humidity flue gas by vacuum swing adsorption with zeolite 13X. *Adsorption*, 14(2-3):415–422, 2008.

[60] Yu Wang and M Douglas LeVan. Adsorption equilibrium of binary mixtures of carbon dioxide and water vapor on zeolites 5A and 13X. *Journal of Chemical & Engineering Data*, 55(9):3189–3195, 2010.

[61] Qassim Hassan Dirar and Kevin F Loughlin. Intrinsic adsorption properties of CO_2 on 5A and 13X zeolite. *Adsorption*, 19(6):1149–1163, 2013.

[62] Arno De Klerk. Voidage variation in packed beds at small column to particle diameter ratio. *AIChE J.*, 49(8):2022–2029, 2003.

[63] Ana M Ribeiro, Ticiane P Sauer, Carlos A Grande, Regina FPM Moreira, José M Loureiro, and Alírio E Rodrigues. Adsorption equilibrium and kinetics of water vapor on different adsorbents. *Industrial & Engineering Chemistry Research*, 47(18):7019–7026, 2008.

[64] Gilbert F Froment and Kenneth B Bischoff. *Chemical Reactor Analysis and Design*. John Wiley & Sons Inc, 1990.

[65] James A Ritter, Shubhra J Bhadra, and Armin D Ebner. On the use of the dual-process Langmuir model for correlating unary equilibria and predicting mixed-gas adsorption equilibria. *Langmuir*, 27(8):4700–4712, 2011.